Scanning Tunneling Microscopy/Spectroscopy Studies of Ultrathin Sb Films

XU WENTAO
(B.Eng., Shandong Univ.)

A THESIS SUBMITTED

FOR THE DEGREE OF DOCTOR OF PHILOSOPHY

DEPARTMENT OF PHYSICS

NATIONAL UNIVERSITY OF SINGAPORE

2013

DECLARATION

I hereby declare that the thesis is my original work and it has been written by me in its entirety. I have duly acknowledged all the sources of information which have been used in the thesis.

This thesis has also not been submitted for any degree in any university previously.

_____

Xu Wentao

_____

ACKNOWLEDGEMENT

First and foremost, I would like to express my sincerest gratitude to my supervisor, Associate Prof. Wang Xue-sen, for his invaluable guidance, inspiration and constant support throughout the course of my work. I have benefited tremendously from Prof. Wang's insight into the physics frontier, broad knowledge in nanoscience and great patience in guiding my project and thesis writing.

I would also like to express my sincerest gratitude to Dr. Pan Feng, Dr. Yao Guanggeng and Mr. Luo Ziyu for their generous support and invaluable suggestions. Dr Pan Feng and Dr. Yao Guanggeng also taught me how to operate UHV-STM systems; Mr. Luo Ziyu greatly assisted me in performing calculations.

I would also like to thank Prof. Chen Wei for his constructive suggestions and encouragement.

I also thank all my friends and group members in NUS. To Chu Xinjun, Wang Xiao, Sun Jiatao, Lu Yunhao, Bai Zhaoqiang, Huang Han, Xu Hai, Wu Qingyun, Zhou Miao and Qi Dongchen for their kind help and discussions. To Chen Xiao, Wang Yinghui, Wang Yuzhan, Wang Qian, Niu Tianchao, Mao Hongying, Xie Lanfei, Diao Yingying, Cao Liang, Ma Fusheng, Lu Junpeng, Liu Hongwei, Pan Huihui, Li Yanan, Mr Ho and Mr. Wong for their kind help.

Finally yet importantly, I thank my parents, brother Xu Wenhua and sister Xu Wenjuan for their support, tolerance and love.

TABLE OF CONTENTS

SUMMARY

Antimony (Sb) is a semimetal with unique topological surface states (TSS). Bulk Sb is not topological insulator (TI) because of its indirect negative bulk gap. Taking advantage of quantum size effect, Sb thin film can open a bulk gap. This thesis presents the studies of ultrathin Sb films by scanning tunneling microscopy (STM) and spectroscopy (STS) together with first-principles calculations.

Self-assembled Sb nanostructures tend to form high islands because Sb source evaporates in the form of Sb_4 molecules. By adding a cracking part to crack Sb_4 into single atoms, ultrathin Sb films can be grown on Si(111), Si(111)-$\sqrt{3}\times\sqrt{3}$:Bi and HOPG. Thin film growth on solid substrate is affected by kinetics. As a result, the morphology of Sb nanostructures varies a lot as the Si(111) substrate temperature changes. Sb(111) films of best quality on Si(111) can be obtained by depositing Sb at low temperature followed with post-growth annealing. The thinnest Sb(111) film obtained here is 4 BL.

Surface states on 30 BL Sb(111) is spin-polarized TSS without inter-surface coupling. However, for 9 BL Sb(111), inter-surface coupling is significant near $\bar{M}$, while near $\bar{\Gamma}$ surface states are still spin-polarized. This is because the penetration depth is longer near $\bar{M}$; away from $\bar{M}$, penetration depth is short. Inter-surface coupling is thickness- and *k*-dependent. For 4 BL Sb(111), the space inversion asymmetry (SIA) along the surface normal direction induced by the substrate must be taken into account for the interpretation of the surface states. By replacing one Sb atom with one Bi atom from the bottom layer of the 4 BL freestanding Sb(111) unit cell, the SIA effect is

simulated in the first-principle calculations. The effects of the SIA on surface states near $\bar{\Gamma}$ is discussed in detail.

Sb on HOPG form Sb (110) films, which follow even-ML growth mode below 6 ML; above 6 ML, both even- and odd-ML Sb(110) can be observed. First-principles calculations showed that the ultrathin Sb(110) films are relaxed. The energetics of the relaxed Sb(110) films supports the even-ML growth mode below 6 ML. The calculated density of states (DOS) based on the relaxed Sb(110) films is in reasonable agreement with the measured STS. Both experiments and calculations show that the surface states in ultrathin Sb(110) is weak. A 4× reconstruction forms at the edge along $\left[0\,\bar{1}1\right]$ direction in certain conditions.

LIST OF ABBREVIATIONS

2DEG	2D electron gas
ARPES	angle-resolved photoemission spectroscopy
BL	bilayer
BZ	Brillouin zone
CEC	constant energy contour
DAS	dimer adatom stacking-fault
DFT	density functional theory
DOS	density of states
FT	Fourier transform
HOPG	highly ordered pyrolytic graphite
LDOS	local density of states
LEED	low-energy electron diffraction
LT	low temperature
ML	monolayer
QHE	quantum Hall effect
QPI	quasiparticle interference
SBZ	surface Brillouin zone
SIA	space inversion asymmetry
SOC	spin-orbit coupling
STM/STS	scanning tunneling microscopy/spectroscopy
TI	topological insulator
TRIM	time reversal invariant momentum
TRS	time reversal symmetry
TSS	topological surface state
UHV	ultra-high vacuum

LIST OF FIGURES

Chapter 1

Introduction

Nanoscience and nanotechnology study nanostructures whose sizes range from 1-100 nm (1 nm = 10^{-9} m) in one or more dimensions, including clusters, nanoparticles, quantum dots, nano-crystallines, nanotubes, nanorods and ultrathin films, or aggregations of individual nanostructures. The study of nanomaterials is important in two ways. First, nanomaterials are the transition between single atoms and bulk materials. A thorough understanding of nanomaterials can deepen our understanding of bulk materials. Second, nanomaterials have many special properties due to their nanoscale dimensions, for example, catalytic properties related with size and shape of nanoparticles,[1, 2] unique magnetic properties,[3-5] enhanced non-linear optical properties,[6-8] the unique properties of carbon fullerene,[9, 10] nanotube[11] and graphene.[12]

The research and development of nanomaterials include three important aspects: preparation, properties characterization and device application. Nanomaterials can be prepared by top-down and bottom-up approaches. Top-down approach uses externally controlled tools to cut, mill and etch larger materials to produce nanostructures. Lithographic methods including optical lithography, electron beam lithography and ion beam lithography belong to this category. Bottom-up approach constructs nanomaterials from atoms or molecules that can react and grow, or self-assemble into structures that are more complex. Deposition techniques like physical vapor deposition (PVD) and chemical vapor deposition (CVD), molecular self-assembly or manipulation with scanning tunneling microscopy/atomic force microscopy[13, 14] belong to this category.

In this thesis, self-assembled antimony ultrathin films and islands are prepared on certain substrates by PVD in ultra-high vacuum (UHV) chamber. The bottom boundary of a film or island is in contact with the solid substrate, forming *interface*, while the top boundary of a film or island is in contact with vacuum, forming *surface*.

The properties of thin films or islands include physical topography, chemical composition, atomic and electronic structures. To characterize these properties, many techniques can be applied taking advantage of interactions between photon and the material, such as in infrared spectroscopy (IR), X-ray photoelectron spectroscopy (XPS), or between electron and the material, such as in Auger electron spectroscopy (AES), low-energy electron diffraction (LEED), scanning electron microscopy (SEM), transmission electron microscopy (TEM) and scanning tunneling microscopy (STM). Most of these characterizations are carried out in vacuum, because in atmosphere, surfaces may be contaminated and electrons are scattered by gas molecules.

The characterization work in this thesis are based mainly on UHV STM system, which can probe physical morphology, localized density of states (DOS), surface atomic structure. Nanoscience can not only explain observed properties, but also predict properties accurately by quantum mechanics. The ground state of many-body systems can be determined by first-principles approaches, such as Hartree-Fork approximation,[15] density functional theory[16] (DFT) and quantum Monte Carlo methods.[17] In this thesis, the first-principles total energy pseudopotential method based on DFT are employed to study the properties of nanomaterials.

The following sections provide an overview of thin film growth theory, a general introduction to topological insulators (TI), and the motivation and synopsis of this thesis.

1.1 Thin film growth on solid substrate

Thin film growth on solid substrate is usually achieved by a deposition method. The desired source materials are heated up and vaporized. The vapor condenses onto the substrate surface after reaching certain pressure. The condensed solid structure may form oriented single crystalline film on a single crystal substrate, and this process is referred to as *epitaxy*. Epitaxy can be divided into homoepitaxy (the substrate and thin film are the same material) and heteroepitaxy (the substrate and thin film are different materials). Generally, the thin film growth process on substrate is controlled by the interplay between thermodynamics and kinetics. Thermodynamics approach can be understood in terms of surface and interface energies, as the thin film tend to minimize the total energy. However, film growth process is also concerned with kinetics, where growth conditions and the surface conditions affect film morphology. In this section, the effects of these two interplaying factors on thin film growth are briefly introduced.

1.1.1 Thermodynamics in thin film growth

Three general growth modes exist in the thin film growth,[18] as shown in Fig. 1.1. They are:

(i) Layer-by-layer, or Frank-van der Merwe (FM) growth mode. In this growth mode, one layer fully covers the sample before growth of the next layer, forming 2D thin film.

(ii) Island, or Volmer-Weber (VW) growth mode. In this mode, 3D islands nucleate and grow.

(iii) Layer-plus-island, or Stranski-Krastanov (SK) growth mode. The thin film follows the layer-by-layer growth mode first for several strained layers, then islands form on the 2D thin film.

The first two growth modes can be understood in terms of surface and interface energies. Let γ_s, γ_f and γ_{sf} be the substrate surface energy, thin film surface energy and interface energy per unit area, respectively. If the interface bonding is strong, *i.e.*, γ_{sf} is very low, we may have $\gamma_f + \gamma_{sf} < \gamma_s$, the interface should be as large as possible to reduce the total energy, therefore, thin film follows the layer-by-layer growth mode. If the interface bonding is weak, *i.e.*, γ_{sf} is very high, we may have $\gamma_f + \gamma_{sf} > \gamma_s$, interface area should be reduced to reduce total energy, hence, 3D islands form.

The layer-plus-island growth mode is related with lattice mismatch between the substrate and thin film. The thin film adjust itself to match the substrate lattice constant due to strong interface binding to have lower γ_{sf}, but at the expense of elastic deformation energy E_{el}. Initially, E_{el} is low because the strained film is thin. We have $\gamma_f + \gamma_{sf} + E_{el} < \gamma_s$, hence, the film follow layer-by-layer growth mode first. As the strained film becomes thicker, E_{el} is higher. To reduce E_{el}, 3D islands form on the strained thin film.

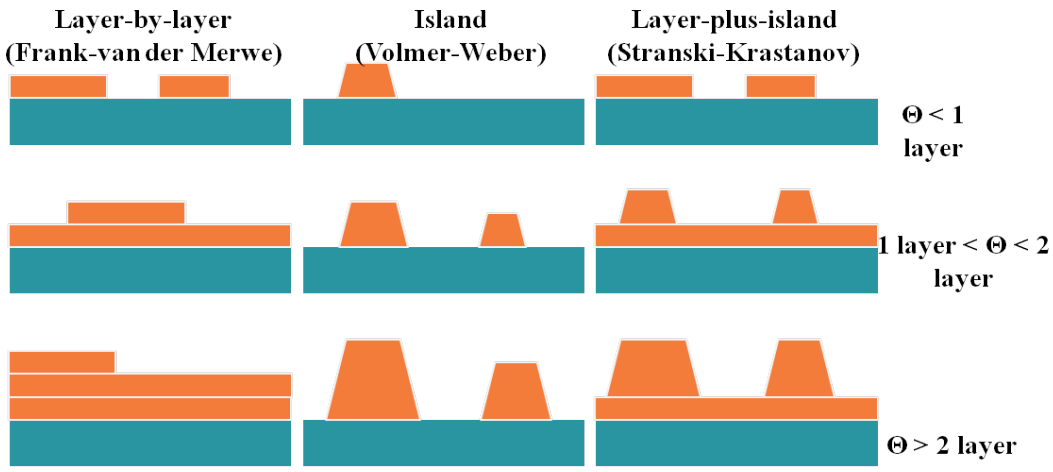

Fig. 1.1. Schematic view of the three main thermodynamic growth modes. (a) Layer-by-layer, or Frank-van der Merwe (FM) growth mode. (b) Island, or Volmer-Weber (VW) growth mode. (c) Layer-plus-island, or Stranski-krastanov (SK) growth mode. Θ is the coverage of the thin film.

1.1.2 Kinetics in thin film growth

Instead of forming the thermodynamic-equilibrium shape, thin film morphology is often influenced by many other factors, such as depositing flux, substrate chemical activity and substrate temperature. The typical processes involved in thin film growth on a microscopic scale are shown in Fig. 1.2(a). The source atoms attach to the substrate after arriving at the substrate from gaseous phase, and become adatoms. Adatoms may stay where they land on the surface if adatom-substrate interaction is strong or kinetic energy of adatoms is small. Or else, adatoms diffuse over the surface until existing clusters or defects, such as steps, capture them. Adatoms may also stop diffusing after combining with other adatoms to form clusters. Small clusters are metastable and may decompose into single adatoms. They are more stable as they grow in size.

Adatoms may diffuse on a flat terrace (intralayer diffusion) or across a terrace (interlayer diffusion). To characterize the diffusion process, we should consider the potential energy for adatoms on a surface, as shown in Fig. 1.2(b). On a flat terrace, adatoms on different sites could have different interaction strength with substrate and thus different energy, feeling the diffusion barrier E_{diff}. If adatoms migrate to the lower side of a step from a flat terrace, they are very likely to stick to the edge because of higher coordination number (number of nearest-neighbor atoms) at the lower side of the step than on the flat terrace. Therefore, the diffusion across a step edge from the lower side is usually neglected. If adatoms migrate to the step edge from the upper side, an additional barrier ΔE_{ES} (Ehrlich-Schwoebel barrier[19, 20]) appears because adatoms have low coordination number when crossing the edge.

Depending on the relative rate of deposition, intralayer diffusion, which is related with E_{diff}, and interlayer diffusion, which is related with ΔE_{ES}, three general growth modes are introduced as follows (Fig. 1.2(c)).

(i) Step-flow growth mode. Intralayer diffusion is quite high, thus adatoms can diffuse to the lower side of the step edge and stick to it. The film extends from the step edge. In this situation, interlayer diffusion does not play an important role.

(ii) Layer-by-layer growth mode. If the diffusion length is shorter than the terrace width, the film grows from nucleation of clusters (islands) on the flat terrace. Interlayer diffusion is high so that adatoms deposited on top of the islands can cross to the lower side of the step.

(iii) Multilayer growth mode. The same as layer-by-layer growth mode, except that the interlayer diffusion is low so that adatoms on an island nucleate into island of a new layer.

For the case of homoepitaxy, E_{diff} and ΔE_{ES} do not change during the film growth process; for the case of heteroepitaxy, adatoms landing on the film and substrate feel different E_{diff} and ΔE_{ES}. Higher substrate temperature raises the kinetic energy of adatoms, thereby enhancing both intralayer and interlayer diffusion. Film morphology varies a lot depending on the source material and substrate conditions, such as surface structure, chemical activity, temperature and terrace width. This is the reason why we can control the film morphology to certain extent by changing these conditions.

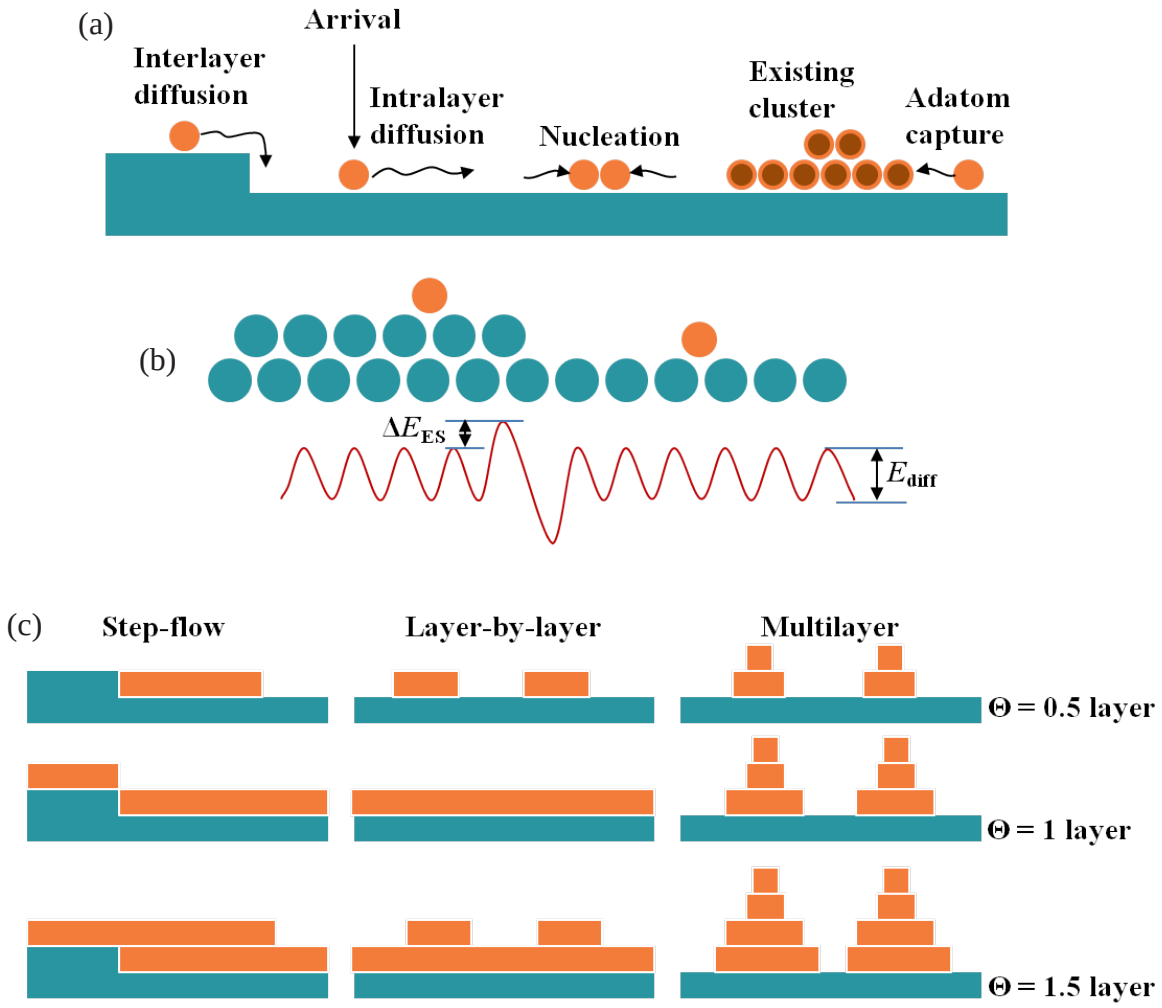

Fig. 1.2. (a) Schematic diagram showing typical processes involved in the film growth on solid substrate. (b) Schematic diagram of terrace diffusion barrier E_{diff} and Ehrlich-Schwoebel barrier ΔE_{ES}. (c) Schematic view of the three kinetic growth modes.

1.2 Topological insulators

1.2.1 From quantum Hall effect to quantum spin Hall effect

Landau's symmetry-breaking theory[21] is one of the foundations of traditional condensed matter physics.[22] The main point of this theory is that the absence of certain symmetry in a certain state of matter corresponds to a phase transition. For example, ferromagnetism and antiferromagnetism correspond to broken time reversal symmetry (TRS). Superfluidity and superconductor correspond to broken gauge symmetry. Phase transitions to ferromagnetism and antiferromagnetism or superfluidity and superconductor are second order transitions. Though Landau's symmetry-breaking theory is precisely for second order transition, its basic concept can be extended to some first order transitions as well. For example, liquid to crystalline solid transition corresponds to broken translational symmetry and rotational symmetry.

Integer quantum Hall (QH) state[23] discovered in 1980 does not have an analogous symmetry that is spontaneously broken and cannot be described by Landau's symmetry-breaking theory. The QH state occurs when a strong external magnetic field is applied to a 2D electron gas (2DEG) at low temperature, such as GaAs quantum well. Electrons in the bulk will follow circular cyclotron orbits, with energy levels quantized to be $(n+\frac{1}{2})\hbar\omega_c$ and $\omega_c = eB/m$ is the cyclotron frequency. The energy levels are called Landau levels. The orbits are localized in the bulk, which means that the electrons cannot move from one side to the other in an electric field. However, if we look at the boundary, electrons at the boundary will be bounced off. Since the momentum in the direction of

boundary does not change, electrons can move to the other side finally, forming the so called edge state. Suppose we have a defect on the edge, electrons are still scattered forward so this edge state is robust to disorder. The Hall conductivity σ is precisely quantized as

$$\sigma = \frac{I_{\text{channel}}}{V_{\text{Hall}}} = \upsilon \frac{e^2}{h} \tag{1.1}$$

where I_{channel} is the channel current, V_{Hall} is the Hall voltage. The prefactor υ is called filling factor, which can take value of only integer (υ =1, 2, 3,…). This phenomenon was recognized to be topological by Thouless, Kohmoto, Nightingale, and den Nijs (TKNN).[24] TKNN showed that the filling factor in Eq. (1.1) is given by the TKNN invariant (or first Chern number):

$$\upsilon = \frac{1}{2\pi} \int_{BZ} \left[\nabla_{\mathbf{k}} \times \mathbf{A}(k_x, k_y) \right]_z d^2\mathbf{k} \tag{1.2}$$

with

$$\mathbf{A} = i \sum_{m=1}^{N} \langle u_m \,|\, \nabla_{\mathbf{k}} \,|\, u_m \rangle \tag{1.3}$$

where $\{u_m(\mathbf{k})\}$ are a set of N occupied Bloch wavefuncitons which describe the many body ground state, the integral is taken over the Brillouin zone. $\mathbf{A}$ is Berry's connection and $\nabla_{\mathbf{k}} \times \mathbf{A}(\mathbf{k})$ is Berry's curvature. If one changes the Hamiltonian of the system smoothly, the topological first Chern number does not change, indicating that the QH state does not change, so the edge state is preserved. In this sense, we say that the edge state is protected topologically.

Since the realization of QH effect (QHE) requires strong magnetic field, we may want to know if we can get a similar phase as the QH states without magnetic field. This possibility is argued in a paper by B. A. Bernevig *et al.*[25] First, we should know that the Landau levels in QHE are responsible for the quantized Hall conductance, while the Landau levels arise physically from Lorentz force $\mathbf{F} = q(\mathbf{v} \times \mathbf{B})$, which is a velocity dependent force. In the Hamiltonian, this velocity dependent force contributes a term proportional to

$$H_{Lorentz} \propto \frac{Bq}{4m}\left(xp_y - yp_x\right) \tag{1.4}$$

where we suppose *z* is the magnetic direction. In the nature, the only other ubiquitous velocity dependent force is spin-orbit coupling (SOC) force, which contributes a term proportional to $\lambda_R(\nabla V \times \boldsymbol{p}) \cdot \boldsymbol{\sigma}$ in the Hamiltonian, here $\boldsymbol{p}$ is the momentum, ∇V is the electric field and $\boldsymbol{\sigma}$ is the Pauli matrices. For some special cases,[25] we can rewrite the term as

$$H_{SO} \propto \lambda_R \sigma_z \left(xp_y - yp_x\right) \tag{1.5}$$

where λ_R is the SOC constant. By comparing (1.4) and (1.5), we find that electrons with SOC experience an effective magnetic field. Moreover, the effective magnetic field points to different directions for the spin-up and spin-down electrons. Now if we look at the spin-up electrons, they form a set of chiral edge state as in QH state, as shown in Fig. 1.3. Spin-down electrons form another set of chiral edge state that have opposite chirality due to opposite effective magnetic field. Red and blue solid lines indicate the conducting channels for spin-up and spin-down electrons, respectively. We call these edge states

helical edge states in the sense that at each conducting edge, the different spin electrons are counter-propagating. Now we want to know if these states are robust or not. Suppose the right propagating spin-up electrons at the top edge of Fig. 1.3 are scattered backward to the opposite momentum, they must reverse their spin direction as well, which is forbidden in time-reversal invariant system (no external magnetic field and no magnetic impurities). In this sense, we say that the edge state is protected by TRS. This state is called quantum spin Hall effect (QSHE), and later named 2D topological insulator (TI).

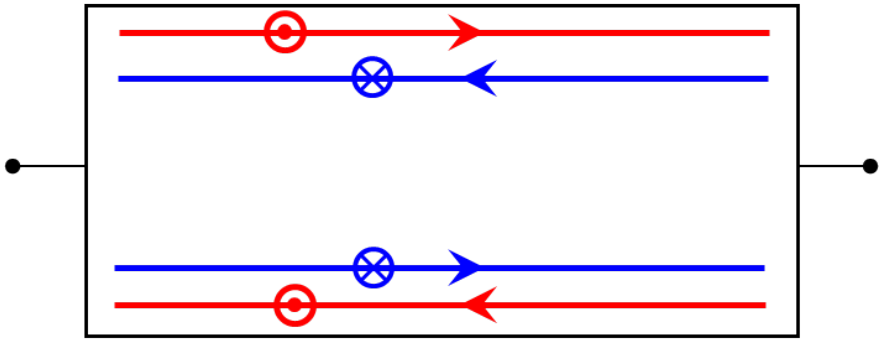

Fig. 1.3. Helical edge state of QSHE. Red and blue indicate spin up and spin down; arrows indicate momentum direction.

In 2005, Kane and Mele[26] showed that 2D TI can be characterized by a new type of topological invariant number Z_2, which takes value of either 1 or 0. If $Z_2 = 1$, the system is 2D TI. If $Z_2 = 0$, the system is anything else but 2D TI. They also proposed that graphene could be the 2D TI.[26, 27] Unfortunately, the SOC in graphene is so weak that it is impossible to observe the 2D TI effect experimentally. Soon after Kane and Mele's papers, in 2006, Bernevig, Hughes, and Zhang[28] proposed that 2D TI can be realized in CdTe/HgTe/CdTe quantum well, which was verified by transport measurement[29] in 2007.

1.2.2 From 2D TI to 3D TI

Soon after the theory of 2D TI, three theoretical groups[30-32] independently proved that the 2D TI could be generalized to 3D. There are four Z_2 invariants that can take value of either 1 or 0, *i.e.*, (ν_0; ν_1 ν_2 ν_3). A 3D system is strong TI if $\nu_0 = 1$. A 3D system is weak TI if $\nu_0 = 0$ and at least one of ν_1, ν_2 and ν_3 equals to 1. Only surface states of strong TI are robust to disorder and a TI (without strong or weak in front) usually indicates strong TI in literature. In 2007, Fu and Kane[33] predicted that $Bi_{1-x}Sb_x$ alloys are 3D TI with x ranges from 0.07 to 0.22. This prediction was soon verified by ARPES measurement.[34, 35] The bulk energy gap of this alloy is < 30 meV and it is classified as the first generation TI. In 2009, Zhang *et al.*[36] predicted that Bi_2Se_3, Bi_2Te_3, and Sb_2Te_3 are TI with bulk energy gap > 0.1 eV. At almost the same time, Xia *et al.*[37] also predicted that Bi_2Se_3 is a TI and their ARPES measurement clearly showed that there is a single Dirac cone at the surface. In the same year, Bi_2Te_3[38, 39] and Sb_2Te_3[39] were also verified to be TI by APRES measurement. These materials are classified as the second generation TI.

ARPES measurement is a common way to verify 3D TI. Another experimental method to verify topological surface state (TSS) is STM/STS. Usually two features of TSS are identified by STM/STS. First, quantized Landau levels of 2DEG with parabolic dispersion are equally spaced in strong magnetic field; Landau level energies of mass less Dirac fermions, including TSS, are proportional to $\sqrt{N}$ and the zero-energy Landau level is pinned to Dirac point. STS could detect Landau levels as peaks[40-43] in dI/dV spectroscopy. Second, the scattering by defects is reduced for TSS than normal surface states and the local density of states (LDOS) near the step could be different from normal surface states;[44-46] quasiparticle interference (QPI) patterns could also show evidence of

the topologically protected surface states.[47-51] The method of getting QPI patterns by STS will be introduced in detail in Section 2.1.3.

1.3 Motivation and synopsis of this thesis

Sb has been intensively studied recently due to the strong SOC[52, 53] and especially its unique TSS.[33, 35, 46, 49, 54] However, Sb bulk is semimetal[55] instead of insulator. The practical application of TSS is possible only if the bulk is an insulator. For ideal freestanding thin film in a vacuum, electrons are confined in the finite thickness, leading to quantized energy levels. The top valence band and bottom conduction band can shift downward and upward in energy, respectively, due to quantum confinement, so the bulk would possibly open a gap, making Sb thin film a TI if the surface states are still TSS. It is also possible that the surface states become spin degenerate due to coupling of states from two surfaces (inter-surface coupling) when their penetration depth is comparable with the film thickness.

The above argument is based on the assumption that the film is freestanding with two surfaces exposed to vacuum. For real thin films, the bottom surface is normally in contact with a substrate. The different environments of two surfaces break the space inversion symmetry in surface normal direction, and may affect the surface states. In addition, atoms at or near the surface may relax or reconstruct to reduce the surface energy. Electronic properties are sensitive to the atomic structures, thus relaxation and reconstruction may affect the surface states.

This thesis will cover these topics using the specific example of Sb(111) and Sb(110) thin films or islands. This thesis is organized as follows. In Chapter 2, a concise introduction to the experimental setup of STM and LEED as well as the substrates used in the experiment, *i.e.* Si(111)-7×7, Si(111)-$\sqrt{3}\times\sqrt{3}$:Bi and highly ordered pyrolytic graphite (HOPG), is given. The lattice structure and electronic properties of bulk Sb and bulk Sb(111) surface are briefly described.

In Chapter 3, the method for growing ultrathin Sb(111) atomic flat films is introduced. Sb nanostructures growing on Si(111)-7×7 at different substrate temperatures are investigated.

In Chapter 4, first, our *in-situ* STM studies on 30 and 9 BL Sb(111) films are given. For 30 BL Sb(111), surface states are bulk-like without inter-surface coupling. For 9 BL Sb(111), the QPI patterns can only be interpreted by considering the inter-surface coupling. Experimental results of 30 and 9 BL films can be simulated based on freestanding Sb(111) thin films. Calculations of 4 BL freestanding thin film showed an surface energy gap at $\bar{\Gamma}$, while the ARPES measurement showed no surface energy gap,[56] due to space inversion asymmetry (SIA) introduced by the substrate. Motivated by this result,[56] the SIA effect is simulated by replacing an Sb atom with a Bi atom in each unit cell. The mechanism that how the SIA hindered inter-surface coupling near $\bar{\Gamma}$ is discussed in detail. The calculated Fourier transform of QPI pattern is in good agreement with the experimental result.

In Chapter 5, Sb(110) thin films on HOPG are investigated. The 1, 3 and 5 ML Sb(110) are not observed in experiment. First-principles calculations indicate that

ultrathin Sb(110) relaxes and the Sb(110) films at 1, 3 and 5 ML thickness are not stable. Repeatable QPI patterns on ultrathin Sb(110) are not observed. The existence of the TSS is supposedly not related to the surface index,[54] *i.e.*, if Sb(111) possesses TSS, so does Sb(110). The relaxation of ultrathin Sb(110) is partly responsible for the disappearance of the surface states. Additionally, 4× reconstruction forms at the edge along $[0\bar{1}1]$ direction at certain conditions.

Finally, conclusions to this thesis and recommendations for further research are given in Chapter 6.

References

[1] M. Valden, X. Lai, D. W. Goodman, Onset of catalytic activity of gold clusters on titania with the appearance of nonmetallic properties. *Science* **281**, 1647 (1998).

[2] C. R. Henry, Surface studies of supported model catalysts. *Surface Science Reports* **31**, 235 (1998).

[3] R. D. McMichael, R. D. Shull, L. J. Swartzendruber, L. H. Bennett, R. E. Watson, Magnetocaloric effect in superparamagnets. *Journal of Magnetism and Magnetic Materials* **111**, 29 (1992).

[4] I. Anton, I. de Sabata, L. Vékás, Application orientated researches on magnetic fluids. *Journal of Magnetism and Magnetic Materials* **85**, 219 (1990).

[5] M. N. Baibich *et al.*, Giant Magnetoresistance of (001)Fe/(001)Cr Magnetic Superlattices. *Physical Review Letters* **61**, 2472 (1988).

[6] M. C. Daniel, D. Astruc, Gold nanoparticles: Assembly, supramolecular chemistry, quantum-size-related properties, and applications toward biology, catalysis, and nanotechnology. *Chemical Reviews* **104**, 293 (2004).

[7] A. G. Cullis, L. T. Canham, P. D. J. Calcott, The structural and luminescence properties of porous silicon. *Journal of Applied Physics* **82**, 909 (1997).

[8] Y. Wang, N. Herron, Nanometer-sized semiconductor clusters: materials synthesis, quantum size effects, and photophysical properties. *Journal of Physical Chemistry* **95**, 525 (1991).

[9] H. W. Kroto, J. R. Heath, S. C. O'Brien, R. F. Curl, R. E. Smalley, C60: Buckminsterfullerene. *Nature* **318**, 162 (1985).

[10] H. W. Kroto, A. W. Allaf, S. P. Balm, C60: Buckminsterfullerene. *Chemical Reviews* **91**, 1213 (1991).

[11] S. Iijima, Helical microtubules of graphitic carbon *Nature* **354**, 56 (1991).

[12] K. S. Novoselov *et al.*, Electric Field Effect in Atomically Thin Carbon Films. *Science* **306**, 666 (2004).

[13] D. M. Eigler, E. K. Schweizer, Positioning single atoms with a scanning tunnelling microscope. *Nature* **344**, 524 (1990).

[14] M. F. Crommie, C. P. Lutz, D. M. Eigler, Confinement of Electrons to Quantum Corrals on a Metal Surface. *Science* **262**, 218 (1993).

[15] M. C. Payne, M. P. Teter, D. C. Allan, T. A. Arias, J. D. Joannopoulos, Iterative minimization techniques for ab initio total-energy calculations: molecular dynamics and conjugate gradients. *Reviews of Modern Physics* **64**, 1045 (1992).

[16] P. Hohenberg, W. Kohn, Inhomogeneous Electron Gas. *Physical Review* **136**, B864 (1964).

[17] W. M. C. Foulkes, L. Mitas, R. J. Needs, G. Rajagopal, Quantum Monte Carlo simulations of solids. *Reviews of Modern Physics* **73**, 33 (2001).

[18] K. Oura, V.G. Lifshits, A.A. Saranin, A.V. Zotov, M. Katayama, *Surface Science: An Introduction*. Germany: Springer, 2003.

[19] R. L. Schwoebel, E. J. Shipsey, Step Motion on Crystal Surfaces. *Journal of Applied Physics* **37**, 3682 (1966).

[20] G. Ehrlich, F. G. Hudda, Atomic View of Surface Self-Diffusion: Tungsten on Tungsten. *The Journal of Chemical Physics* **44**, 1039 (1966).

[21] L. D. Landau, *Collected papers of L.D. Landau*. (Pergamon Press, 1965).

[22] X. G. Wen, *Quantum Field Theory of Many-Body Systems: From the Origin of Sound to an Origin of Light and Electrons*. (Oxford University Press, Oxford, 2004).

[23] K. v. Klitzing, G. Dorda, M. Pepper, New Method for High-Accuracy Determination of the Fine-Structure Constant Based on Quantized Hall Resistance. *Physical Review Letters* **45**, 494 (1980).

[24] D. J. Thouless, M. Kohmoto, M. P. Nightingale, M. den Nijs, Quantized Hall Conductance in a Two-Dimensional Periodic Potential. *Physical Review Letters* **49**, 405 (1982).

[25] B. A. Bernevig, S.-C. Zhang, Quantum Spin Hall Effect. *Physical Review Letters* **96**, 106802 (2006).

[26] C. L. Kane, E. J. Mele, Z_2 Topological Order and the Quantum Spin Hall Effect. *Physical Review Letters* **95**, 146802 (2005).

[27] C. L. Kane, E. J. Mele, Quantum Spin Hall Effect in Graphene. *Physical Review Letters* **95**, 226801 (2005).

[28] B. A. Bernevig, T. L. Hughes, S.-C. Zhang, Quantum Spin Hall Effect and Topological Phase Transition in HgTe Quantum Wells. *Science* **314**, 1757 (2006).

[29] M. Konig *et al.*, Quantum Spin Hall Insulator State in HgTe Quantum Wells. *Science* **318**, 766 (2007).

[30] J. E. Moore, L. Balents, Topological invariants of time-reversal-invariant band structures. *Physical Review B* **75**, 121306 (2007).

[31] L. Fu, C. L. Kane, E. J. Mele, Topological insulators in three dimensions. *Physical Review Letters* **98**, 106803 (2007).

[32] R. Roy, Topological phases and the quantum spin Hall effect in three dimensions. *Physical Review B* **79**, 195322 (2009).

[33] L. Fu, C. L. Kane, Topological insulators with inversion symmetry. *Physical Review B* **76**, 045302 (2007).

[34] D. Hsieh *et al.*, A topological Dirac insulator in a quantum spin Hall phase. *Nature* **452**, 970 (2008).

[35] D. Hsieh *et al.*, Observation of Unconventional Quantum Spin Textures in Topological Insulators. *Science* **323**, 919 (2009).

[36] H. Zhang *et al.*, Topological insulators in Bi2Se3, Bi2Te3 and Sb2Te3 with a single Dirac cone on the surface. *Nature Physics* **5**, 438 (2009).

[37] Y. Xia *et al.*, Observation of a large-gap topological-insulator class with a single Dirac cone on the surface. *Nature Physics* **5**, 398 (2009).

[38] Y. L. Chen *et al.*, Experimental Realization of a Three-Dimensional Topological Insulator, Bi_2Te_3. *Science* **325**, 178 (2009).

[39] D. Hsieh *et al.*, Observation of Time-Reversal-Protected Single-Dirac-Cone Topological-Insulator States in Bi_2Te_3 and Sb_2Te_3. *Physical Review Letters* **103**, 146401 (2009).

[40] P. Cheng *et al.*, Landau Quantization of Topological Surface States in Bi2Se3. *Physical Review Letters* **105**, 076801 (2010).

[41] Y. Jiang *et al.*, Landau Quantization and the Thickness Limit of Topological Insulator Thin Films of Sb_2Te_3. *Physical Review Letters* **108**, 016401 (2012).

[42] T. Hanaguri, K. Igarashi, M. Kawamura, H. Takagi, T. Sasagawa, Momentum-resolved Landau-level spectroscopy of Dirac surface state in Bi_2Se_3. *Physical Review B* **82**, 081305 (2010).

[43] Y. Okada *et al.*, Visualizing Landau Levels of Dirac Electrons in a One-Dimensional Potential. *Physical Review Letters* **109**, 166407 (2012).

[44] Z. Alpichshev *et al.*, STM Imaging of Electronic Waves on the Surface of Bi_2Te_3: Topologically Protected Surface States and Hexagonal Warping Effects. *Physical Review Letters* **104**, 016401 (2010).

[45] J. E. Ortega *et al.*, Scattering of surface electrons by isolated steps versus periodic step arrays. *Physical Review B* **87**, 115425 (2013).

[46] J. Seo *et al.*, Transmission of topological surface states through surface barriers. *Nature* **466**, 343 (2010).

[47] P. Roushan *et al.*, Topological surface states protected from backscattering by chiral spin texture. *Nature* **460**, 1106 (2009).

[48] T. Zhang *et al.*, Experimental Demonstration of Topological Surface States Protected by Time-Reversal Symmetry. *Physical Review Letters* **103**, 266803 (2009).

[49] K. K. Gomes *et al.*, Quantum Imaging of Topologically Unpaired Spin-Polarized Dirac Fermions. *arXiv:0909.0921v2* (2009).

[50] G. Yao *et al.*, Evolution of Topological Surface States in Antimony Ultra-Thin Films. *Scientific Reports* **3**, 2010 (2013).

[51] A. Strozecka *et al.*, Unconventional spin texture of a topologically nontrivial semimetal Sb(110). *New J. Phys.* **14**, 103026 (2012).

[52] K. Sugawara *et al.*, Fermi Surface and Anisotropic Spin-Orbit Coupling of Sb(111) Studied by Angle-Resolved Photoemission Spectroscopy. *Physical Review Letters* **96**, 046411 (2006).

[53] T. Kadono *et al.*, Direct evidence of spin-polarized band structure of Sb(111) surface. *Appl. Phys. Lett.* **93**, 252107 (2008).

[54] J. C. Y. Teo, L. Fu, C. L. Kane, Surface states and topological invariants in three-dimensional topological insulators: Application to $Bi_{1-x}Sb_x$. *Physical Review B* **78**, 045426 (2008).

[55] Y. Liu, R. E. Allen, Electronic structure of the semimetals Bi and Sb. *Physical Review B* **52**, 1566 (1995).

[56] G. Bian, X. Wang, Y. Liu, T. Miller, T. C. Chiang, Interfacial Protection of Topological Surface States in Ultrathin Sb Films. *Physical Review Letters* **108**, 176401 (2012).

Chapter 2

Experimental Setup and Substrates

2.1 Scanning tunneling microscopy (STM)

The development of STM has proved to be an exciting achievement, especially in surface science. This technique offers the ability of obtaining high-resolution images. The lateral and vertical resolution for a good STM is 0.1 nm and 0.01 nm, respectively.[1] Furthermore, STM can get local density of states (LDOS), which is hard to get with other scientific instruments. The majority of experimental results in this thesis are based on STM. The working principles and instrument setup are introduced here.

2.1.1 Basic principles

STM is the practical application of a quantum mechanical phenomenon: quantum tunneling. The theory of 1D quantum tunneling is explained briefly as follows.

An electron with energy E moving in a potential $U(z)$ satisfies the Schrödinger equation,

$$-\frac{\hbar^2}{2m}\frac{d^2}{dz^2}\psi(z)+U(z)\psi(z)=E\psi(z) \tag{2.1}$$

If $U(z)$is a constant, *i.e.*, $U(z)=U$, in the region where $E > U$, Eq. (2.1) has solution,

$$\psi(z)=\psi(0)e^{\pm ikz} \tag{2.2}$$

where

$$k = \frac{\sqrt{2m(E-U)}}{\hbar} \tag{2.3}$$

is the wavevector.

In the region where $E < U$, Eq. (2.1) has solution,

$$\psi(z) = \psi(0)e^{-\kappa z} \tag{2.4}$$

where

$$\kappa = \frac{\sqrt{2m(U-E)}}{\hbar} \tag{2.5}$$

is the decay constant.

Solution (2.2) is in accordance with the classical situation, while (2.4) is forbidden in classical physics. $|\psi(0)|^2 e^{-2\kappa z}$ means a non-zero probability density of observing the electron near z, where $E < U$.

In a STM system, the tip and sample is so close that electrons from the sample can tunnel through the vacuum barrier into the tip, and *vice visa*, as shown in Fig. 2.1(a). For simplicity, we assume that the work functions Φ of the sample and the tip are the same. There is no net tunneling current without a bias voltage applied between the tip and sample. Fig. 2.1(b) shows that when a negative bias voltage -V is applied to the sample, there is a net tunneling current. Electrons in state ψ_n with energy E_n lying between E_F - eV and E_F have a chance to tunnel into the tip. According to Eq. (2.4), the probability p for an electron in state ψ_n to tunnel into the tip is,

$$p \propto |\psi_n(0)|^2 e^{-2\kappa z} \tag{2.6}$$

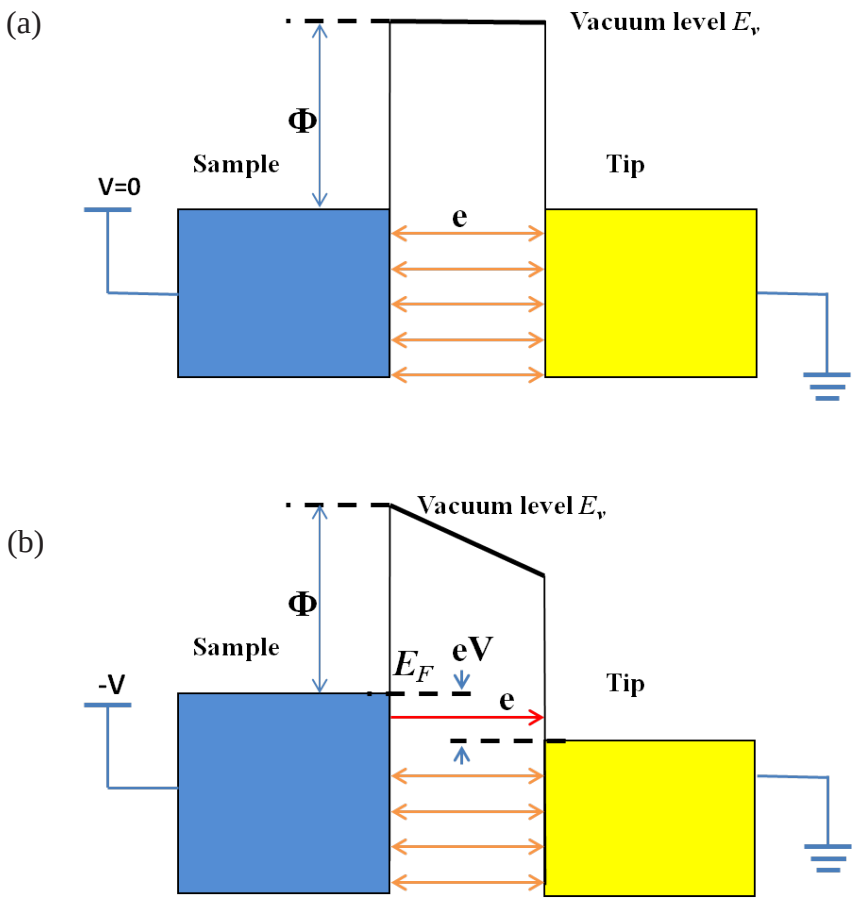

Fig. 2.1. Energy diagram of the tunneling junction of the STM tip and sample. For simplicity, we assume that the sample and tip have the same work function Φ. (a) Tip and sample are close but there is no bias voltage. Even though electrons from both sides can tunnel into each other (indicated by orange arrows), there is no net tunneling current. (b) Sample is negatively biased. There are net tunneling electrons from the sample to the tip (indicated by the red arrow). In this case, STM probes the filled states of the sample surface. If sample is positively biased, STM probes the empty states.

where the decay constant is $\kappa = \frac{\sqrt{2m(E_v - E_n)}}{\hbar}$ according to Eq. (2.5). For simplicity again , we assume eV << Φ, then all the energy levels E_n of interest are close to the Fermi level, *i.e.*, $E_v - E_n \approx E_v - E_F = \Phi$. Hence, we have,

$$\kappa = \frac{\sqrt{2m\Phi}}{\hbar} \tag{2.7}$$

By summing up all the states in $E_F - \mathrm{eV} \le E \le E_F$, the tunneling current is,

$$I \propto \sum_{E_n = E_F - eV}^{E_F} |\psi_n(0)|^2 e^{-2\kappa z} \tag{2.8}$$

The numerical value of Eq. (2.7) is $\kappa = 0.51\sqrt{\Phi(eV)}\,\text{Å}^{-1}$. Assuming Φ=4.8 *eV*, from Eq. (2.7) and (2.8), it could be seen that a change of *z* by 1 Å will cause about one order of magnitude change in current. This is why STM has a quite high vertical resolution.

However, for a full description of STM, 1D model is not enough. Most of the tunneling theories are based on the 'perturbative-transfer Hamiltonian' formalism introduced by Bardeen.[2] The electrons from both electrodes follow Fermi-Dirac distribution $f(E) = \{1 + \exp[(E - E_F)/k_B T]\}^{-1}$. With a bias voltage -V applied to the sample, as shown in Fig. 2.2, we have the total tunneling current as following,

$$I = \frac{2\pi e}{\hbar} \int \rho_s(E_F - eV + \varepsilon)\rho_t(E_F + \varepsilon)\left[f(E_F - eV + \varepsilon) - f(E_F + \varepsilon)\right] |M|^2 \, d\varepsilon \tag{2.9}$$

where *M* is tunneling matrix element, and $\rho_s(E)$ and $\rho_t(E)$ are the DOS of the sample and the tip, separately.

At low temperatures, the Fermi-Dirac distribution function can be approximated as a step function, hence the tunneling current (2.9) becomes

$$I = \frac{2\pi e}{\hbar} \int_0^{eV} \rho_s(E_F - eV + \varepsilon)\rho_t(E_F + \varepsilon) |M|^2 \, d\varepsilon \tag{2.10}$$

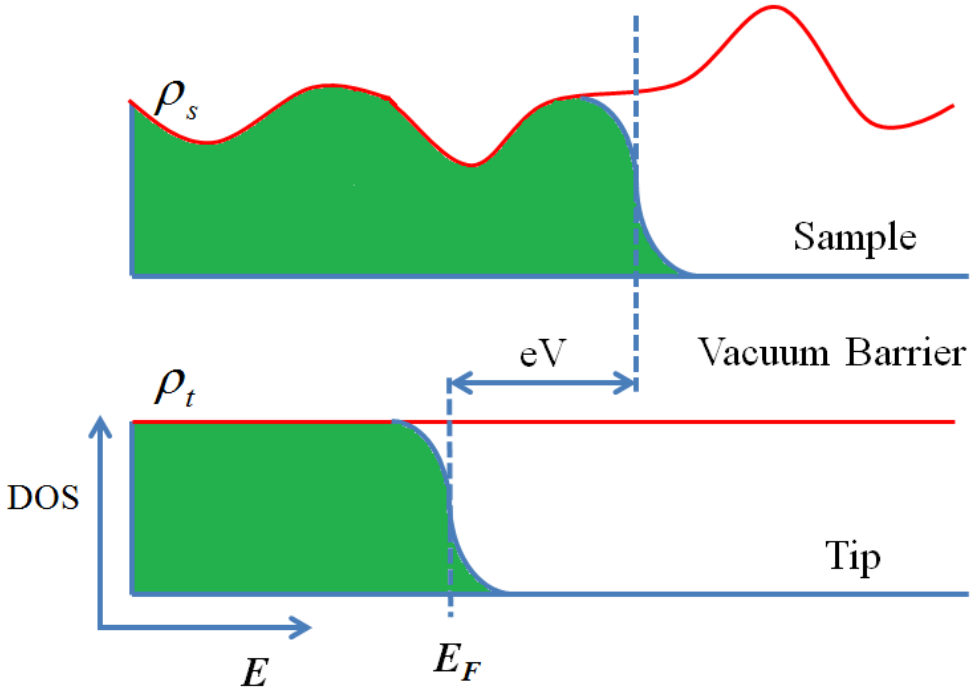

Fig. 2.2. The Bardeen approach to tunneling theory. Along the horizontal axis is the energy while the DOS is along the vertical one. The filled states are colored in green and the empty states are in white. The non-sharp edge transition from filled states to empty states arises from the Fermi-Dirac distribution when temperature T ≠ 0 K. The Fermi level of the sample is shifted from that of tip due to applied negative bias on the sample.

Bardeen[2] has shown that, for a small bias voltage, the magnitude of the tunneling matrix $|M|$ can be assumed as a constant in the interval of interest for interpretation of the experimental data, which makes the above equation even simpler:

$$I = \frac{2\pi e}{\hbar}|M|^2 \int_0^{eV} \rho_s(E_F - eV + \varepsilon)\rho_t(E_F + \varepsilon)d\varepsilon \qquad (2.11)$$

The above equation shows clearly that the tunneling current could be used as a tool to measure the DOS. Usually we use a metal tip, whose DOS could be considered to be constant over the energy range of interest. In this case, from Eq. (2.11), we have

$$\frac{dI}{dV} \propto \rho_s(E_F - eV) \tag{2.12}$$

Thus, the DOS of the sample surface is proportional to the tunneling conductance.

2.1.2 STM setup

Gerd Binnig, Heinrich Rohrer and their co-workers at IBM Research Laboratory invented the STM in the early 1980s.[3-6] They had tried to measure the spatial distribution of tunneling current between a tip and superconductor at a separation of about 1 nm. During this study, they recognized the possibility of achieving a tremendous high-resolution microscope based on scanning method. Binnig and Rohrer finally came up with atomic resolution by STM, which won them Nobel Prize in Physics in 1986.

From an instrumental point of view, an STM is composed of the following essential parts:

(1) An environmental control system. Since STM scanning operation is very sensitive to contamination on many sample surfaces, a UHV chamber is often required, which is evacuated by a group of vacuum pumps usually including rotary pump, turbo molecular pump and ion pump. Furthermore, for low temperature STM (LT-STM), temperature control system together with cryostat is needed.

(2) Since the tip and sample are so close and the tunneling current is very sensitive to the tip-sample distance, a little bit of vibration could dramatically vary the tunneling current, thereby introducing noise. A vibration isolation system to minimize the disturbance of mechanical vibration from the lab environment is needed. For example, spring suspension bench is employed to support the STM

head. In addition, sometimes air cushion platform is employed to support the whole STM system.

(3) An atomically sharpened tip. The tips we used are either commercially bought PtIr tips or electrochemically etched tungsten tips.

(4) Positioning system to select the target area on a sample surface, control the tip-sample distance, and scan the tip over the area with atomic resolution. A piezoelectric tube can implement this function.

(5) Since tunneling current is of nA order in magnitude, current amplifier is necessary to measure the tunneling current and a feedback loop to keep the tunneling current constant is also necessary.

(6) A computer system to control the STM controller, collect image data, display and process the images.

Fig 2.3 shows the schematic components of (3) to (6) mentioned above. A tunneling current in or less than the order of nA is detected by a current amplifier. The output of the amplifier is fed into a feedback circuit, which makes sure that the tip-sample separation is appropriate. Since the tip-sample separation is controlled by the voltage signal applied to the piezoelectric tube, tip height in a specific position could be tracked by recording the voltage. The tip height information for all pixels in one scanning frame can be used to convert to morphological image by computer programs.

Fig. 2.4 shows our two STM systems, Omicron room-temperature UHV STM (RT-STM) system and Unisoku low-temperature UHV STM (LT-STM) system. The latter can perform imaging at liquid nitrogen (LN_2) temperature (77K) or liquid helium (LHe) temperature (4.2K).

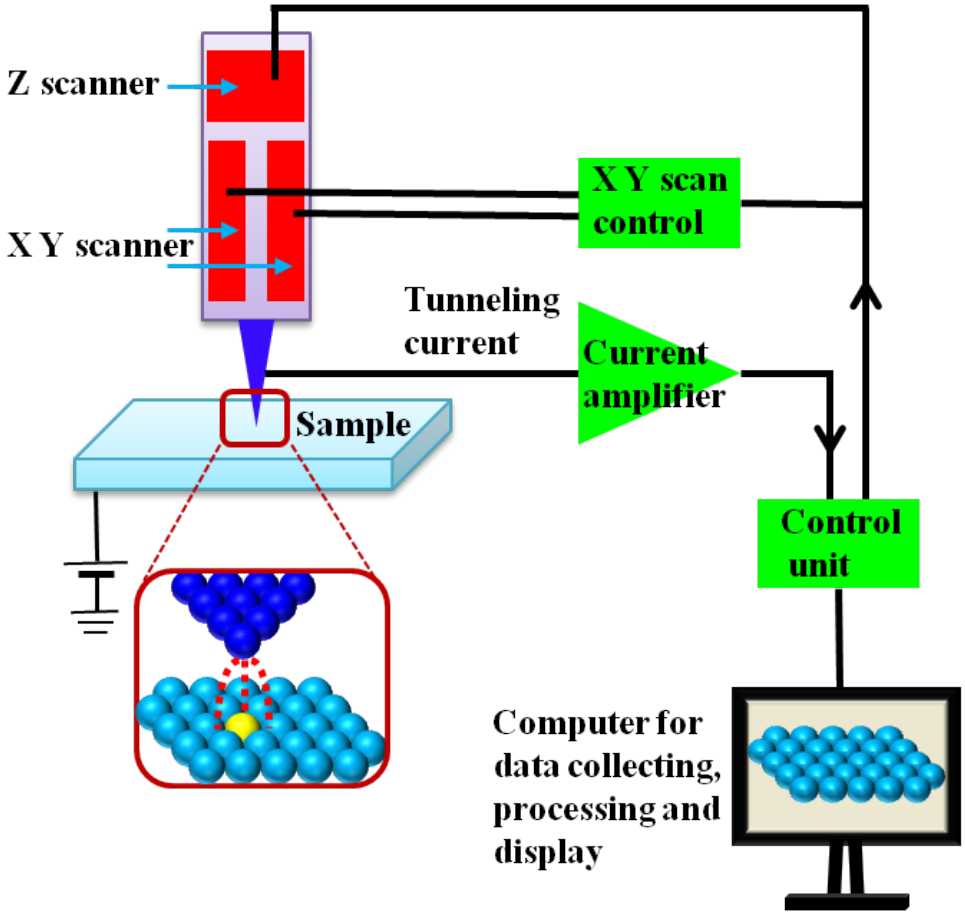

Fig. 2.3. Schematic view of STM essential components, including tip, positioning system, current amplifier, STM controller unit and computer system.

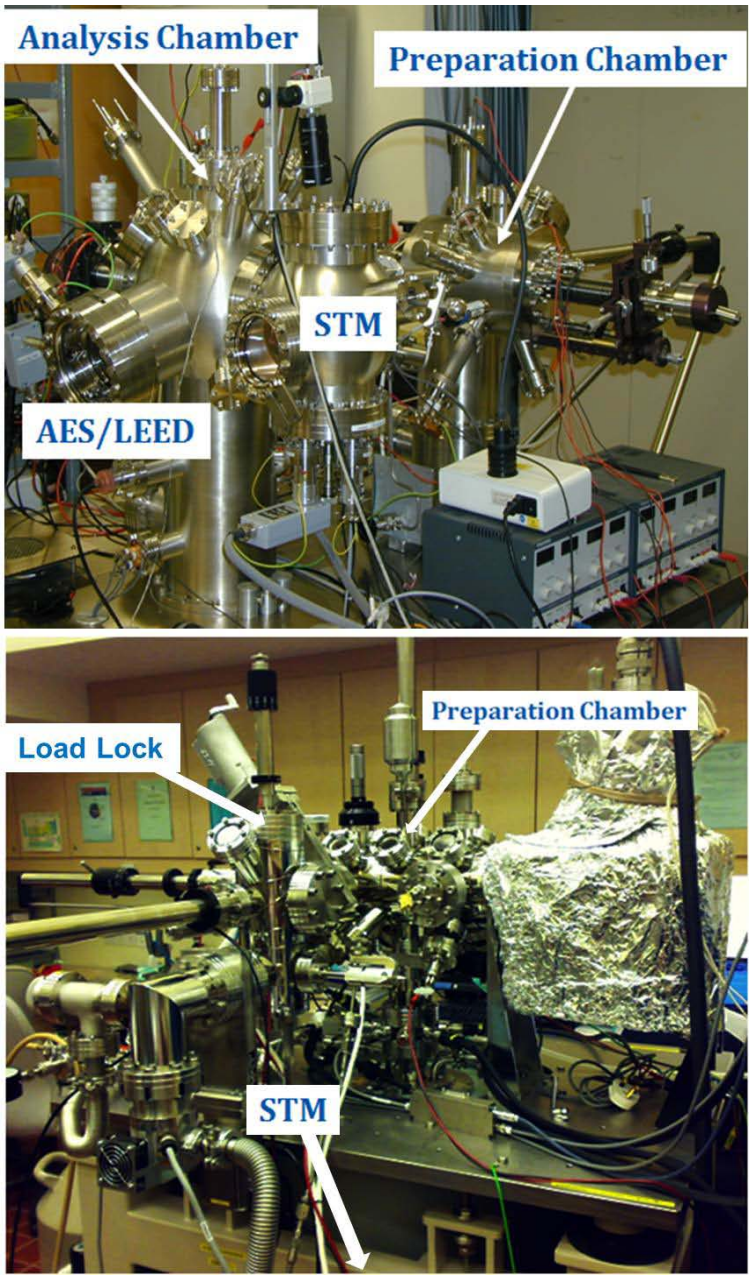

Fig. 2.4. Photos of Omicron UHV RT-STM system (top panel) and Unisoku UHV LT-STM system (bottom panel).

2.1.3 STM modes of operation

2.1.3.1 Topography

The most common mode of STM operation is topography. In our experiment for topography, STM is always working in constant current mode. The tip is adjusted vertically in such a way that tunneling current is fixed. The computer, according to the vertical position of the tip, generates a topographic image. STM can also work in constant height mode, in which the vertical position of the tip is unchanged. The current as a function of lateral position represents the topographic image. This mode is only suitable for atomically flat surfaces as otherwise the tip would crash inevitably. This mode, however, can work in very fast frequencies, as the current feedback loop is disabled and hence useful for fast STM.

2.1.3.2 Scanning tunneling spectroscopy (STS)

By interrupting the feedback loop so that the tip-sample distance is fixed, and applying a bias voltage ramp, the tunneling current as a function of bias voltage is recorded. According to Eq. (2.12), the differentiation of $I(V)$ with respect to V (differential conductance) provides a direct measure of LDOS of the sample surface. In practice, we could obtain LDOS through numerical differential of I-V curve. However, this technique generally results in noisy spectra. A better way is to measure $\mathrm{d}I/\mathrm{d}V$ directly using a lock-in amplifier. By adding a small AC modulation (~1-10 mV) to the applied voltage and measuring the corresponding AC current at the same frequency, one can effectively measure $\mathrm{d}I/\mathrm{d}V$. We use STS method in two ways, point spectroscopy and current image tunneling spectroscopy (CITS).

- **Point spectroscopy (d*I*/d*V* spectroscopy)**

In this mode, the tip position is fixed as we record d*I*/d*V* as a function of V. The result is a spectrum indicating the local DOS at a particular point on the surface. The ability to measure the local DOS allows the study of many condensed matter physics phenomena, such as superconductivity,[7] Landau levels[8] and Dirac fermions.[9]

- **Current imaging tunneling spectroscopy (CITS)**

In this mode, while the tip is scanning over the surface, the maps of tunneling spectra together with morphology are generated. At each pixel (*x*, *y*), we can measure *z* with feedback loop on at a fixed bias voltage V_0, then with the feedback loop interrupted, one records d*I*/d*V* as a function of V. Next, feedback loop is on again and the bias voltage is returned to V_0 and tip moves to the next pixel (*x'*, *y'*), starting the next cycle until all pixels in the selected scanning area are completed. Then we can take slices across this data to extract d*I*/d*V* at a given energy as a function of position, which is called a conductance map or STS image. However, this method is quite time consuming, taking ~10 hours for one CITS map. If we are interested in just a few energy values, it is faster to acquire the lock-in amplifier signal (d*I*/d*V*) at a fixed voltage as the tip is scanning over the sample surface. In this mode, a small voltage modulation of frequency ω is superimposed to the DC bias V_0, where ω is too fast for the feedback loop to follow. Then the current modulation at frequency ω from the lock-in amplifier are recorded to form the STS map at energy of eV_0.[1] If one is interested in the STS map at another energy eV_0', another scanning should be performed with the DC bias equals to V_0'.

The STS map is very powerful in imaging electronic wave interference patterns on surfaces, just as eyes could visualize the interference patterns of visible light. Fig. 2.5 shows a schematic view of an electron wave scattered by a defect. Interference of initial incoming state ($\boldsymbol{k_i}$) and final scattered state ($\boldsymbol{k_f}$) would give rise to a modulation of LDOS along the direction of $\boldsymbol{q}$ with periodicity of $|2\pi/\boldsymbol{q}|$, where $\boldsymbol{q} = \boldsymbol{k_f} - \boldsymbol{k_i}$, is the scattering wavevector. The modulation of LDOS can be shown in the STS map, which is also called quasi-particle interference (QPI) pattern. Hence, by performing a Fourier transformation (FT) of the STS map, we can get the FT-STS map, which contains information of $\boldsymbol{q}$, and hence gives us valuable information about the dispersion relations of surface bands.

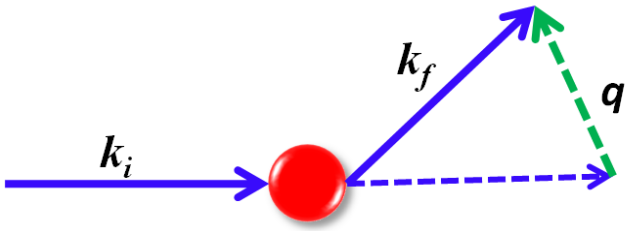

Fig. 2.5. The schematic view of scattering. Electronic surface state with an initial wavevector $\boldsymbol{k_i}$ is scattered to a different state with final wavevector $\boldsymbol{k_f}$ by a defect (red circle).

2.2 Low-energy electron diffraction (LEED)

2.2.1 Basic principles

LEED is a structural analysis technique that uses diffracted electrons. The spatial distribution of the diffracted electrons from a solid surface tells us about the crystal lattice. The incident electron energy is typically in the range 30-200 eV. From the de Broglie wavelength:

$$\lambda = \frac{h}{p} = \frac{h}{\sqrt{2m_e E_k}} = \frac{12.25}{\sqrt{E_k(\text{in eV})}} \text{ Å} \tag{2.13}$$

we get λ ranging from ~1-2 Å , which satisfies the diffraction conditions, i.e., λ is comparable to lattice constant. This energy range is roughly at the minimum in the universal inelastic mean free path curve. Thus, most elastic collisions occur in the top 1-2 atomic layers of the sample, making LEED surface sensitive, which provides mostly the 2D lattice structure of the sample surface. Fig 2.6(a) shows the schematic view of diffraction process on a 2D surface with normal incidence. The constructive interference occurs when the diffraction angle θ fulfills the following Bragg condition:

$$a \sin\theta = n\lambda \tag{2.14}$$

where n is an integer and λ is the wavelength.

Fig. 2.6(b) is the corresponding Ewald sphere construction of Fig. 2.6(a) in reciprocal space, for analyzing the diffraction patterns. To construct a 2D Ewald construction, one needs the following steps,[10]

- Construct the 2D reciprocal lattice.

- Draw the incidence wavevector k_0 along one rod, which is defined as the (00) rod.
- Draw a sphere of radius $2\pi/\lambda$ centered at the origin of k_0.
- Find all points of the sphere intersecting reciprocal lattice rods. Draw vectors indicating scatted wavevector pointing from the sphere center to all these points.

For 2D surface structure, we can regard the periodic repeat distance in surface normal direction to be infinite. Since the distance between adjacent points in a reciprocal lattice is inversely proportional to the corresponding distance in real space, the reciprocal lattice points along the surface normal are infinitely dense, forming rods. The radius of the Ewald sphere is the magnitude of the incident wavevector. The diffraction condition is satisfied for every beam that emerges in a direction along which the sphere intersects a reciprocal rod.

Mathematically, the incoming wavevector k_0 and diffracted wavevector k' are related with the 2D crystal reciprocal lattice by the condition:

$$k'^{//} - k_0^{//} = G_{hk} \tag{2.15}$$

where the superscript // indicates the wavevector components parallel to the surface, G_{hk} is the 2D reciprocal lattice vector. For normal incidence, $k_0^{//}=0$, so we have

$$k'^{//} = G_{hk} \tag{2.16}$$

If we collect the diffracted electrons, from (2.16) we get directly the reciprocal unit cell and from which one can deduce the 2D surface unit cell in real space.

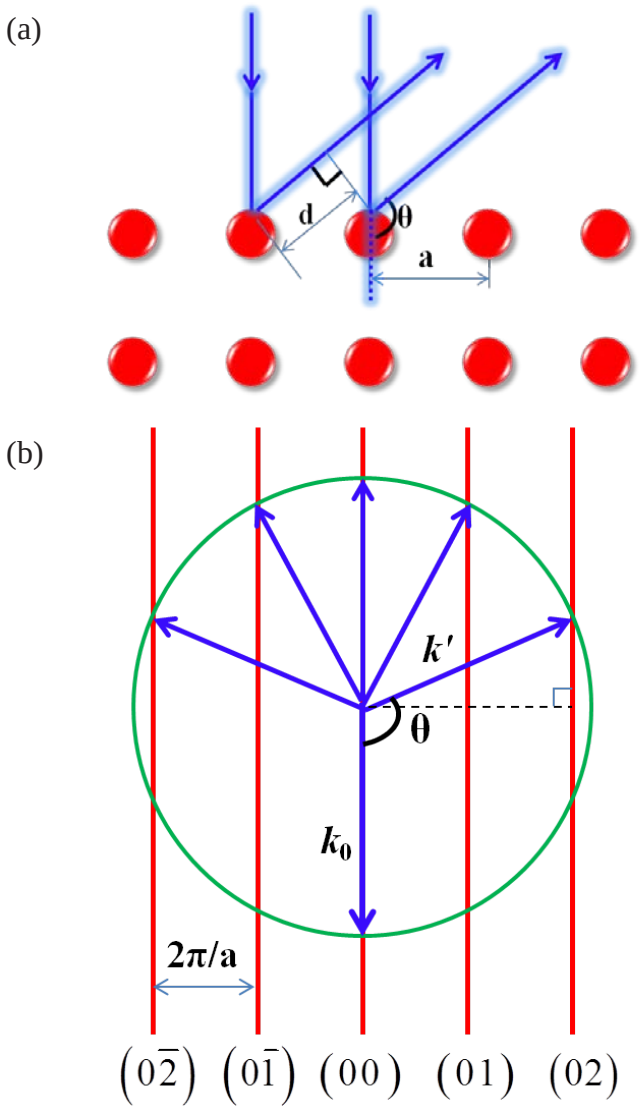

Fig. 2.6. (a) Schematic view of 2D diffraction process and, (b) the corresponding Ewald sphere construction in reciprocal space. Red lines indicate the 2D reciprocal-lattice rods. Blue arrows indicate the electron wavevector. θ is the diffraction angle. k_0 is the incident wavevector while k' is the diffracted wavevector. The two integers in each parenthesisare the subscript of the 2D reciprocal lattice vector G_{hk}.

2.2.2 LEED setup

Fig. 2.7(a) shows the schematic view of experimental setup of LEED which consists of two essential parts: an electron gun to produce a well-collimated beam with certain energy and a hemispherical fluorescent screen with a set of four grids to observe the diffraction pattern of the elastically scattered electrons.

The electron gun unit consists of a cathode filament with a Wehnelt cylinder and an electrostatic lens. G_1 is set at ground potential to set up field free region between the sample and G_1. The potential of G_2 and G_3 is at adjustable negative potential, close to that of the cathode but somewhat lower in magnitude. G_4 is set at ground potential to screen other grids from the field of the fluorescent screen, which is biased to a high voltage of about 5 kV. Electrons emitted by the cathode are accelerated in the gun unit, propagate to the sample, and then scattered by the sample surface elastically or inelastically. The inelastically scattered electrons, which may make up 99% of the total flux, have lower kinetic energy thus cannot pass through G_2 and G_3 to reach the fluorescent screen. The elastically backscattered electrons form a set of diffracted beams and arrive at the fluorescent screen, which provides the electrons with high enough energy to excite fluorescence because of its high positive potential. Since the screen is transparent, we can view the diffraction pattern from backside of the screen. This is the so-called reverse-view arrangement, in which case, electron gun is an obstacle between the view position and the screen thus should be minimized. We can also use the normal-view arrangement (view position is in front of the backside of the sample), in which case, the sample holder

is an obstacle thus should be small. Fig. 2.7(b) shows a typical LEED pattern of Si(111)-7×7 surface.

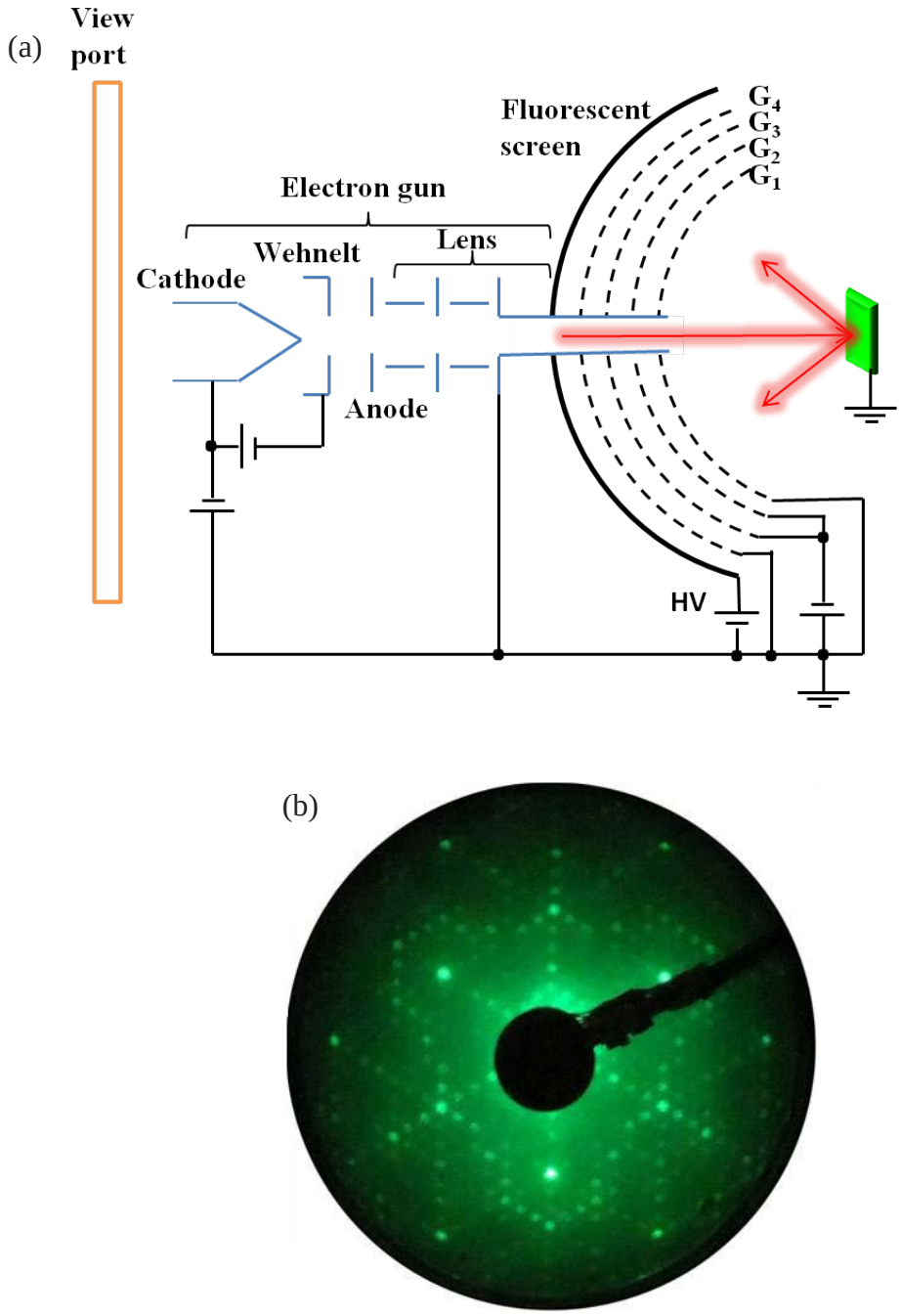

Fig. 2.7. Schematic view of a standard reverse-view four-grid LEED setup and (b) The LEED pattern of Si(111)-(7×7) surface (90 eV).

2.3 Substrate description

2.3.1 Si(111)-7×7

Silicon belongs to the face-centered cubic (FCC) group with a lattice constant of 5.43 Å. The basis of the lattice contains two atoms at (000) and $\left(\frac{1}{4}\frac{1}{4}\frac{1}{4}\right)$ of the FCC unit cube. Each atom has four nearest neighbors with a tetrahedral bond angle of $109^{\circ}28''$, which form the sp^3 hybridization.

Atomically clean Si(111) surface exhibits two main reconstructions, 7×7 and 2×1. The 2×1 reconstruction is produced by cleavage of Si along the (111) plane. This reconstruction was explained by π-bond chain model[11] and confirmed by Feenstra *et al.*[12] using STM. The 2×1 reconstruction is metastable and converts to 7×7 irreversibly upon annealing to about 500 ℃. The 7×7 reconstruction is stable up to about 850 ℃, above which the 7×7 reconstruction undergoes order-disorder transition. This transition is reversible, and upon cooling down to the transition temperature, the 7×7 reconstruction is restored. In our experiment, the 7×7 reconstruction was obtained by heating up the commercially available Si(111) wafer up to 1250 ℃ for about 10 seconds before cooling down to room temperature to get rid of oxide layer.

Si(111)-(7×7) reconstruction is very sophisticated, which was first observed in 1959 by LEED.[13] The satisfied explanation showed up in 1985 when Takayangi *et al.*[14] proposed the famous dimer-adatom-stacking fault (DAS) model. As shown in Fig. 2.8(a).

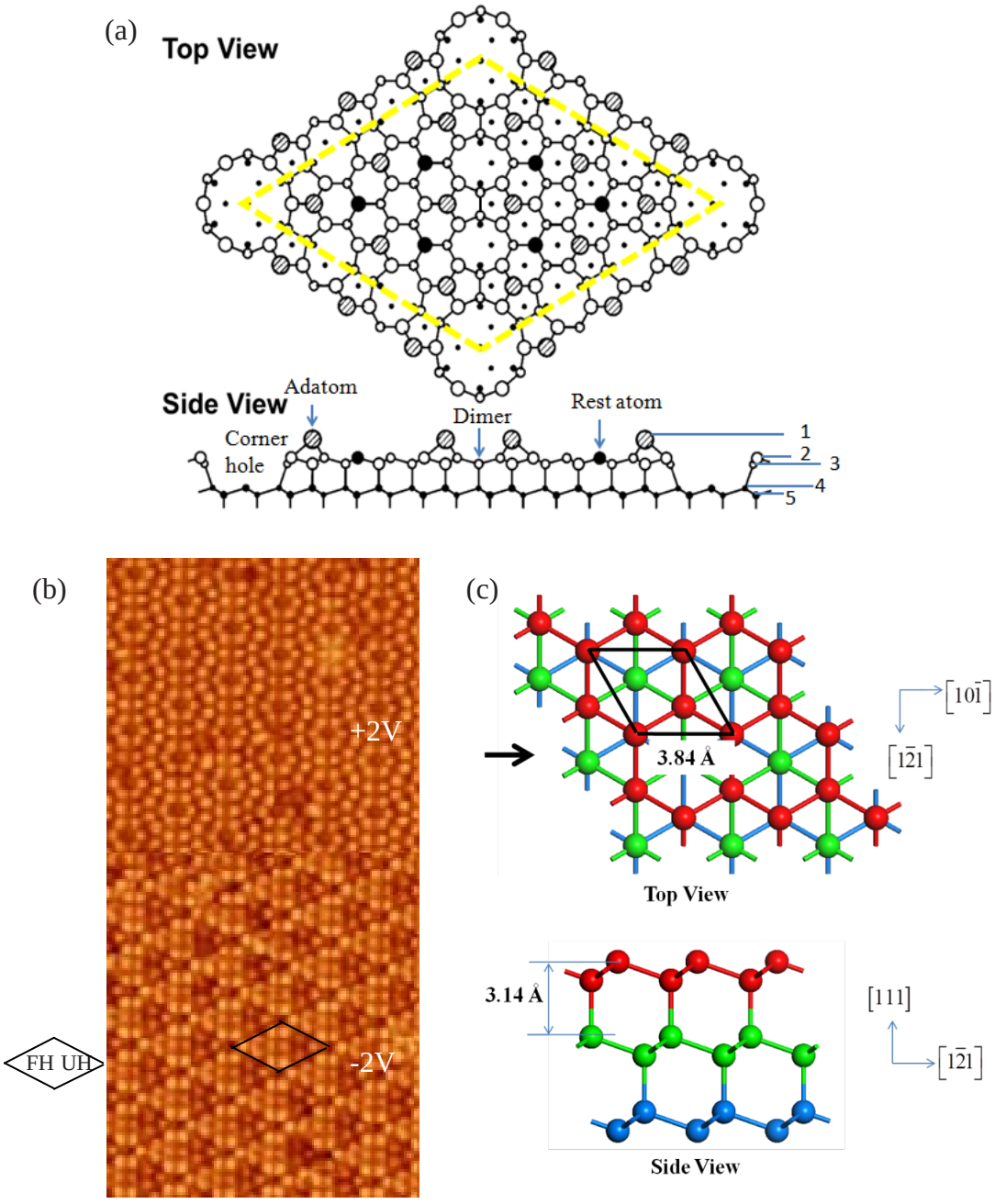

Fig. 2.8. (a) The DAS model of Si(111)-7×7 structure. (b) An atomic-resolution STM image of Si(111)-7×7, which shows the empty/filled states taken with positive/negative sample bias. The black rhombus indicates one 7×7 unit cell. (c) Schematic diagram of the ideal non-reconstructed Si(111) surface. The side view is from the direction as indicated by the black arrow shown in the top view figure.

In Fig. 2.8(a), the integers in the side view indicate the atomic layer numbers of the reconstruction. For each unit cell, there are 12 adatoms which occupy the T_4 sites above the second atomic layer. The second and third atomic layers form a Si(111) double layer, this double layer is alternatively faulted and unfaulted with respect to the underlying bulk (the fourth and fifth layer). So in Fig. 2.8(a) the left half in the yellow rhombus are called faulted half (FH) and the right half are called unfaulted half (UH). In each half 6 atoms saturated 18 dangling bonds from the second atomic layer, leaving 3 atoms in the second atomic layer unsaturated, which are called rest atoms. There are 9 dimers formed in the third atomic layer, surrounding the two halves in each unit cell. At the corner of the unit cell, 12 atoms from the second and third atomic layer form a ring, which is called corner hole. At the centre of the corner hole, there is one atom from the fourth layer unsaturated. So this 7×7 DAS structure replaces 49 dangling bonds of the bulk-terminated Si(111) surface by 19 dangling bonds, including those of 12 adatoms, 6 rest atoms and 1 in the corner hole.

It is commonly believed that the bright spots in the STM images are due to the tunneling currents originating from these dangling bonds.[15] Fig 2.8(b) shows typical STM images of Si(111)-7×7 structure. The difference between top and bottom half are due to different sample bias V_s. The top half was obtained at V_s = +2 V, in which situation the tip detects the filled state of the sample, while the bottom half was obtained at V_s = -2 V and is an image of the filled state. From the filled state image, we can identify FH and UH by brightness: FH is brighter, as shown in the black rhombus.

Fig. 2.8(c) is the schematic view of the ideal bulk-terminated Si(111)-1×1 surface. The black rhombus indicates unit cell of the 1×1 bulk termination. The side view is along $\left[10\bar{1}\right]$ direction as indicated by the black arrow.

2.3.2 Si(111)-√3×√3:Bi

Si(111)-7×7 substrate may form (√3×√3)R30° reconstruction induced by adsorption of Bi atoms. There are two stable (√3×√3)R30° phases with Bi coverage equaling to 1/3 ML (α-phase) or 1 ML (β-phase).[16] For the α-phase, each Bi atom adsorbs at the T_4 site, and for the β-phase, three Bi atoms form a trimer centering at the T_4 site.[16, 17] Since each Bi atom or trimer saturates 3 dangling bonds, all atoms from Si(111) are saturated, thus Si(111)-√3×√3:Bi is inert compared with Si(111)-7×7. In this thesis, we only use β-phase Si(111)-√3×√3:Bi.

2.3.3 Highly ordered pyrolytic graphite (HOPG)

HOPG belongs to layered material. Within one atomic layer, each carbon atom connects with three nearest neighbors by very strong covalent bonds, forming a plane hexagonal structure with two equivalent sublattices, as shown in Fig 2.9(a). Atoms from the two sublattices are indicated by red and blue circles, respectively. The interlayer spacing is 3.354 Å and the adjacent layers are connected by weak Van der Waals force. As a result, the outermost surface of the graphite preserves the bulk-terminated structure without reconstruction, and the relaxation of the first layer is also small (0.05 Å of contraction, i.e., 1.5% of the bulk value).[18]

Ideally, the atomic-resolution STM image of HOPG should show two atoms in each unit cell, which makes the image a honeycomb atomic pattern, as shown in Fig 2.9(c). However, STM usually can only map out one sublattice, as shown in Fig 2.9(d). Six nearest neighbors surround each apparent spot, with a lattice constant of 2.46 Å. In fact, if one peels out only one atomic layer of HOPG, *i.e.*, graphene, one can map out two sublattices in one STM image, making the atomic-resolution image of graphene honeycomb. In a few cases, researchers could observe honeycomb structure by STM on HOPG, and they explain this as a result of weakened coupling between the topmost and the second atomic layers;[19, 20] the property of the observed honeycomb structure is like a piece of graphene. The clean HOPG surface could be prepared by simply peeling the surface using scotch tape. HOPG is very stable. It remains stable at 500℃ in air and over 2000℃ in vacuum or inert environment. Since the surface is chemically inert, it is a good substrate to study physisorption phenomena.

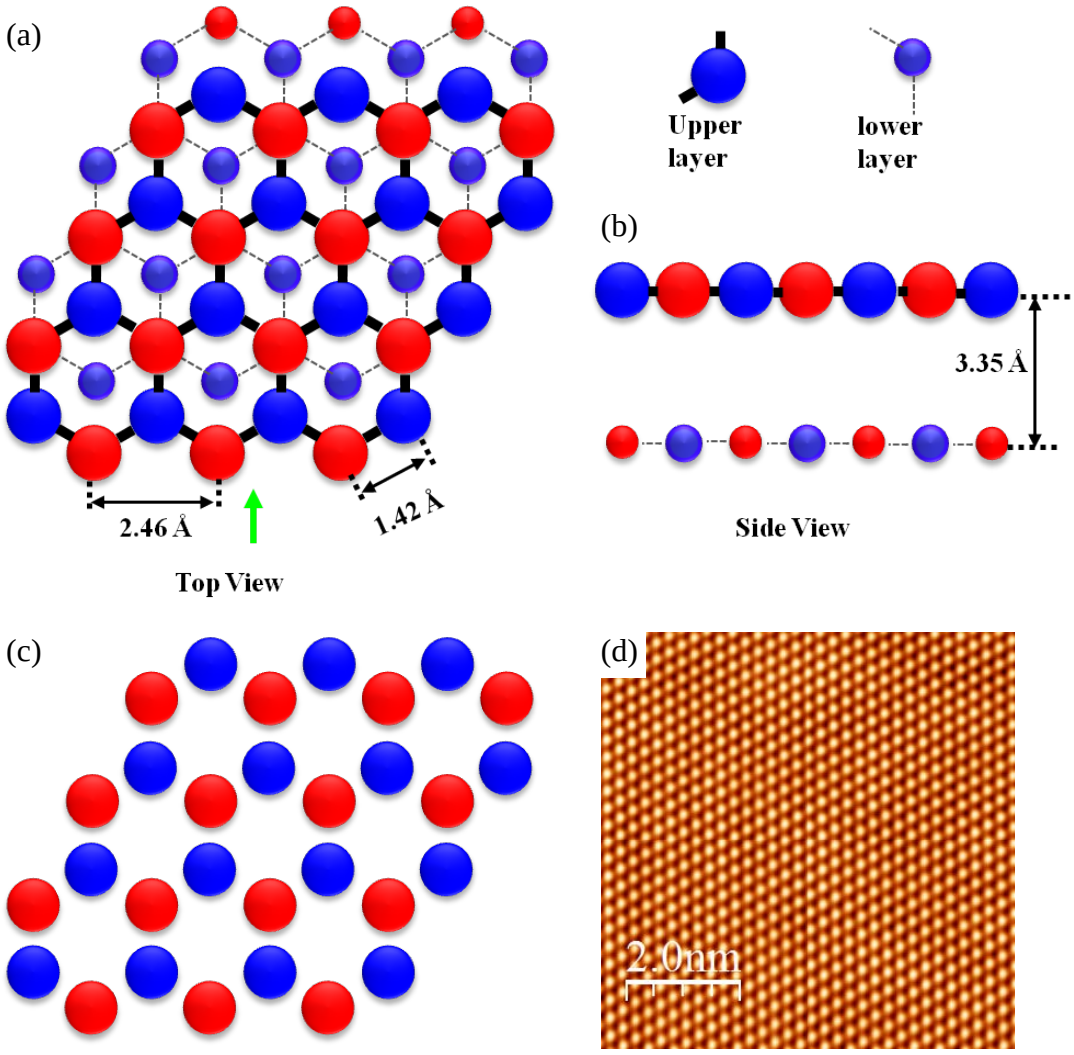

Fig. 2.9. (a) Schematic top view of HOPG (0001) surface and (b) side view from the direction as indicated by the green arrow in panel (a). (c) Schematic view of an ideal atomic-resolution STM image. (d) The atomic-resolution STM image of HOPG. The two sublattices are equivalent, usually only one of the two sublattices can be mapped out in one STM image.

2.4 A brief introduction to Sb crystal

2.4.1 Lattice structure of Sb

Sb is a prototypical group-V element. In ambient conditions, Sb crystallizes in the rhombohedral A7 structure with two atoms per unit cell, as shown in Fig. 2.10(a). Two different atoms in the unit cell are shown as blue and brown circles, respectively. The lattice is generated by three rhombus base vectors **a**, **b** and **c**. The angle between each two of the three base vectors is 57.1°.[21] This structure can be regarded as derived from the sodium chloride face centered cubic (FCC) structure.[22] First, replace both sodium and chloride sublattices with Sb. Then slightly stretch along a body diagonal to reduce the rhombohedral angle from 60° to 57.1°. Finally, move one sublattice relative to the other along the same body diagonal to make the ratio d_1/d_2 from 1 to 0.876. The direction of stretched diagonal of the FCC is the [111] direction in rhombohedral structure. Since rhombohedral structure can be derived by a slight distortion from cubic lattice, Sb also can be described by pseudocubic indices. In addition, Sb can be described by hexagonal indices. Rhombohedral indices are used in this thesis.

In Fig. 2.10(a), the three nearest atoms for the blue one are the three brown atoms below it, and the next nearest three atoms are three brown atoms above it. The blue atom is connected to three nearest neighbors by covalent bond within one puckered bilayer (BL). The covalent bonding within each BL is much stronger than the interbilayer van der Waals bonding, so Sb can easily cleave along (111) plane. Each Sb(111) BL forms a honeycomb structure, with two sublattices not within the same plane. The bilayers follow ABC-stacked structure in the bulk, as shown in Fig 2.10(b). Atoms in different layers are

indicated by different colors. The solid lines indicate covalent bonds. A black rhombus in the top-view image indicates the unit cell. STM can only map the upper sublattice of one BL, thus the STM image exhibits a hexagonal order instead of honeycomb, as shown in Fig. 2.10(d).

Fig. 2.10(c) schematically illustrates the ideal bulk-terminated Sb(110) surface. This surface is not a natural cleavage plane of Sb crystal, but we can get it from self-assembly growth method, which will be discussed in Chapter 5. A unit cell is shown as a black square in top-view image. The atom in the middle of the unit cell in the terminating layer (blue color circles) has three nearest neighbors and is saturated. However, the atom in the corner is connected covalently only to two nearest neighbors, and the dangling bonds are indicated by blue dash lines in the side-view images. Fig. 2.10(e) shows the atomic-resolution STM image of Sb(110) thin film; only one atom in each unit cell is observed in this image.

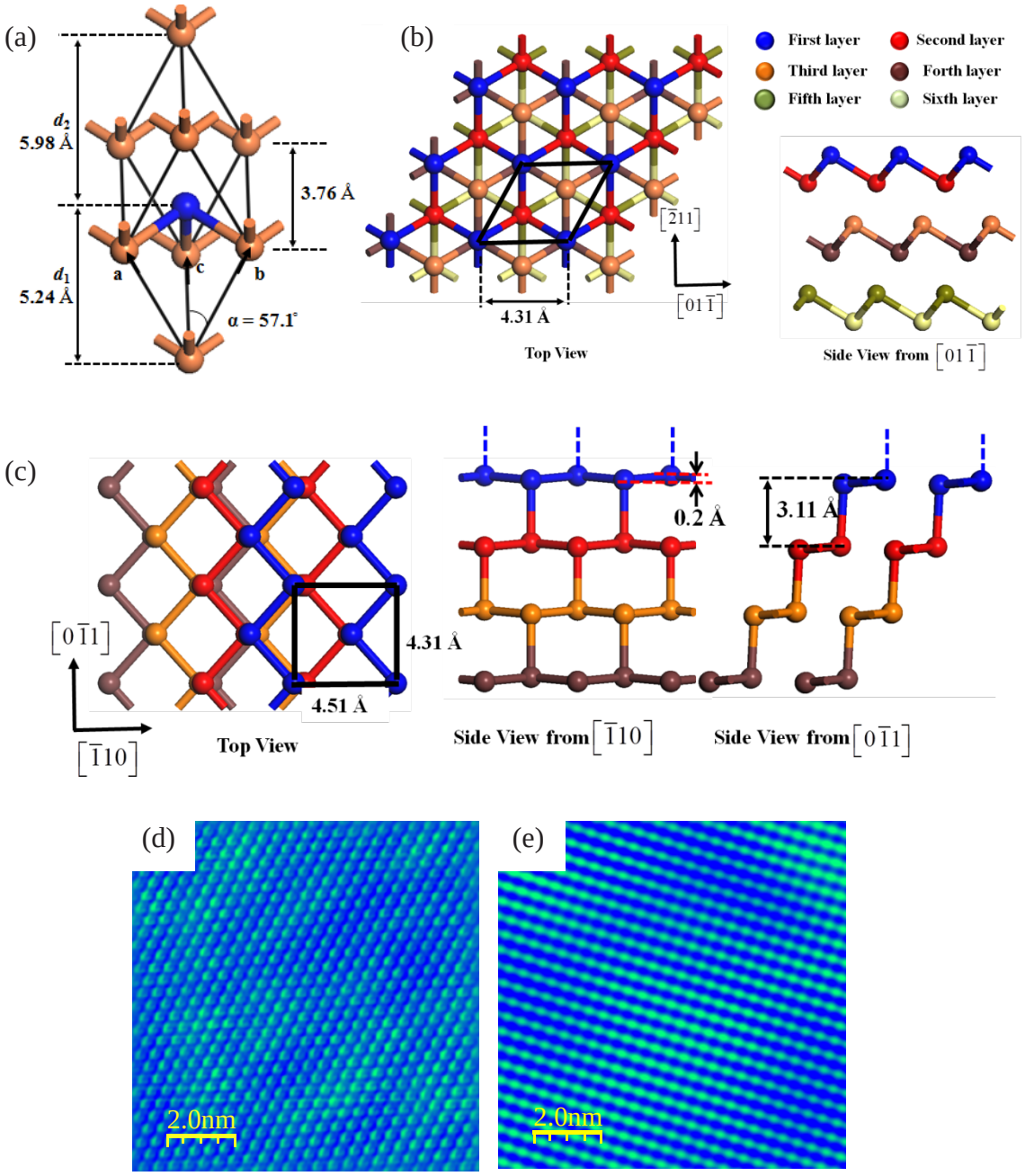

Fig. 2.10. (a) Schematic view of bulk Sb rhombohedral unit cell. Three base vectors are marked as **a**, **b** and **c**. (b) Schematic view of Sb(111) surface. (c) Schematic view of Sb (110) surface. (d) A 10×10 nm atomic-resolution STM image of Sb(111) thin film on Si(111)-$\sqrt{3}\times\sqrt{3}$:Bi substrate, at V_s = 1 V and tunneling current = 0.26 nA. (e) A 10×10 nm atomic-resolution STM image of Sb (110) thin film on HOPG substrate, at V_s = -0.01 V and tunneling current 0.11 nA.

2.4.2 Electronic structure of Sb

Sb is a semimetal with an indirect negative band gap because the conduction band minima at the *L* points is 174 meV lower than the valence band maxima at the *H* points.[21] Fig. 2.11(a) is the schematic of the bulk Brillouin zone (BZ) of rhombohedral structure and its (111) surface Brillouin zone (SBZ).[23] The *H* point is near *T* point and is on the mirror plane, with trigonal coordinates [0.4543, 0.3722, 0.3722].[21] Sb has attracted a lot of researchers' attention since the emergence of a new class of topological state, namely topological insulator (TI).[24] The first experimentally verified 3D TI is $Bi_{1-x}Sb_x$ alloy,[25] with $0.07 < x < 0.22$.[26] The $\nu_0 = 1$ topology of the $Bi_{1-x}Sb_x$ alloy is predicted to be inherited from the bulk wavefunctions of pure Sb.[26] The large atomic number of Sb leads to the strong spin-orbit coupling (SOC) which mixes *p* orbitals; the six bands nearest to the Fermi level have strongly mixed p_x, p_y and p_z character. Tight binding model calculations of Sb[21] show that the conduction band crosses Fermi level near the *L* points, where electrons pockets form. The bottom of the conduction band at *L* is derived from antisymmetric linear combination (L_a) of *p*-orbitals, while the next lower band is derived from symmetric linear combination (L_s) of *p*-orbitals, as shown in Fig. 2.11(b), where the bulk projected band structure on Sb(111) surface together with the surface states are schematically shown. This inversion between the L_a and L_s bands leads to the existence of topological surface states (TSS) in pure Sb crystal. [26]

Fig. 2.11(c) is the first-principles calculations of band structure of 15 BL Sb(111) along high symmetry directions. The red lines indicate the surface states where the crossover forms the Dirac cone. There are two main differences between this Dirac cone

and the common one in graphene. First, the Dirac cone on each surface of Sb(111) is spin non-degenerate. Second, on Sb(111), the lower part of the Dirac cone disperses to higher energy with larger *k* value before going down to connect to the valence band, *i.e.* the cone is strongly warped. The warping in $\bar{\Gamma}$-$\bar{M}$ direction is stronger than in $\bar{\Gamma}$-$\bar{K}$ direction. The detailed ARPES spectrum featuring the surface states in the dashed square is shown in the left of Fig. 2.11(d);[27] the right figure shows constant energy contour (CEC) at the Fermi surface. Besides the central electron pocket, there are 6 hole pockets in $\bar{\Gamma}$-$\bar{M}$ direction, arising from the warping of the Dirac cone. The highest energy of the warping surface state in $\bar{\Gamma}$-$\bar{K}$ direction is below the Fermi level in their work,[27] so there are only hole pockets in $\bar{\Gamma}$-$\bar{M}$ direction near Fermi level. The purple arrows show the spin direction of the surface states. For TSS, backscattering with 180° spin flip is absent[28] while it is allowed for other spin angle differences. The right of Fig. 2.11(d) clearly shows that at Fermi level, the 6 hole pockets open up more scattering channels. Thus from FT-STS maps, one can get many scattering wavevectors and extract much information about the surface states. Therefore, STS method is a good investigation technique for the studies of Sb(111) surface states. For example, J. Seo *et al.*[29] have recently demonstrated that the TSS of bulk cleaved Sb(111) can penetrate defects (atomic steps) with higher probability compared with non–TSS of common metals, such as copper, silver and gold.

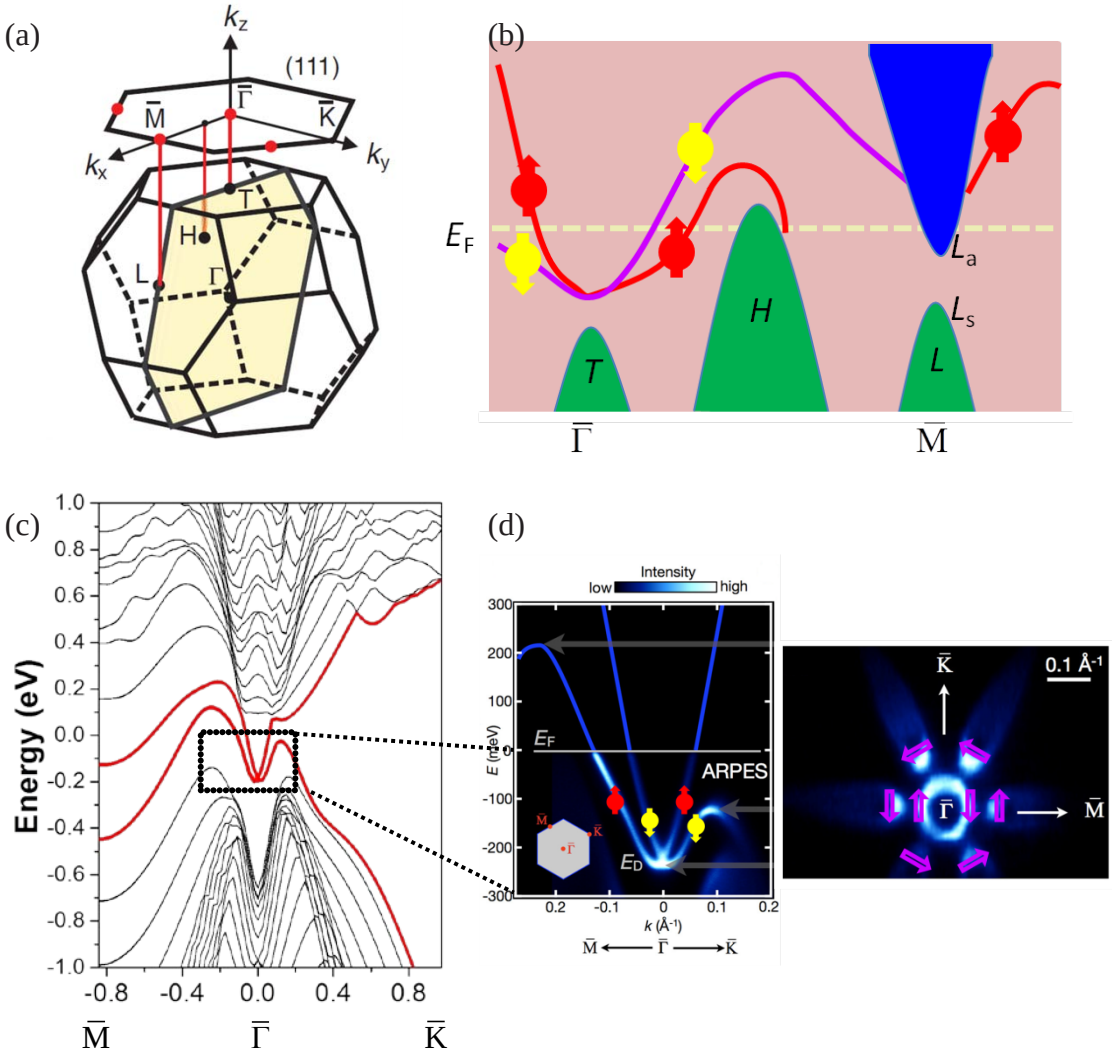

Fig. 2.11. (a) Schematic of the bulk 3D BZ of Sb and its (111) SBZ (Reprinted from Ref. [22] by permission of The American Association for the Advancement of Science). The faces in which *T* and *L* lie are regular and compressed hexagons, respectively. The SBZ is a regular hexagon. Γ and *L* points are projected to $\bar{\Gamma}$ and $\bar{M}$ of the SBZ, respectively. (b) Schematic diagram of the surface bands (red and purple lines) and the projected bulk bands (green and blue shaded area) onto (111) plane. The red and yellow arrows indicate the spin direction of the states. (c) First-principles calculations of band structure of 15 BL Sb(111) film along a $\bar{M}$-$\bar{\Gamma}$-$\bar{K}$ cut in *k*-space. The red lines indicate surface bands. (d) The left picture shows the ARPES measurement of bulk Sb(111) surface featuring the surface bands in the dashed square of panel (c); the right picture shows the ARPES measurement of constant energy contour (CEC) at the Fermi surface of bulk Sb(111) surface (Adapted from Ref. 26).

References

[1] C. Bai, *Scanning Tunneling Microscopy and Its Application*. (Springer, 2000).

[2] J. Bardeen, Tunnelling from a Many-Particle Point of View. *Physical Review Letters* **6**, 57 (1961).

[3] G. Binnig, H. Rohrer, Scanning tunneling microscopy. *Surface Science* **126**, 236 (1983).

[4] G. Binnig, H. Rohrer, C. Gerber, E. Weibel, Tunneling through a controllable vacuum gap. *Appl. Phys. Lett.* **40**, 178 (1982).

[5] G. Binnig, H. Rohrer, C. Gerber, E. Weibel, Surface Studies by Scanning Tunneling Microscopy. *Physical Review Letters* **49**, 57 (1982).

[6] G. Binnig, H. Rohrer, Scanning tunneling microscopy—from birth to adolescence. *Reviews of Modern Physics* **59**, 615 (1987).

[7] S. Y. Qin, J. Kim, Q. Niu, C. K. Shih, Superconductivity at the Two-Dimensional Limit. *Science* **324**, 1314 (2009).

[8] Y. Jiang *et al.*, Landau Quantization and the Thickness Limit of Topological Insulator Thin Films of Sb_2Te_3. *Physical Review Letters* **108**, 016401 (2012).

[9] L. Zhao *et al.*, Visualizing Individual Nitrogen Dopants in Monolayer Graphene. *Science* **333**, 999 (2011).

[10] K. Oura, V.G. Lifshits, A.A. Saranin, A.V. Zotov, M. Katayama, *Surface Science: An Introduction*. Germany: Springer, 2003.

[11] K. C. Pandey, New π-Bonded Chain Model for Si(111)-(2×1) Surface. *Physical Review Letters* **47**, 1913 (1981).

[12] R. M. Feenstra, W. A. Thompson, A. P. Fein, Real-space observation of π-bonded chains and surface disorder on Si(111)2×1. *Physical Review Letters* **56**, 608 (1986).

[13] R. E. Schlier, H. E. Farnsworth, Structure and Adsorption Characteristics of Clean Surfaces of Germanium and Silicon. *The Journal of Chemical Physics* **30**, 917 (1959).

[14] K. Takayanagi, Y. Tanishiro, S. Takahashi, M. Takahashi, Structure analysis of Si(111)-7 × 7 reconstructed surface by transmission electron diffraction. *Surface Science* **164**, 367 (1985).

[15] Y. L. Wang *et al.*, Tip size effect on the appearance of a STM image for complex surfaces: Theory versus experiment for Si (111) - (7×7). *Physical Review B* **70**, 073312 (2004).

[16] K. J. Wan, T. Guo, W. K. Ford, J. C. Hermanson, Initial growth of Bi films on a Si(111) substrate: Two phases of $\sqrt{3} \times \sqrt{3}$ low-energy-electron-diffraction pattern and their geometric structures. *Physical Review B* **44**, 3471 (1991).

[17] T. Kuzumaki *et al.*, Re-investigation of the Bi-induced Si(111)-() surfaces by low-energy electron diffraction. *Surface Science* **604**, 1044 (2010).

[18] N. J. Wu, A. Ignatiev, Low-energy-electron-diffraction structural determination of the graphite (0001) surface. *Physical Review B* **25**, 2983 (1982).

[19] Y. Wang, Y. Ye, K. Wu, Simultaneous observation of the triangular and honeycomb structures on highly oriented pyrolytic graphite at room temperature: An STM study. *Surface Science* **600**, 729 (2006).

[20] A. Luican, G. Li, E. Y. Andrei, Scanning tunneling microscopy and spectroscopy of graphene layers on graphite. *Solid State Communications* **149**, 1151 (2009).

[21] Y. Liu, R. E. Allen, Electronic structure of the semimetals Bi and Sb. *Physical Review B* **52**, 1566 (1995).

[22] R. I. Sharp, E. Warming, The lattice dynamics of antimony. *Journal of Physics F: Metal Physics* **1**, 570 (1971).

[23] D. Hsieh *et al.*, Observation of Unconventional Quantum Spin Textures in Topological Insulators. *Science* **323**, 919 (2009).

[24] X.-L. Qi, S.-C. Zhang, The quantum spin Hall effect and topological insulators. *Physics Today* **63**, 33 (2010).

[25] D. Hsieh *et al.*, A topological Dirac insulator in a quantum spin Hall phase. *Nature* **452**, 970 (2008).

[26] L. Fu, C. L. Kane, Topological insulators with inversion symmetry. *Physical Review B* **76**, 045302 (2007).

[27] K. K. Gomes *et al.*, Quantum Imaging of Topologically Unpaired Spin-Polarized Dirac Fermions. *arXiv:0909.0921v2* (2009).

[28] P. Roushan *et al.*, Topological surface states protected from backscattering by chiral spin texture. *Nature* **460**, 1106 (2009).

[29] J. Seo *et al.*, Transmission of topological surface states through surface barriers. *Nature* **466**, 343 (2010).

This Page Intentionally Left Blank

Chapter 3

Growth of Ultrathin Sb(111) Films

3.1 Introduction

Quite a few research groups including ours have studied Sb growth on several substrates, especially on HOPG and MoS_2.[1-5] The Sb is evaporated in the form of Sb_4 clusters.[5] The Sb island shape varying from spheres to ramified fractals could be explained in terms of the interplay of Sb_4 arriving rate at an existing island and the time it takes for the cluster and island to coalesce. In addition, Sb_4 could dissociate and transform from physisorption to chemisorption state. The diffusion and nucleation of chemisorbed Sb species could lead to 1D crystalline nanorods and 2D crystalline islands besides 3D islands,[2] as shown in Fig. 3.1(a). The energy costs to dissociate an Sb_4 into two Sb_2 and four Sb_1 are 2.4 eV and 4.8 eV,[2] respectively. These energies are much higher than the diffusion barrier (E_{diff}) of a physisorbed Sb_4 on HOPG (~60 meV),[2] so Sb_4 diffusion is highly activated and 3D island nucleation and growth are dominant at room temperature (RT), as shown in Fig 3.1(b). Increasing the substrate temperature could enhance the rate of Sb_4 dissociation and hence chemisorptions, which results in the dominant nucleation and growth of 2D and 1D crystalline structures,[2] as shown in Fig. 3.1(c).

Based on our understanding that dissociation of Sb_4 could result in 2D and 1D crystalline structures, we deliberately add a cracking part to the Sb evaporation source, and get smooth Sb(111) thin films. In the rest of this chapter, the growth of Sb on Si(111) at different substrate temperatures, including RT, elevated temperature and low

temperature, is described. Substrate temperature affects the diffusion length of the Sb atoms, and subsequently the morphology of Sb nanostructures. The Sb(111) and Sb(110) films coexist after depositing on Si(111) surface at or above RT. Post-growth annealing

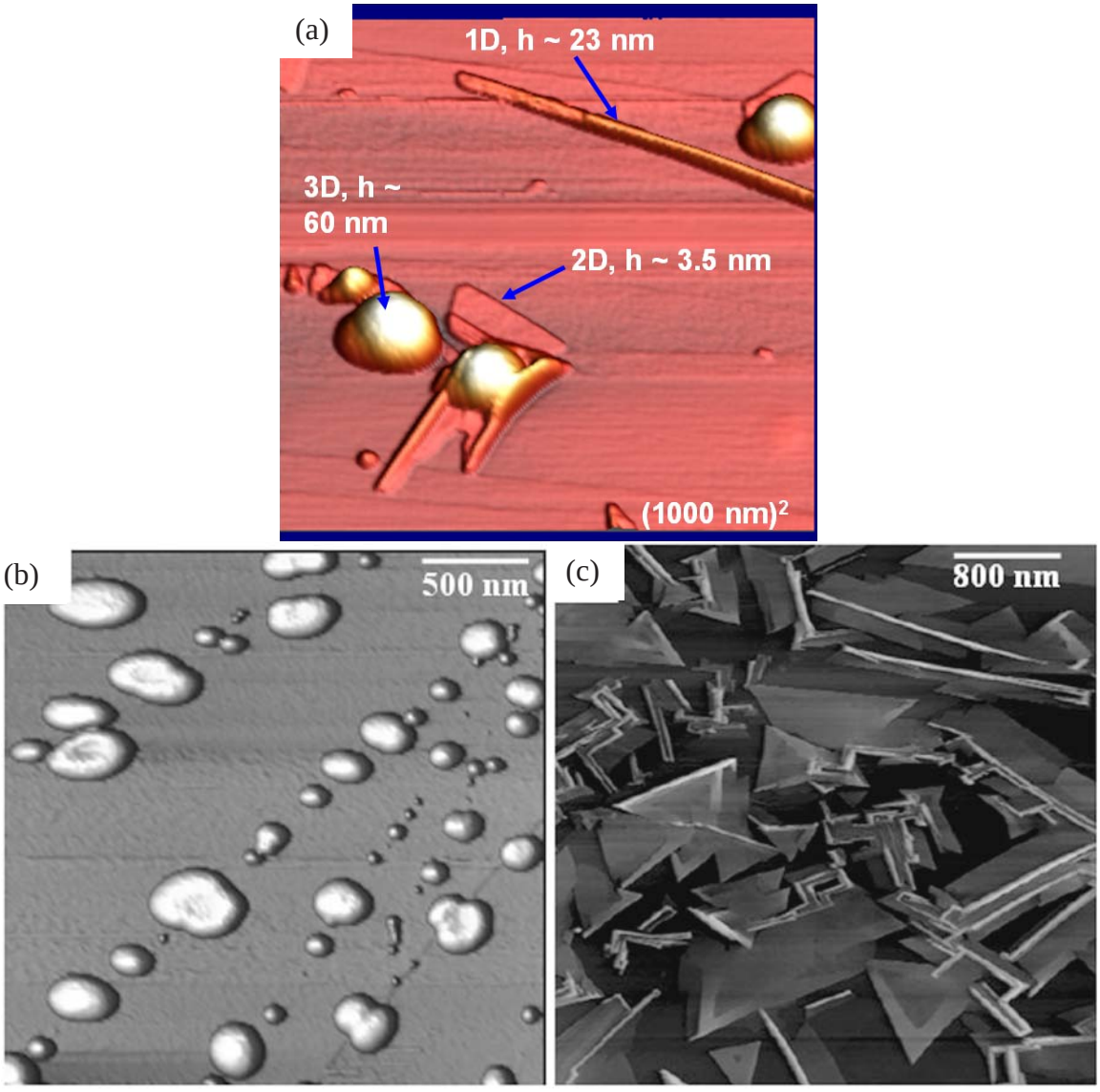

Fig. 3.1. The STM images of Sb structures on HOPG. (a) Sb deposited at RT, three different types of structures, 1D crystalline nanorods, 2D crystalline islands and 3D islands, are labeled as 1D, 2D and 3D, separately. (b) Sb deposited at RT, with 3D islands dominating. (c) Sb deposited at 100 ºC, 1D and 2D crystalline structures dominate due to the dissociation of Sb_4 at elevated substrate temperature. (Reprinted from Ref. [2] by permission of American Institute of Physics)

of the nanostructures grown at RT leads to the transformation to single crystalline Sb(111) films. First-principles calculations demonstrated that, at the same thickness, the energy of Sb(111) thin film is lower than that of Sb(110) thin film, which explains the transformation from Sb(110) to Sb(111) film after annealing. Sb(111) thin film of very good quality can be formed by depositing Sb at low temperature followed with post-growth annealing. The thinnest Sb(111) film we can get experimentally is 4 BL, probably because 4 BL is the critical thickness to be stable.

3.2 Experimental and computational methods

The studies of Sb deposition on Si(111) at RT and elevated temperature (80 ºC) are carried out in Omicron UHV RT-STM. The base pressure is 2×10^{-10} Torr. Electrochemically etched tungsten tips are used. The surface condition of Si(111) is checked with STM and LEED. High purity (99.999%) Sb source is used. The flux of Sb is 0.175 BL/min (1 BL is defined as 1 bilayer of Sb(111), *i.e.*, 12.4×10^{14} cm^{-2}). The flux is calibrated by growing flat Sb(111) thin film and measuring the film thickness.

The studies of Sb deposition on Si(111) at low temperature are performed in the Unisoku UHV LT-STM system. The base pressure is 9×10^{-11} Torr. PtIr tips are used. The surface condition of Si(111) is checked with STM. Sb is deposited on Si(111)-7×7 at about -150 °C, with flux of 0.23 BL/min, then the sample is annealed to 280 ºC and STM imaging is performed at LHe temperature (4.2 K).

The first-principles calculations of the electronic structures of Sb are carried out within the framework of density functional theory (DFT) as implemented in the Vienna

Ab-initio Simulation Package (VASP). In all calculations, the projector augmented-wave (PAW) pseudopotential,[6,7] the generalized gradient approximation (GGA) in Perdew-Burke-Ernzerhof (PBE) format[8, 9] and the spin-orbit coupling are employed. A standard plane-wave basis set with a kinetic energy cutoff of 250 eV and a Monkhorst-pack *k*-mesh[10] of 5×5×1 sampling in the full BZ are used. The vacuum region of 10 Å along the film normal direction is employed between repeated thin films.

3.3 Results and discussion

3.3.1 Sb source

As noted in Section 3.1, dissociating Sb_4 into Sb single atoms is important for forming 1D and 2D crystalline structures. One way to enhance the dissociation of Sb_4 into Sb_1 atoms is to increase the substrate temperature. However, the energy costs of dissociating one Sb_4 into two Sb_2 and four Sb_1 are 2.4 eV and 4.8 eV,[2] respectively. If one keeps the substrate temperature at 200 ºC, which can supply Sb_4 thermal energy of $k_BT \approx 40.8$ meV, the dissociation probability is still too small. Adding a cracking part to the source is more effective, as shown in Fig. 3.2(a). Using a tungsten (W) filament from backside to heat a tantalum (Ta) foil to over 1100 ºC when evaporating Sb, almost all Sb_4 clusters can dissociate into single Sb atoms before arriving at the substrate. The cracking temperature we used here is based on the research by Rouillard *et al.*.[5] They passed the evaporated Sb_4 through a cracking part, where the temperature was kept from about 500 ºC to over 1500 ºC, and recorded the flux of coming out Sb_4, Sb_2 and Sb, respectively, as shown in Fig. 3.2(b).[5] When the cracking temperature is 825 ºC, almost all the Sb_4 clusters are

cracked into Sb_2 clusters. If the temperature is over 825 ºC, Sb_2 clusters start to crack into single Sb atoms. To get majority single Sb atoms, we must set the cracking temperature at over 1100 ºC. In our experiment, single Sb atoms were detected, as shown by the mass spectrum in Fig. 3.2(c), when evaporating Sb with the W filament from backside of the Ta foil on. In the remaining part of this chapter and the next two chapters, all Sb nanostructures were grown from the cracked Sb source.

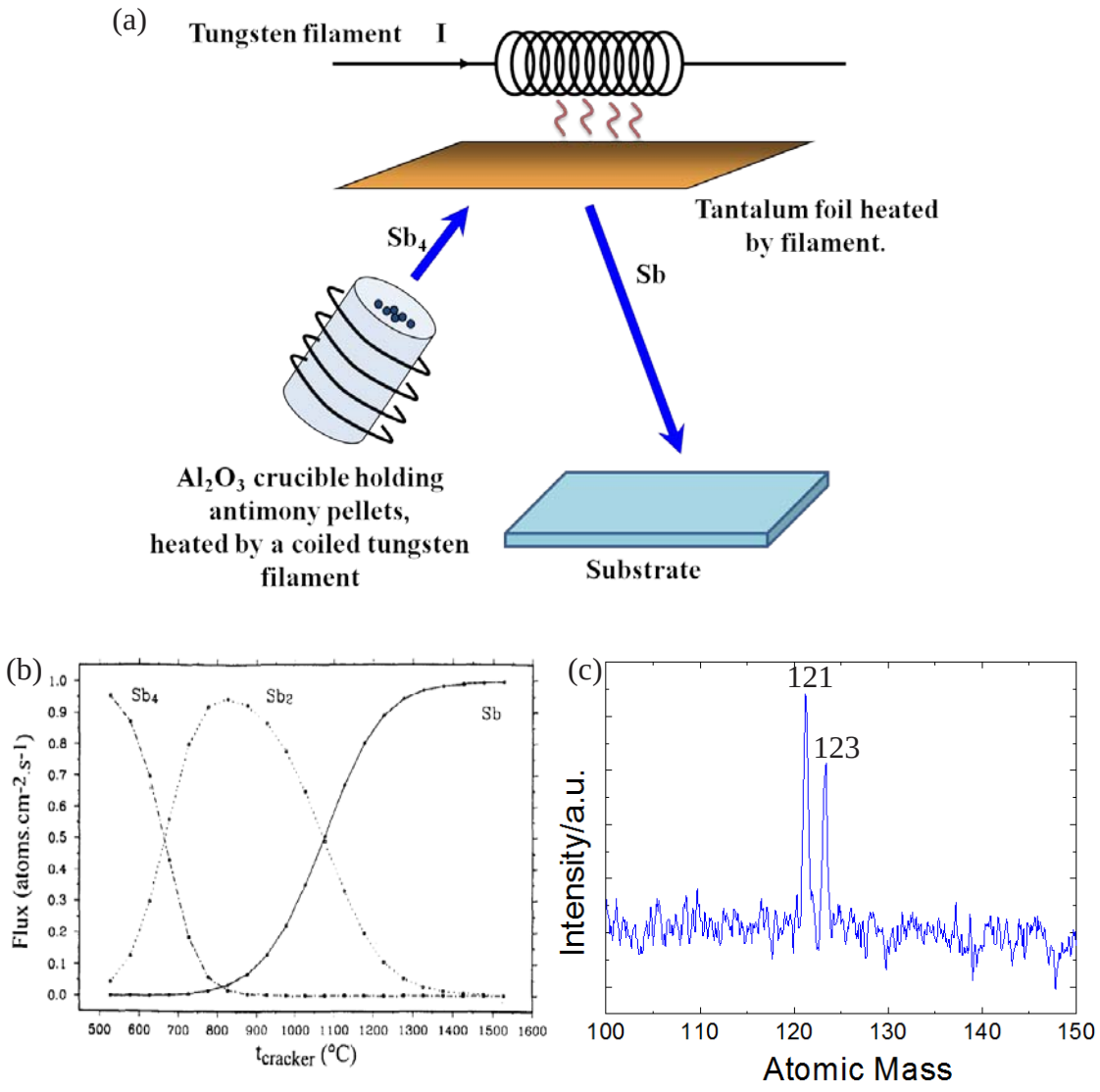

Fig. 3.2. (a) Schematic view of Sb source with a cracking part. Sb was evaporated to a Ta foil heated to over 1100 ºC by a tungsten filament from backside. The Sb_4 clusters impinged on the high-temperature Ta foil where they were cracked to single Sb atoms, then single Sb atoms were reflected to the substrate. (b) Flux of Sb_4, Sb_2 and Sb versus the temperature of the cracker zone (Reprinted from Ref. 5 by permission of Elsevier). (c) Mass spectrum of cracked Sb vapor in our experiment, which indicates the yield of single Sb atoms. ^{121}Sb and ^{123}Sb are two naturally occurring isotopes of Sb.

3.3.2 Substrate temperature effect on Sb nanostructures

Sb under 2-BL amount deposited on Si(111)-7×7 at 80 ºC forms a rough wetting layer, as shown in Fig. 3.3(a). The roughness is about 2 nm as shown from the line profile Fig. 3.3(b), which is extracted from Fig. 3.3(a) along the straight line. In each 7×7 reconstruction unit cell, there are 19 dangling bonds (see Section 2.3.1), hence the interaction between Sb and the Si substrate is strong, which makes diffusion length of Sb atoms on Si(111)-7×7 relatively short. Therefore, the aggregation of Sb atoms on Si(111)-7×7 is difficult and atoms distribute all over the surface. Furthermore, since there is a large lattice mismatch (12.2%) between Sb(111) surface and Si(111)-1×1, it is hard for the Sb to grow crystalline structure before a wetting layer is fully formed. Extra Sb adatoms on the wetting layer form thermodynamically more stable form, *i.e.*, crystalline structure, as shown in Fig. 3.3(c) and (d). These two figures are scanned after 2.6-BL Sb deposition. Fig. 3.3(c) shows an image of Sb(111) islands while Fig. 3.3(d) shows Sb(110) islands. The in-plane orientation of Sb(110) thin films is random. However, the in-plane orientation of most Sb(111) follows the substrate. The orientation alignment for Sb(111) with the substrate is even more obvious by depositing Sb at RT followed with post-growth annealing (see Fig. 3.5). Fig. 3.3(e) and (f) are images of the sample with 4.4-BL Sb deposition. No wetting layer can be seen and the substrate is fully covered by Sb(111) islands (Fig. 3.3(e)) and Sb(110) islands (Fig. 3.3(f)), which coexist with about equal probability.

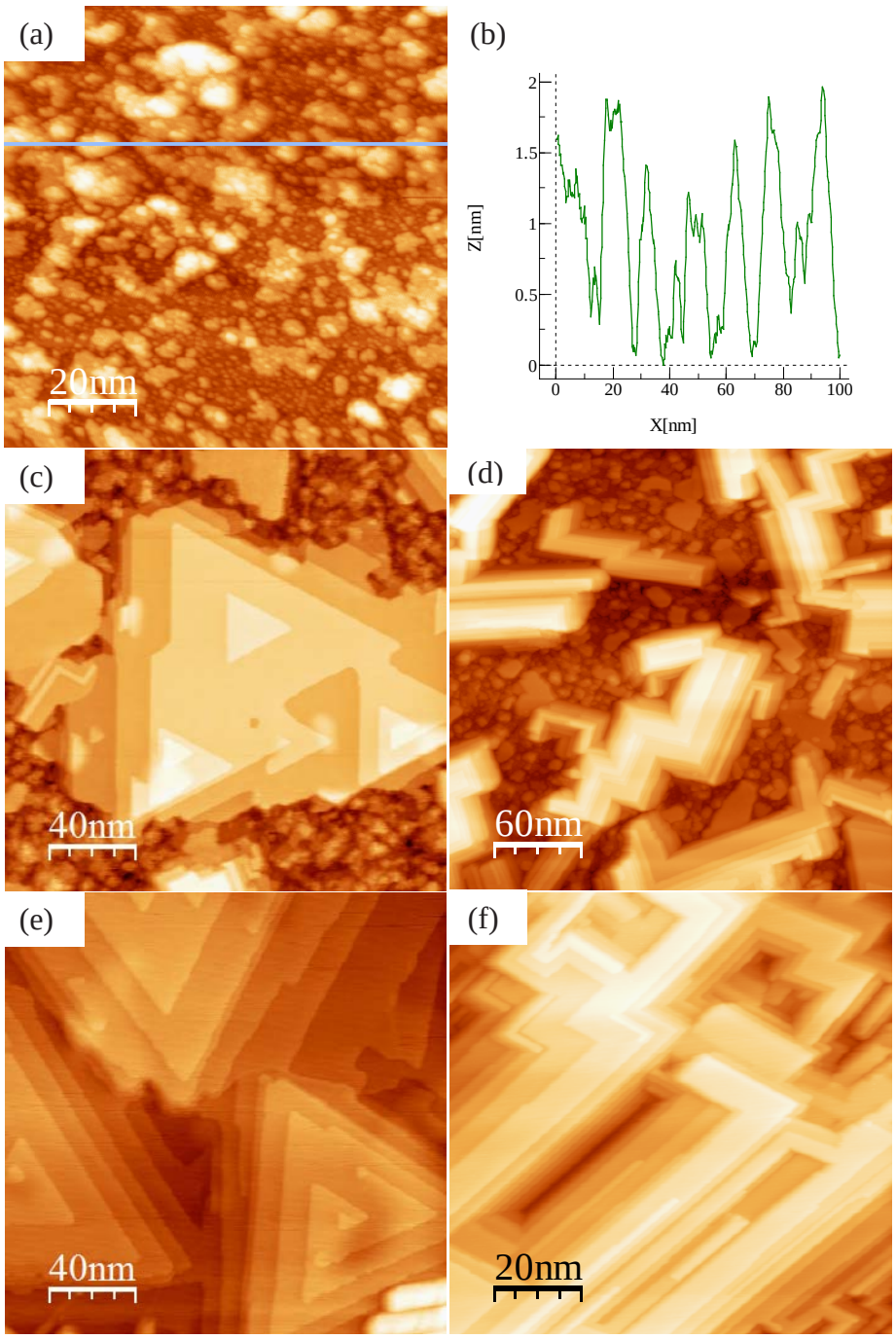

Fig. 3.3. The STM images of Sb deposited on Si(111)-7×7 at about 80 ºC. (a) The STM image of the sample with 10-min (1.75-BL) Sb deposition. (b) A line profile extracted from panel (a) along the straight line. (c), (d) The STM images of the sample with 15-min (2.6-BL) Sb deposition show the initial crystallization of (c) Sb(111) and (d) Sb(110). (e), (f) STM images of the sample with 25-min (4.4-BL) Sb deposition show that (d) Sb(111) and (e) Sb(110) nanostructure fully covered the Si(111) surface.

Next, the deposition of Sb on Si(111)-7×7 at RT will be discussed. The wetting layer is as thick as 5 BL, as shown in Fig. 3.4(a), where the total deposition amount is about 5.3 BL. The wetting layer is thicker than that formed at elevated temperature deposition where the wetting layer is about 2 BL. At RT, Sb atoms have less thermal energy to rearrange themselves into crystalline structure, so, there is just a fraction of Sb forming crystalline structure, indicated by black arrows. After more deposition of Sb (7 BL in total), as shown in Fig. 3.4(b), both Sb(111) (upper part) and Sb(110) (lower part) crystalline structures form. Compared with elevated temperature deposition, the thin film is much more flat.

Statistically, from STM images, the Sb(111) and Sb(110) have about equal probability to form on Si(111)-7×7. From upper part of Fig. 3.4(b), the Sb(111) triangular islands are of the same orientation, indicating that the Sb(111) film is single crystalline. However, the long edge direction ($\left[01\bar{1}\right]$) of Sb(110) nanobelts is random in the lower part of Fig. 3.4(b). The single-crystalline character of Sb(111) shows that the thin film orientation is regulated by the Si substrate, which is impossible if Sb(111) thin film is separated by 5-BL thick amorphous wetting layer. Therefore, we infer that, once the total amount of Sb is over 5 BL, the original amorphous wetting layer rearrange themselves into crystalline structure and there is no more wetting layer between the thin film and the substrate, as schematically shown in Fig. 3.4 (c) and (d).

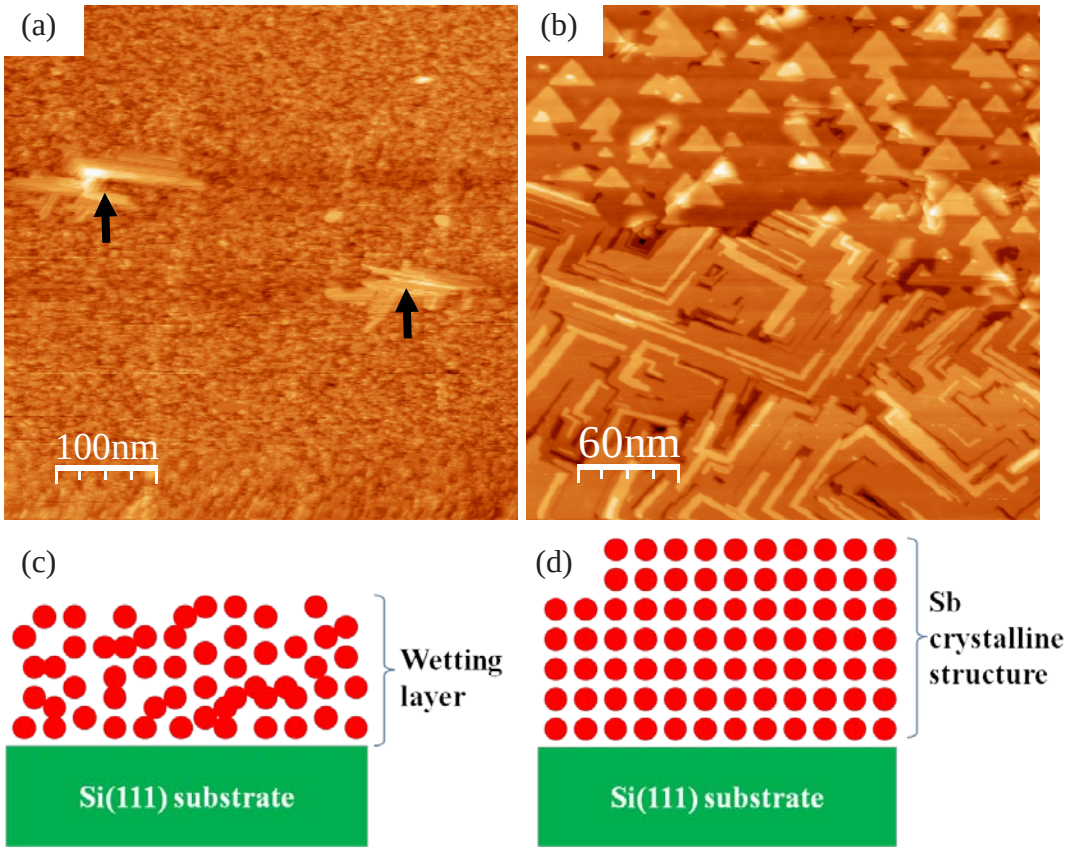

Fig. 3.4.The STM images of Sb deposited on Si(111)-7×7 at RT. (a) The STM image with 30-min (5.3-BL) Sb deposition. Two black arrows indicate the initial formation of crystalline structure. (b) The STM image with 40-min (7-BL) Sb deposition. (c) Schematic side view of wetting layer ≤ 5-BL Sb. (d) Schematic side view of crystalline structure. Once the Sb coverage is > 5 BL, crystalline structure including Sb(111) and Sb(110) form without wetting layer between the crystalline structure and the substrate.

By annealing the sample of Fig. 3.4(a) to 220 ºC for 30 min, the previous amorphous wetting layer transform to Sb(111) thin film, as shown in Fig. 3.5(a). The LEED pattern shows 6 bright spots, which are the first-order spots of Sb(111) surface, as shown in Fig. 3.5(b). To investigate whether the single crystalline follow the orientation of the substrate or not, another sample was annealed to 300 ºC for 10 min after 7-BL deposition of Sb. The annealing temperature is high enough that Sb atoms can desorb and part of Si substrate was exposed. The LEED pattern of this sample is shown in Fig. 3.5(c). Compared with Fig. 3.5(b), there emerged a new set of six bright spots with a larger reciprocal lattice vector, which we call the outer set. The ratio of the reciprocal lattice vector of the inner set to that of the outer set is about 0.9, which is the inverse of surface lattice constant of Sb(111) (4.31 Å) over that of Si(111) (3.84 Å). Therefore, the inner set is the first-order spots of Sb(111) while the outer set is that of Si(111). This LEED pattern proved that the orientation of Sb(111) is the same as that of the Si substrate. Our experiment showed that the wetting layer of thickness between 4-5 BL can be annealed to crystalline structure; below 4 BL, the wetting layer remains amorphous after annealing to 180 ºC for 30 min. By increasing the annealing time or annealing temperature, amorphous wetting layer start to desorb, *i.e.*, the thinnest Sb(111) film one is able to get by annealing amorphous wetting layer is 4 BL.

By annealing thicker Sb(111) and Sb(110) crystalline structures, we can also get single crystalline Sb(111) films over 5-BL thick. Fig. 3.5(d) is the STM image of the sample acquired by annealing the sample of Fig. 3.4(b) to 220 ºC for 30 min. After annealing, the film became more flat, and transformed to single crystalline Sb(111) film instead of coexisting of Sb(111) and Sb(110). At elevated temperature, the Sb atoms have

more thermal energy to rearrange themselves to lower the energy. This phenomenon indicates that Sb(111) uniform thin film has lower energy than Sb(110) uniform thin film at the same coverage. To validate this claim, the relative extra energy $E_e(n) = U(n)/2n - E_B$ was calculated, where $U(n)$ is the total energy of the n-layer thin film. Note that here n-layer Sb(111) indicates n BL Sb(111) and the atomic density of 1 BL Sb(111) is 12.4×10^{14} cm^{-2}; n-layer Sb(110) indicates n ML Sb(110) and the atomic density of 1 ML Sb(110) is 10.3×10^{14} cm^{-2}. There are two atoms in each layer of the unit cell. As a result, $U(n)/2n$ is the average energy of one atom in n-layer thin film. E_B is the energy of each bulk Sb atom. So extra energy $E_e(n)$ is defined as average extra energy gained by each Sb atom in n-layer thin film compared with the bulk atom. The calculation results for 1-10 BL Sb(111) and 1-12 ML Sb(110) is shown in Fig. 3.5(e). At the same coverage, the Sb(111) thin film always has lower energy. The energy reduction is about 20 meV, roughly the same as thermal energy at RT (~ 26 meV). This calculation data explains the experimental results.

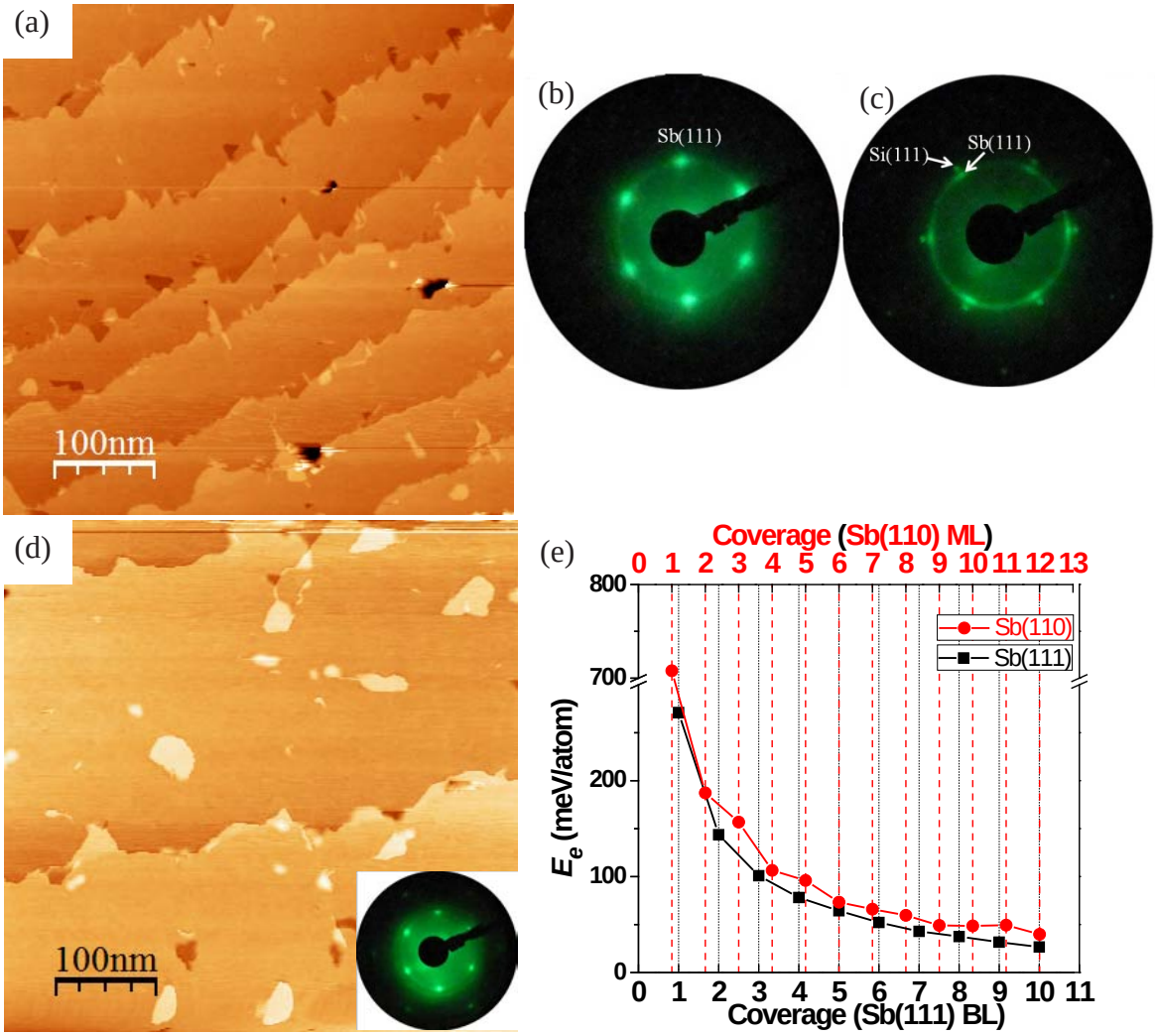

Fig. 3.5. (a) The STM image of the sample annealed to 220 ºC for 30 min after 30-min (5.3-BL) deposition of Sb at RT and (b) its LEED pattern (80 eV). (c) LEED pattern (80 eV) of the sample annealed to 300 ºC for 10 min after 7-BL deposition of Sb at RT. Si signal can be seen because part of the Si substrate was exposed due to desorption of Sb. (d) The STM image of the sample annealed to 220 ºC for 30 min after 40-min (7-BL) deposition of Sb at RT. The insert image shows the LEED pattern (76 eV) of the sample. (e) First-principles calculations of the extra energy $E_e(n)$ of Sb(111) and Sb(110) thin films. The red solid circles and black solid squares are $E_e(n)$ of Sb(110) and Sb(111) thin films, respectively. The red and black solid lines are guides to the eye. Note that since $E_e(1)$ of Sb(110) is especially large, for better view of other E_e(n), there is a break of vertical axis from 300 meV to 700 meV.

The morphology of the Sb(111) film was also influenced by the terrace width of the Si substrate. In our experiment, Si substrates of different miscut angles were used. Fig. 3.6(a) schematically illustrates the vicinal Si substrate with miscut angle of α. Suppose the steps are single atomic steps, then the average terrace width $D = h / \tan\alpha$, where h is the single atomic step height. Fig. 3.6(b) and (d) are the STM images of Si substrates with miscut angle $< 0.5°$ and $\approx 1.5°$, respectively, so the average terrace width is larger than 36 nm for (b) and approximately equals to 12 nm for (d). Fig. 3.6(c) and (e) are the 7 BL Sb(111) film on the substrate of Fig. 3.6 (b) and (d), respectively. It is obvious that Sb(111) thin film has wider terrace on Si substrate with wider terrace. The terrace widths are more or less the same as the substrate terrace widths. The thin film is globally flat regardless of the substrate terrace. The evidence is stronger if we anneal the sample to expose part of the Si substrate, so that Sb(111) terrace and Si(111) terrace can be observed in one image, as shown in Fig. 3.6(f). This sample is prepared by depositing 4.4-BL Sb at RT and annealing the sample at 250 °C for 30 min. The dark area is Si substrate, while the bright area is Sb(111) film of mainly 4 BL. The terrace of the Sb film (indicated by arrows) follows exactly the terrace of Si substrate. This globally flat film growth mode is illustrated schematically in Fig. 3.6(g). The terrace width of Sb(111) thin film can be controlled by selecting Si substrate with different miscut angles.

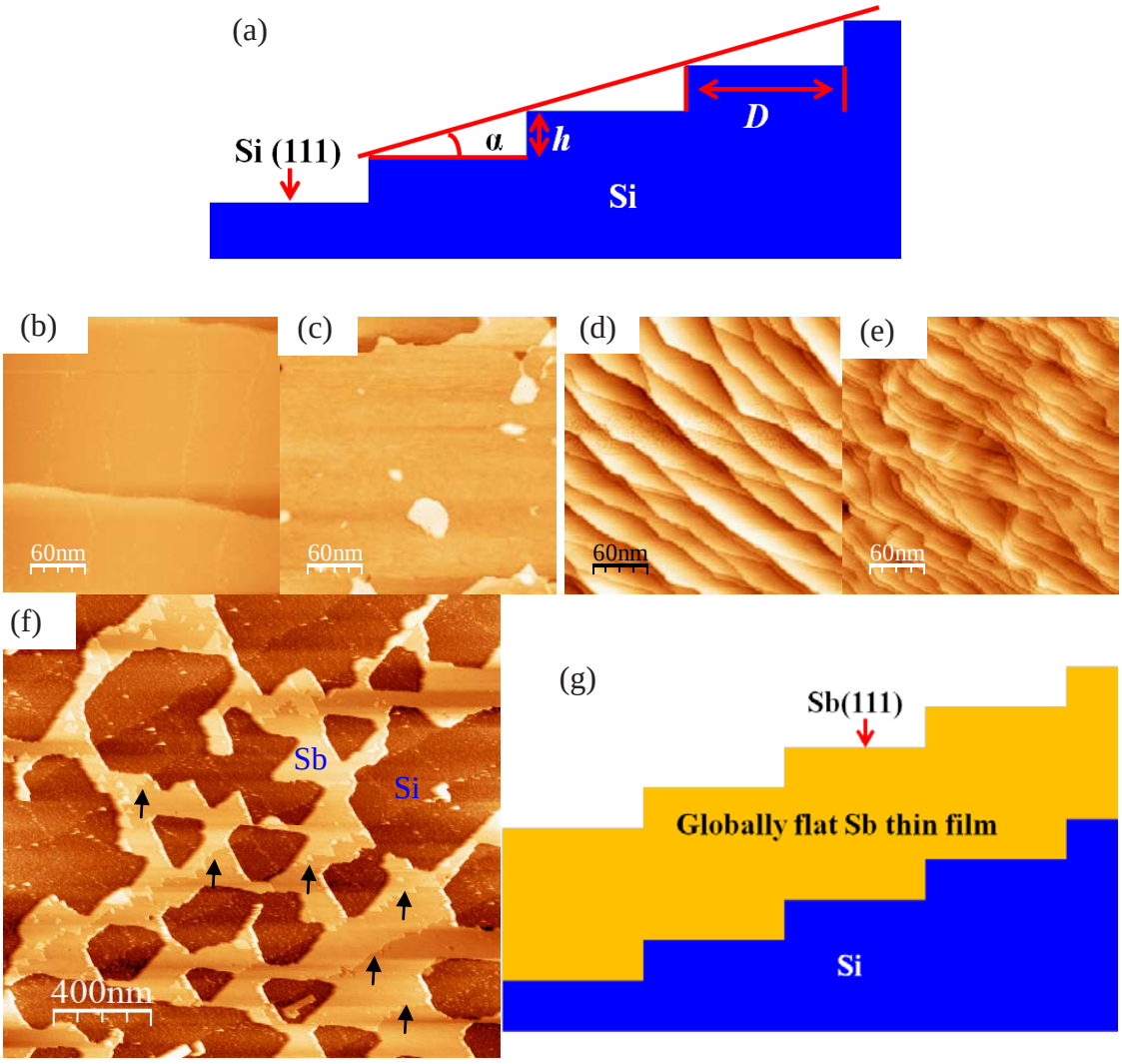

Fig. 3.6. Globally flat thin film growth mode. (a) Schematic view of Si(111) substrate with miscut angle of α; *D* is the average terrace width; *h* is the single atomic step height. (b) The STM image of Si(111)-7×7 with miscut angle < 0.5° and (c) 7 BL Sb(111) on it. (d) The STM image of Si(111)-7×7 with miscut angle ≈ 1.5° and (e) 7 BL Sb(111) on it. (f) The STM image of 4 BL Sb(111) film on Si substrate. It is obvious that the terrace of the Sb thin film (indicated by arrows) follows exactly the terrace of Si substrate. (g) Schematic view of globally flat Sb(111) thin film on Si.

By comparing the depositions of Sb at elevated temperature and at RT, it is obvious that the RT deposition could result in the uniform distribution of Sb. Post-growth annealing causes the Sb atoms to rearrange themselves into thermodynamically more stable Sb(111) thin film. Following the trend, deposition at low temperature plus post Post-growth annealing could result in uniform film of better quality. Based on this expectation, 4-BL Sb was deposited on Si(111)-7×7 at about -150 °C, with flux of 0.23 BL/min. Then the sample was annealed to 280 °C for 10 min. STM images were acquired at LHe temperature. Fig. 3.7(a) is the STM image, which shows the yield of very flat and uniform thin film. Fig. 3.7(b) is the profile along the green line in (a), which shows that the hole in the film, reaching to the Si substrate, is about 1.44 nm in depth, which is the thickness of 4 BL Sb(111). Fig. 3.7(c) is the atomic-resolution STM image. The thinnest Sb(111) film can be obtained by this method is still 4 BL. Even the thin film is annealed to 220 °C for as long as 60 min so that Sb atoms can desorb in a slow rate, the thickness of islands left on Si substrate is ≥ 4 BL, as shown in Fig. 3.7(d). Generally speaking, as the freestanding thin film get thicker, the average energy for each atom is reduced and the value approaches that of the bulk energy, as shown in the black line of Fig. 3.5(e). n-layer film is stable if the energy satisfies $E_e(n) < \left[E_e(n-1) + E_e(n-1)\right]/2$.[11] However, the presence of critical stable layer for Sb(111) (4 BL) cannot be extracted from the energy of freestanding thin film because of the substrate effect for real thin film. There is charge redistribution between the thin film and the substrate to make sure the alignment of the Fermi level at the interface. This charge spilling would reduce the total energy of the system.[12] As a result, the energy of Sb(111) thin film would differ a little bit from that in

Fig. 3.5(e). Probably the critical 4 BL could be explained by detailed calculation taking into account of the Si substrate effect.

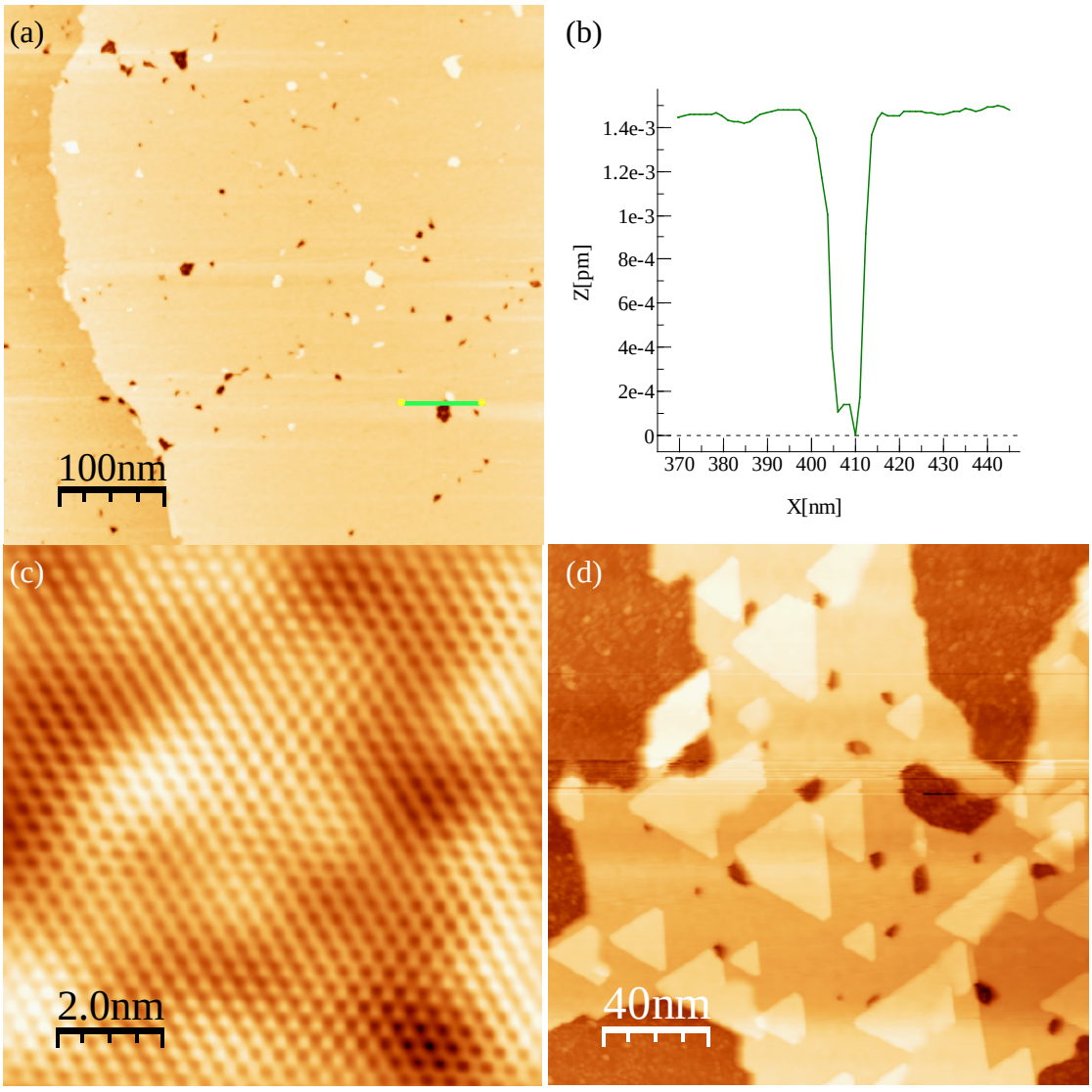

Fig. 3.7. (a) The STM image of 4 BL Sb(111) on Si(111). (b) Line profile of a hole on Sb(111) along the green line in (a) shows the hole reaches to the Si substrate. (c) The atomic-resolution STM image of 4 BL Sb(111). (d) Part of the Si substrate is exposed due to desorption of Sb at elevated temperature.

3.4 Conclusions

In this chapter, Sb thin films and nanostructures grown on Si(111)-7×7 substrate was demonstrated. Cracked Sb source provides a possibility to realize the 1D and 2D nanostructures growth mode on Si substrate, without forming high 3D islands at the same time

At 80 °C and a deposition amount ≤ 2 BL, amorphous wetting layer forms. With deposition amount > 2 BL, Sb (111) and (110) islands formed with about equal probability. At RT and a deposition amount ≤ 5 BL, the atoms form amorphous wetting layer. Above 5-BL deposition, smooth Sb(111) and (110) islands without underlying wetting layer form with about equal probability. The post-growth annealing can achieve single crystalline Sb(111) films of thickness ≥ 4 BL. Energy of a Sb(111) is always lower than that of Sb(110) at the same coverage, which explains the transformation from Sb(110) to Sb(111) film with post-growth annealing.

The good quality single crystalline Sb(111) films of thickness ≥ 4 BL can be grown at low temperature followed with post-growth annealing to about 280 °C for 10 min.

References

[1] L. Bardotti, P. Jensen, A. Hoareau, M. Treilleux, B. Cabaud, Experimental Observation of Fast Diffusion of Large Antimony Clusters on Graphite Surfaces. *Physical Review Letters* **74**, 4694 (1995).

[2] X.-S. Wang, S. S. Kushvaha, Z. Yan, W. Xiao, Self-assembly of antimony nanowires on graphite. *Applied Physics Letters* **88**, 233105 (2006).

[3] B. Kaiser, B. Stegemann, Cluster Assembled Nanostructures: Designing Interface Properties. *ChemPhysChem* **5**, 37 (2004).

[4] B. Kaiser, B. Stegemann, H. Kaukel, K. Rademann, Instabilities and pattern formation during the self-organized growth of nanoparticles on graphite. *Surface Science* **496**, L18 (2002).

[5] Y. Rouillard, B. Lambert, Y. Toudic, M. Baudet, M. Gauneau, On the use of dimeric antimony in molecular beam epitaxy. *Journal of Crystal Growth* **156**, 30 (1995).

[6] P. E. Blöchl, Projector augmented-wave method. *Physical Review B* **50**, 17953 (1994).

[7] G. Kresse, D. Joubert, From ultrasoft pseudopotentials to the projector augmented-wave method. *Physical Review B* **59**, 1758 (1999).

[8] J. P. Perdew, K. Burke, M. Ernzerhof, Generalized Gradient Approximation Made Simple. *Physical Review Letters* **77**, 3865 (1996).

[9] J. P. Perdew, K. Burke, M. Ernzerhof, Generalized Gradient Approximation Made Simple [Phys. Rev. Lett. 77, 3865 (1996)]. *Physical Review Letters* **78**, 1396 (1997).

[10] H. J. Monkhorst, J. D. Pack, Special points for Brillouin-zone integrations. *Physical Review B* **13**, 5188 (1976).

[11] M. M. Özer, Y. Jia, B. Wu, Z. Zhang, H. H. Weitering, Quantum stability and reentrant bilayer-by-bilayer growth of atomically smooth Pb films on semiconductor substrates. *Physical Review B* **72**, 113409 (2005).

[12] Z. Y. Zhang, Q. Niu, C. K. Shih, "Electronic growth" of metallic overlayers on semiconductor substrates. *Physical Review Letters* **80**, 5381 (1998).

This Page Intentionally Left Blank

Chapter 4

Inter-surface Coupling and SIA Effects on Ultrathin Sb(111)

4.1 Introduction

Sb(111) surface states of bulk single crystal have been studied by ARPES and STM.[1-6] These experiments clearly demonstrated that the surface states, which connect the bulk valence and conduction bands in a topologically non-trivial way, are spin-polarized due to SOC. However, in the field of real device applications, thin films, instead of bulk TI, are the building blocks to transport spin of electrons or to form junctions with other materials. Besides the architecture requirement for thin films, there are two more advantages. First, the surface-to-volume ratio is larger and hence the spin-polarized surface states can account for a greater proportion of total transporting electrons, increasing signal-to-noise ratio. Second, when the films are sufficiently thin to be comparable with the wavelength of the electrons, quantum confinement effect may result in larger bulk band gap. Assuming the potential of the thin film to be infinitely deep square well potential, the band gap E_g^{eff} is given by the following equation,

$$\begin{aligned} E_g^{eff} &= \min(E_e) - \max(E_h) \\ &= (E_C + \frac{\pi^2\hbar^2}{2m_0 m_e^* a^2}) - (E_V - \frac{\pi^2\hbar^2}{2m_0 m_h^* a^2}) \\ &= (E_C - E_V) + \frac{\pi^2\hbar^2}{2m_0 a^2}\left(\frac{1}{m_e^*} + \frac{1}{m_h^*}\right) \\ &= E_g^{bulk} + \frac{\pi^2\hbar^2}{2m_0 a^2}\left(\frac{1}{m_e^*} + \frac{1}{m_h^*}\right) \end{aligned} \tag{4.1}$$

where E_g^{bulk} is the bulk band gap, a is the thickness of the thin film, m_0 is electron rest mass, m_e^* and m_h^* are the effective masses of the electron and the hole in unit of m_0, respectively. E_g^{eff} is increased by $\frac{\pi^2\hbar^2}{2m_0a^2}\left(\frac{1}{m_e^*}+\frac{1}{m_h^*}\right)$ due to quantum confinement. Applying Eq. (4.1) to Sb is especially interesting, since the bulk band gap of Sb is E_g^{bulk} = -174 mV,[7] the increase of the bulk band gap can possibly turn the topological semimetal to a TI. For Sb(111) surface, m_e^* = 0.073 and m_h^* = 0.120.[7] Substituting these values into Eq. (4.1), we get the critical thickness a for the thin film to possess a positive gap to be around 6.7 nm, which is approximately 18 BL. This rough estimation gives us a clue that the transition from a topological semimetal to a TI is possible. Recently, by first-principles calculations, P. Zhang *et al.*[8] have demonstrated that the Sb(111) thin film transform from a topological semimetal to a TI at the thickness of 7.8 nm, which is approximately 22 BL.

Larger surface-to-volume ratio and quantum confinement effect give advantages in practical applications of TI thin films. However, as the film becomes as thin as comparable with the penetration depth of the surface states, coupling between the states from different surfaces due to quantum tunneling of electrons may result in a surface energy gap. The gap opening induced by this inter-surface coupling has been clearly seen by ARPES below 6 quintuple layers of Bi_2Se_3[9] and below 2 quintuple layers of Bi_2Te_3.[10] The study of inter-surface coupling provides understanding of the thickness- and *k*-dependent evolution of the Dirac cone in 3D TI.[11, 12] In addition, the surface energy gap itself in a 2D thin film may be topologically non-trival and introduces topologically

protected edge states, making the thin film a 2D TI. So far, the experimentally realized 2D TI includes HgTe quantum well,[13] InAs/GaSb quantum well[14] and 1 BL Bi(111).[15-17] In fact, the Sb(111) thin film between 4 to 8 BL is predicted to be in 2D TI state.[8] However, ARPES measurement shows that there is no surface energy gap, even at the experimentally achieved thinnest 4 BL Sb(111).[18] The difference between the calculation[8] and experiment[18] is induced by the substrate of the thin film, or space inversion asymmetry (SIA). The calculation work is based on the freestanding thin film while experimentally the thin film is attached to a substrate. Interfacial interaction between the lower surface and the substrate lifted the degeneracy of the states on two surfaces in *k*-space, thus reducing the quantum tunneling of electrons between two surfaces.

Non-spin resolved ARPES could give us an intuitive picture about the band gap and the energy dispersion, but cannot give us detailed spin textures of the surface states, which can be partially extracted from the quasiparticle interference (QPI) patterns of the surface. So the employment of FT-STS on Sb(111) thin film can give us such information about the TSS.

In the rest of this chapter, first, the results of our *in-situ* STM/STS investigations of 30 BL and 9 BL Sb(111) films on Si(111)-$\sqrt{3}\times\sqrt{3}$:Bi are presented. First-principles calculations are performed to study the electronic structures of the freestanding 30 BL and 9 BL Sb(111) films. The QPI patterns on 30 BL can be interpreted by the scattering of TSS from the top surface only. On 9 BL Sb(111), QPI pattern is quite different from that on 30 BL, and the interpretation of the pattern should consider the coupling of the states from two surfaces (inter-surface coupling). Then, QPI patterns on 4 BL Sb(111) are

presented. Since APRES measurement showed that there is no surface energy gap[18] due to SIA, we replace an Sb atom at the bottom surface by a Bi atom in each unit cell to simulate the SIA effect by first-principle calculations. The calculations showed that the surface states near the surface Brillouin zone (SBZ) centre are still spin-polarized even in 4 BL Sb(111), but exhibiting Rashba-type splitting, due to the combining effects of inter-surface coupling and SIA. The calculated real-space distributions of the surface states are in agreement with the effective continuous model[19] calculation result. With both spin and spatial distribution information, the FT-STS is simulated, which is in good agreement with the experimental results. Finally, to find out the SIA and inter-surface coupling effect on thicker films, the calculation results of 5 BL Sb(111) are demonstrated.

4.2 Experimental and computational methods

The experiments are carried out in a Unisoku UHV LT-STM system. All the STM measurements are performed at LN_2 temperature. The base pressure is 9×10^{-11} Torr. High purity (99.999%) Bi and Sb are used. Before the deposition, both sources are degassed at appropriate temperatures for 30 min in order to remove contamination. Si(111)-$\sqrt{3}\times\sqrt{3}$:Bi serves as the growth substrate, which is obtained by depositing 2 ML Bi on Si(111)-7×7 at RT, with post-growth annealing at 450 ºC for 15 min. The surface conditions of Si(111) and Si(111)-$\sqrt{3}\times\sqrt{3}$:Bi are checked with STM. Sb is deposited on Si(111)-$\sqrt{3}\times\sqrt{3}$:Bi at about -100 °C, with flux of 0.3 BL/min, then the sample is annealed to 280 ºC for 15 min. The flux is calibrated by growing flat Sb(111) thin film and measuring the film thickness. The STS data are acquired using a lock-in amplifier with

the bias voltage modulated at a frequency of 700 Hz and peak-to-peak amplitude of 10 mV.

The first-principles calculations of the electronic structures of Sb are carried out within the framework of density functional theory (DFT) as implemented in the Vienna *Ab-initio* Simulation Package (VASP). In all calculations, the projector augmented-wave (PAW) pseudopotential,[20, 21] the generalized gradient approximation (GGA) in Perdew-Burke-Ernzerhof (PBE) format[22, 23] and the spin-orbit coupling are employed. A standard plane-wave basis set with a kinetic energy cutoff of 250 eV and a Monkhorst-pack *k*-mesh[24] of 7×7×1 sampling in the full BZ are used. The vacuum region of 10 Å along the [111] direction is employed between repeated thin films. Luo Ziyu in our group performed the calculations in Section 4.3.1. All other calculations are done by the author of this thesis.

4.3 Results and discussion

The QPI patterns are measured on Sb(111) film surfaces of several different thicknesses. We take 30 BL, 9 BL and 4 BL as three typical samples to demonstrate the evolution of the surface states as the film thickness changes. Before discussing the results, the process of getting FT-STS will be explained briefly, taking the FT-STS on 4 BL sample as an example.

Fig. 4.1(a) is the STM image of the 4 BL Sb(111) film. The main part is 4 BL, with some holes reaching the substrate, and some 1-BL islands on the 4-BL film. The thinnest Sb(111) film on Si(111)-$\sqrt{3}\times\sqrt{3}$:Bi is still 4 BL, just the same as the Sb(111) growth on

Si(111)-7×7. Fig. 4.1(b) is the atomic-resolution STM image scanned over the 4-BL part. Fig. 4.1(c) is the STS map at sample bias V_s = -80 mV. Unlike Fig. 4.1(b), which is a morphology map showing mainly the height of atoms, Fig. 4.1(c) is a measure of electronic states around E = -80 meV, which is inhomogeneous. The surface states can be scattered by defects such as steps or atomic impurities. The spatially inhomogeneous electronic states on the surface arise from the interference of reflected electronic waves with the initial incoming waves. Therefore, this kind of image is also named quasiparticle interference (QPI) pattern. As discussed in Chapter 2, the periodicity of the QPI pattern along the direction of $\boldsymbol{q}$ is $|2\pi/\boldsymbol{q}|$, where $\boldsymbol{q} = \boldsymbol{k_f} - \boldsymbol{k_i}$ is the scatting wavevector ($\boldsymbol{k_f}$ and $\boldsymbol{k_i}$ are the final reflected wavevector and initial incoming wavevector). By performing a Fourier transformation of the QPI pattern, we get the Fourier transform of QPI, also named FT-STS. The Fourier transform of 4.1(c) is shown in Fig. 4.1(d). In this image, blue indicates the background, while white indicates the strongest signal. The signal spots indicate scattering wavevectors $\boldsymbol{q}$. The first SBZ is shown as a dash-line hexagon. The direction of the SBZ could be determined from the atomic-resolution image in Fig. 4.1(b), since the close packed direction in real space is the same as the $\bar{\Gamma}$-$\bar{\mathrm{K}}$ direction in *k*-space.

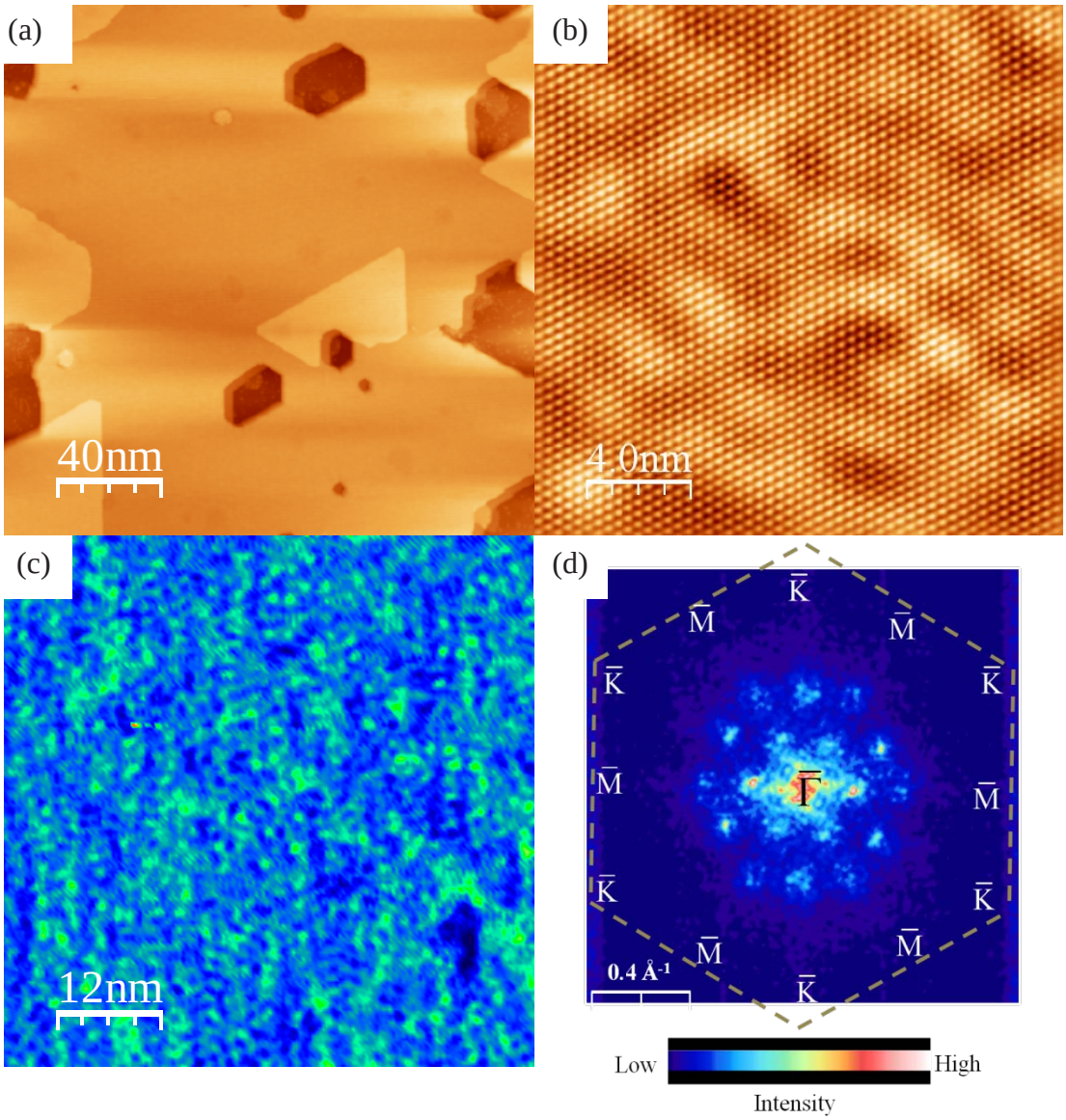

Fig. 4.1. (a) The STM image with 14-min (4.2-BL) Sb deposition on Si(111)-√3×√3:Bi at about -100 °C with post-growth annealing. The main part of the film is 4 BL, with some 1-BL islands on it and holes reaching the substrate. (b) The atomic-resolution STM image of 4 BL Sb(111). (c) The STS map at -80 mV on 4 BL Sb(111) shows QPI pattern; size is 60 nm × 60 nm. (d) The Fourier transform of the QPI pattern from panel (c), or FT-STS of panel (c); the strong intensity spots are indications of scattering wavevectors $\boldsymbol{q}$.

4.3.1 Results of 30 BL and 9 BL Sb(111) thin films

Fig. 4.2(a)[11] shows the Fourier transform of QPI pattern at V_s = 20 mV on 30 BL Sb(111). The intensity is strong along $\bar{\Gamma}$-$\bar{M}$ direction and weak along $\bar{\Gamma}$-$\bar{K}$ direction. Three key scattering wavevectors are identified as $\mathbf{q_A}$, $\mathbf{q_B}$ and $\mathbf{q_C}$. Fig. 4.2(b) is the schematic calculated constant energy contour (CEC) near $\bar{\Gamma}$ on 30 BL Sb(111) as well as the spin textures. This CEC on 30 BL is more or less the same as measured CEC on bulk Sb(111)[3] (see Fig. 2.11(d)), from which one can identify the origins of $\mathbf{q_A}$, $\mathbf{q_B}$ and $\mathbf{q_C}$ observed experimentally in Fig. 4.2(a). $\mathbf{q_A}$ corresponds to the scattering between adjacent hole pockets. $\mathbf{q_B}$ corresponds to the scattering between the hole pocket and electron pocket across the $\bar{\Gamma}$ point. $\mathbf{q_C}$ corresponds to the scattering between the next nearest hole pockets. The intensity of these scattering wavevectors in descending order is $\mathbf{q_B}$, $\mathbf{q_A}$ and $\mathbf{q_C}$, because the scattering probability is related with the spin angle difference of the two relevant states. Specifically, the scattering probability between two spin-polarized sates with wavevectors ***k***' and ***k***' is proportional to $\left|\left\langle \mathbf{S}_{k'} \middle| \mathbf{S}_{k} \right\rangle\right|^2 = \cos^2\left[(\theta_{k'} - \theta_{k})/2\right]$,[3, 25] where $\mathbf{S}_k$ and $\mathbf{S}_{k'}$ are the spin vectors of the states ***k*** and ***k***'. $\left|\left\langle \mathbf{S}_{k'} \middle| \mathbf{S}_{k} \right\rangle\right|^2$ decreases from 1 to 0 as the spin angle difference $\theta_{k'} - \theta_k$ varies from 0° to 180°. The $\mathbf{q_B}$, $\mathbf{q_A}$ and $\mathbf{q_C}$ scatterings have spin angle differences of 0°, 60° and 120°, respectively, so the corresponding scattering intensity is in descending order. The $\mathbf{q_D}$ in Fig. 4.2(b) is totally forbidden due to the requirement of spin flip, which is impossible in a TRS system (no external magnetic field and no magnetic impurities).

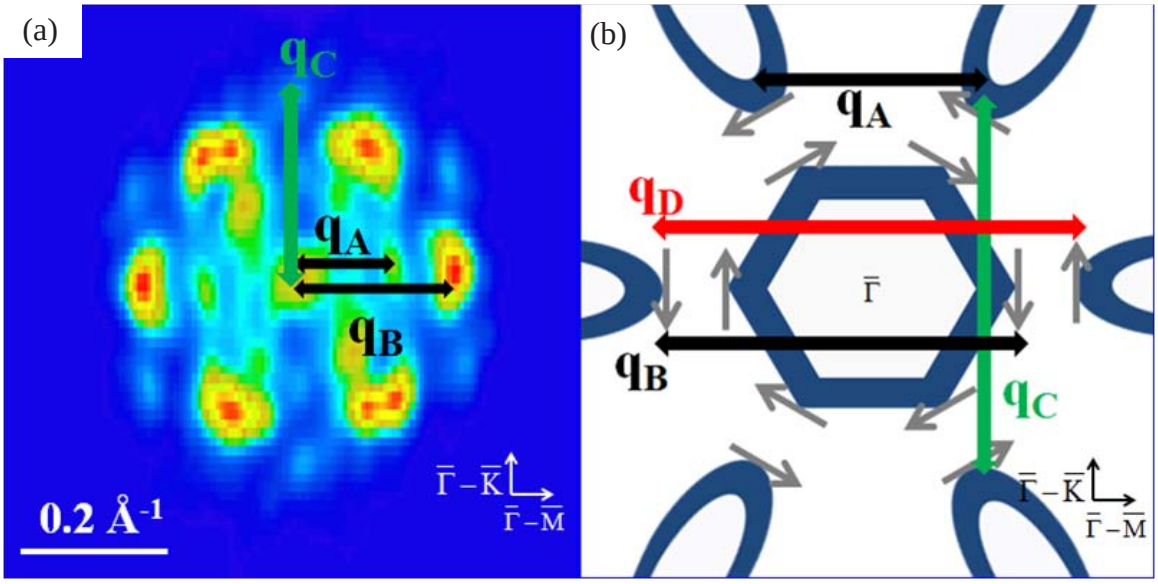

Fig. 4.2. (a) The FT-STS at V_s = 20 mV on 30 BL Sb(111). (b) Schematic calculated CEC on freestanding 30 BL Sb(111) near $\bar{\Gamma}$ at the Fermi surface. The grey arrows indicate the spin textures of the TSS. (Reprinted from Ref. 11).

Fig 4.3(a) shows the experimental result of Fourier transform of QPI at V_s = 20 mV on 9 BL Sb(111). Compared with the Fourier transform of QPI on 30 BL Sb(111), there are two principal differences. First, the intensity is strong both in $\bar{\Gamma}$-$\bar{M}$ and $\bar{\Gamma}$-$\bar{K}$ directions. Second, the cutoff scattering wavevectors are much larger than that on 30 BL Sb(111) (note that the scales are different in Fig. 4.3(a) and Fig. 4.2(a)). Two larger scattering wavevectors are labeled as $\mathbf{q_E}$ and $\mathbf{q_F}$. To investigate their origins, the schematic calculated CEC on 9 BL Sb(111) are shown in Fig. 4.3(b). The grey arrows indicate the spin textures of TSS on top surface of thick film ('thick' means that the film is thick so that there is no inter-surface coupling). The strong intensity forming a hexagon in Fig. 4.3 (a) corresponds to $\mathbf{q_A}$, $\mathbf{q_B}$ and $\mathbf{q_C}$ scatterings as observed on 30 BL Sb(111). The cutoff of the larger $\mathbf{q_E}$ and $\mathbf{q_F}$ involve the scatterings between outer edge (further away from the $\bar{\Gamma}$ point) of the six hole pockets. $\mathbf{q_E}$ scattering should be totally forbidden

on thick film since opposite spin direction of the two relevant states. However, the thickness of 9 ML Sb(111) is comparable with the penetration depth of the surface states. The spin-polarized surface states may become partly degenerate due to inter-surface coupling and $\mathbf{q_E}$ scattering is possible.

To study the coupling quantitatively, following the procedure described by Bian *et al*,[18, 26] we calculated the spin separation (Fig. 4.3(d)) of the lower surface band, indicated by blue line in Fig. 4.3(c). The calculated result showed that the surface states are spin-polarized at $\bar{\Gamma}$ point. However, from $\bar{\Gamma}$ to $\bar{M}$, the surface states gradually become unpolarized. From about 0.4 $Å^{-1}$ above, the initial polarized surface states in thick film become totally degenerate. The spin polarization is *k*-dependent because the penetration depth is longer near $\bar{M}$, where the surface states merge into the bulk. Away from $\bar{M}$, the penetration depth is shorter, as shown in Fig. 4.3(e), which is the real-space charge density distribution along the surface normal direction for the lower surface band at selected *k* points along $\bar{\Gamma}$-$\bar{M}$. Near $\bar{\Gamma}$, the states are localized on the surface; away from $\bar{\Gamma}$, the initial surface states on thick film become surface resonant states. This trend for penetration depth is also valid for the edge states in ultrathin Bi films: penetration depth is shorter when the edge states are far away from the points where edge states merge into the bulk.[27] Very recently, M. Neupane *et al.*[12] also discovered that the spin polarization of 'surface bands' in ultrathin Bi_2Se_3 films is *k*-dependent.

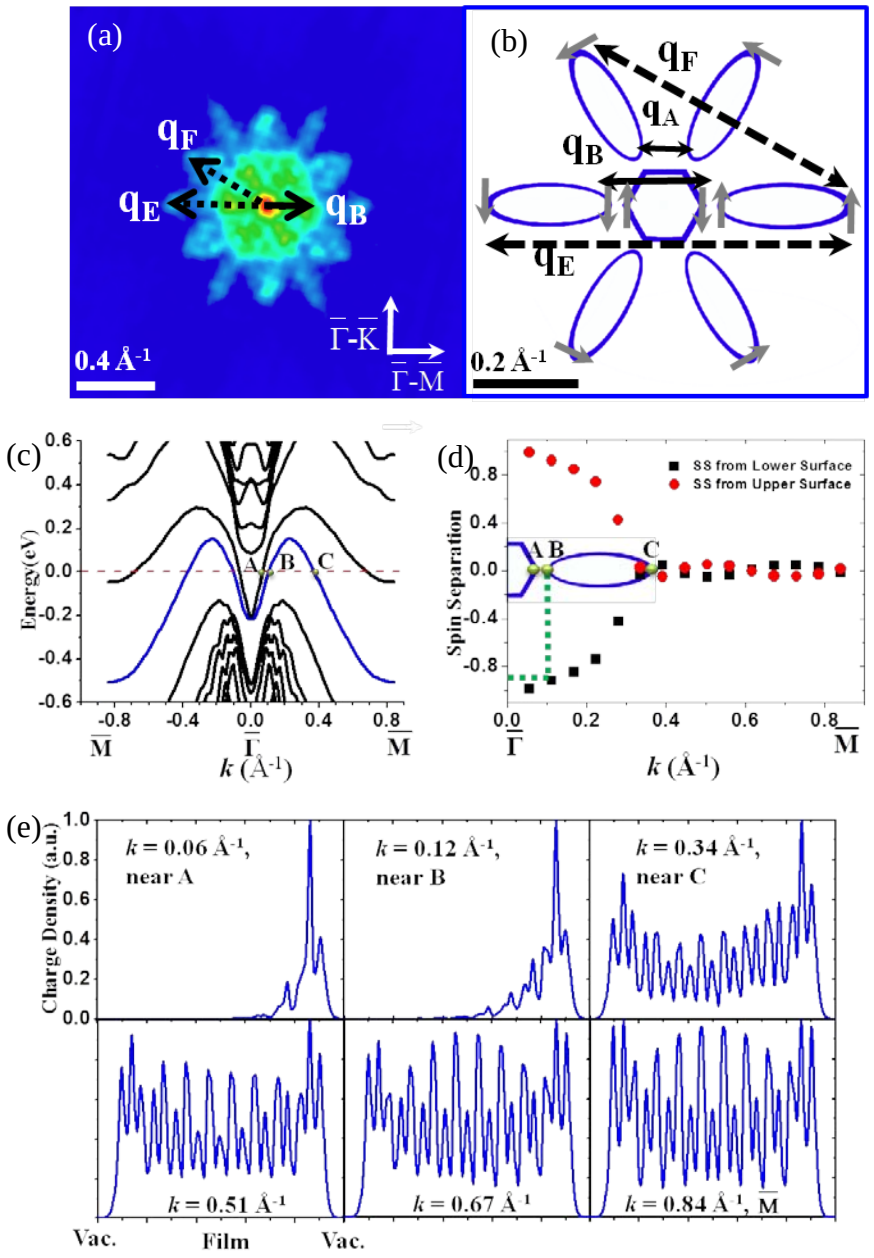

Fig. 4.3 (a) The FT-STS at 20 mV on 9 BL Sb(111). (b) Schematic calculated CEC on freestanding 9 BL Sb(111) near $\bar{\Gamma}$ at the Fermi surface. The grey arrows indicate the spin textures of the TSS on thick film. (c) Calculated band structure of freestanding 9 BL Sb(111) along $\bar{M}$-$\bar{\Gamma}$-$\bar{M}$ direction. The blue solid line indicates the lower surface band. (d) Red circles and black squares are spin separation of surface states indicated by the blue solid line in panel (c). A, B and C are the intersection points of CEC at Fermi level along $\bar{\Gamma}$-$\bar{M}$ direction. (e) Calculated real-space charge density distribution along surface normal direction at selected *k* points of the lower surface band as indicated by the blue line in panel (c). States are well localized on the surface near $\bar{\Gamma}$, away from which point the penetration depth is longer. (Adapted from Ref. 11)

4.3.2 Results of 4 BL Sb(111) thin film

From the last section, we know that the surface states on 30 BL Sb(111) are TSS affected little by inter-surface coupling, and the scatterings are significantly reduced due to the spin-polarized TSS. On 9 BL, the surface states near $\bar{M}$ are affected strongly by inter-surface coupling due to longer penetration depth and become surface resonant states, while the states near $\bar{\Gamma}$ remain spin-polarized TSS. What will happen if the film becomes even thinner? From first-principles calculations[8] and also intuitive thinking, one would believe that an energy gap will open at the Dirac point, when the film thickness is comparable with the penetration depth of surface states at $\bar{\Gamma}$. However, ARPES measurement shows that there is no surface energy gap even at the experimentally thinnest achievable 4 BL Sb(111).[18] This inconsistency between the experiment and calculation arises from the fact that real thin film are attached to the substrate while the calculation work is for freestanding thin film, *i.e.*, the SIA effect must be taken into account for 4 BL Sb(111). In the following, we show the Fourier transform of QPI on 4 BL Sb(111) first, then study the energy dispersion of the surface states near $\bar{\Gamma}$ with SIA introduced in DFT calculations. At the end of this chapter, we will show that the SIA effect is weakened on thick Sb(111). This is why for 30 BL and 9 BL Sb(111), the experimental results can be well interpreted by calculating freestanding Sb(111) thin film.

Fig. 4.4 shows a series of the FT-STS with V_s ranging from -240 mV to 20 mV. All the images are obtained from the same area as shown in Fig. 4.1(c). The FT-STS are determined by the CEC, including the shape and the spin textures, at the energy determined by V_s. The variation of CEC with energy causes the variation of the FT-STS

with V_s. At -240 mV, there is no strong spot but just some weak signal within about 0.6 $Å^{-1}$, forming a dim circle. This trend continues to -160 mV. At -120 mV, the pattern is in hexagonal shape, formed by 12 dim spots that can be barely identified. The 12 spots becomes clear from -80 mV to -40 mV, indicated in Fig. 4.2(e) as scattering wavevectors $\mathbf{q_E}$ and $\mathbf{q_F}$ along $\bar{\Gamma}$-$\bar{M}$ and $\bar{\Gamma}$-$\bar{K}$, respectively. The scattering wavevector $\mathbf{q_F}$ along $\bar{\Gamma}$-$\bar{K}$ is about $\sqrt{3}/2$ times longer in length than $\mathbf{q_E}$ along $\bar{\Gamma}$-$\bar{M}$, hence the 12 spots forming a hexagon. Besides the 12 $\mathbf{q_E}$ and $\mathbf{q_F}$ wavevectors, there are 6 short scattering wavevectors along $\bar{\Gamma}$-$\bar{M}$, indicated by $\mathbf{q_B}$. At -20 mV and 20 mV, no obvious scattering wavevector can be identified.

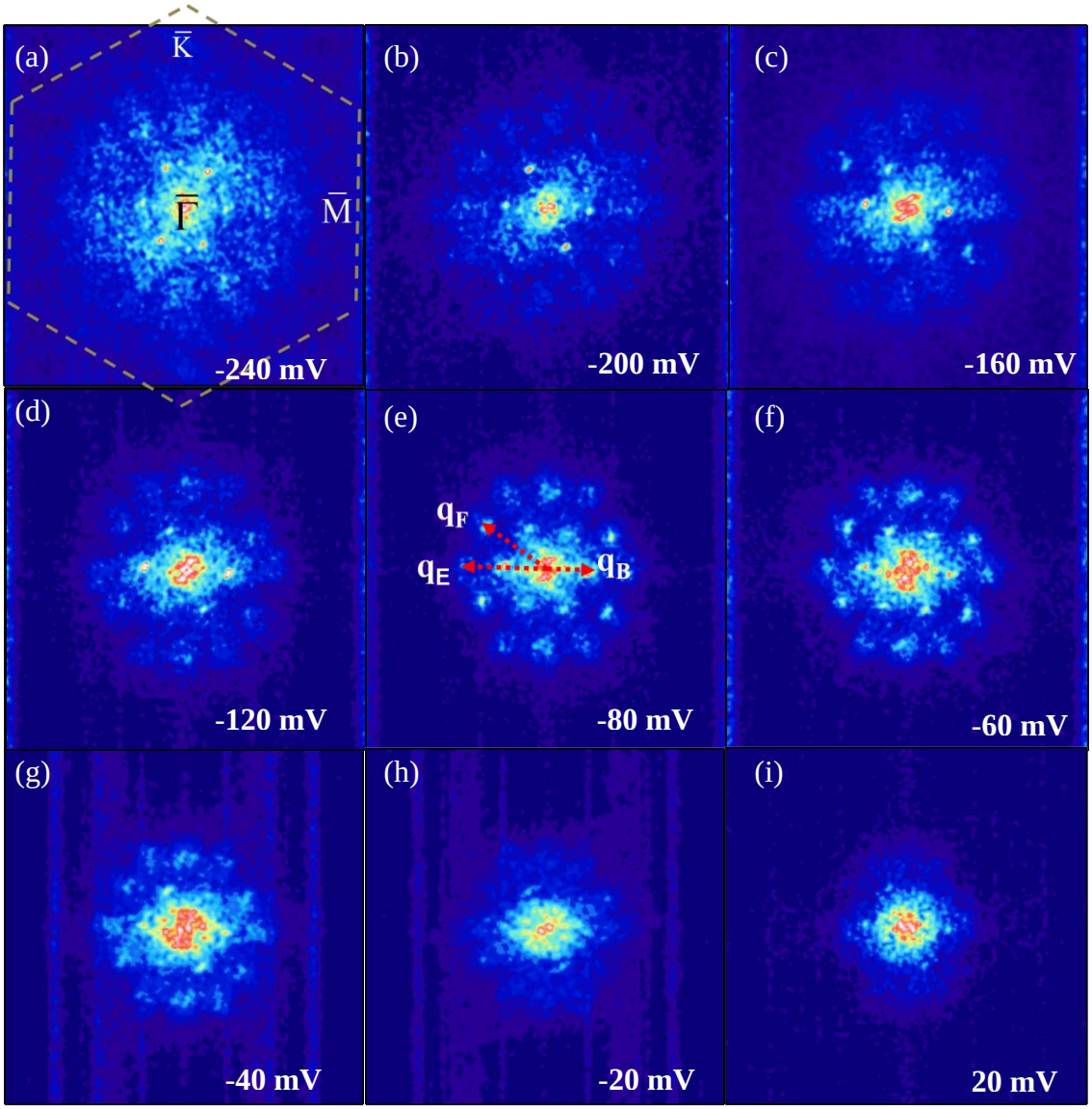

Fig. 4.4. The FT-STS from -240 mV to 20 mV on 4 BL Sb(111) surface. The scanning size of the STS map is 60 nm × 60 nm. (a) The SBZ is shown as a hexagon. The high symmetry points $\bar{\Gamma}$, $\bar{M}$ and $\bar{K}$ are indicated. (e) Six short and long scattering wavevectors along $\bar{\Gamma}$-$\bar{M}$ direction are defined as $\mathbf{q_B}$ and $\mathbf{q_E}$, respectively. Six scattering wavevectors along $\bar{\Gamma}$-$\bar{K}$ are defined as $\mathbf{q_F}$. The cutoff value of $\mathbf{q_B}$, $\mathbf{q_F}$ and $\mathbf{q_E}$ are 0.26 $Å^{-1}$, 0.44 $Å^{-1}$ and 0.5 $Å^{-1}$, respectively.

To understand the origins of these scattering wavevectors, the band structure of the 4 BL Sb(111) film should be calculated. The surface lattice constants of Sb(111) and Si(111)-$\sqrt{3}\times\sqrt{3}$:Bi are 4.31 Å and 6.65 Å, respectively. Accurate calculation including the substrate is not feasible. To simulate the SIA effect, one Sb atom (the lowest one) at the bottom surface of the 4 BL Sb(111) unit cell was replaced by one Bi atom. We call this structure Bi-Sb terminated Sb(111) hereafter. There are two justifications to select the Bi atom to replace one Sb atom. First, the Si(111)-$\sqrt{3}\times\sqrt{3}$:Bi is terminated by Bi. Second, Bi and Sb are the same-group elements, sharing the same outer electronic structure. Hence, there is no electron imbalance. The calculated Bi-Sb terminated 4 BL Sb(111) band structure along $\bar{M}$-$\bar{\Gamma}$-$\bar{K}$ is shown in Fig. 4.5(a). The band structures featuring the surface states near the SBZ centre are shown more clearly in Fig. 4.6. The band structure of freestanding 4 BL Sb(111) along $\bar{M}$-$\bar{\Gamma}$-$\bar{K}$ is shown in Fig. 4.5(b) for comparison. In Fig. 4.5(b), the red lines indicate the initial surface bands on thick film. Both lower and upper 'surface bands' in Fig. 4.5(b) represent a pair of bands with spin 'up' and 'down'. In thick film, the spin 'up' and spin 'down' bands from each pair locate on different surfaces, resulting in the spin-polarized TSS in real space. Compared with the freestanding 4 BL Sb(111) film band structure in Fig. 4.5(b), the energy dispersion of the Bi-Sb terminated film is more or less the same, except the lifted degeneracy in *k*-space for each pair of bands because of SIA. Specifically, the lower 'surface band' splits into two bands: band 39 and band 40. Note that in the calculation, the bands are classified by energy, *i.e.*, the state with lower energy at each *k* point is classified as band 39, the state with higher energy is classified as band 40. The upper 'surface band' splits into two bands: band 41 and band 42. At TRIM points ($\bar{\Gamma}$ and $\bar{M}$), the pair of band 39 and 40 keep

degenerate, the same is true for the pair of band 41 and 42. The real-space charge distributions along the surface normal direction for these states at $\bar{\Gamma}$ and $\bar{M}$ are shown in Fig. 4.5(c) and (d). The corresponding positions of the films are indicated by the side view on top. The purple circles represent Sb atoms, while the brown circle represents the Bi atom. 'B39+B40 at $\bar{M}$' indicates the real-space charge distribution of the pair of band 39 and 40 at $\bar{M}$, etc. Note that each of the eight profiles is from a degenerate point and the charge distribution is a combination of spin 'up' and spin 'down' states. Even though upper and lower 'surface bands' evolve from the surface states that reside only on surfaces of thick Sb(111) film, here the charge distribution profiles at $\bar{M}$ resemble that of surface resonant states for freestanding 4 BL Sb(111) film (Fig. 4.5(d)). States at $\bar{\Gamma}$ still reside on two surfaces. For symmetry reason of freestanding 4 BL Sb (111), the real-space charge distribution of spin 'up' and spin 'down' states from a pair of degenerate bands should be symmetric with respect to the middle of the film. This is why the charge distributions show mirror symmetry in Fig. 4.5(d). However, this is not the case for the Bi-Sb terminated 4 BL Sb(111) in Fig. 4.5(c). The charge distributions at $\bar{M}$ still resemble that of surface resonant states and are nearly mirror symmetric. The loss of symmetric distribution is more obvious at $\bar{\Gamma}$, where each pair of the states resides on one surface only. States of band 39 and 40 at $\bar{\Gamma}$ reside mainly on the lower Bi-terminated surface, and states of band 41 and 42 at $\bar{\Gamma}$ reside mainly on the upper Sb-terminated surface.

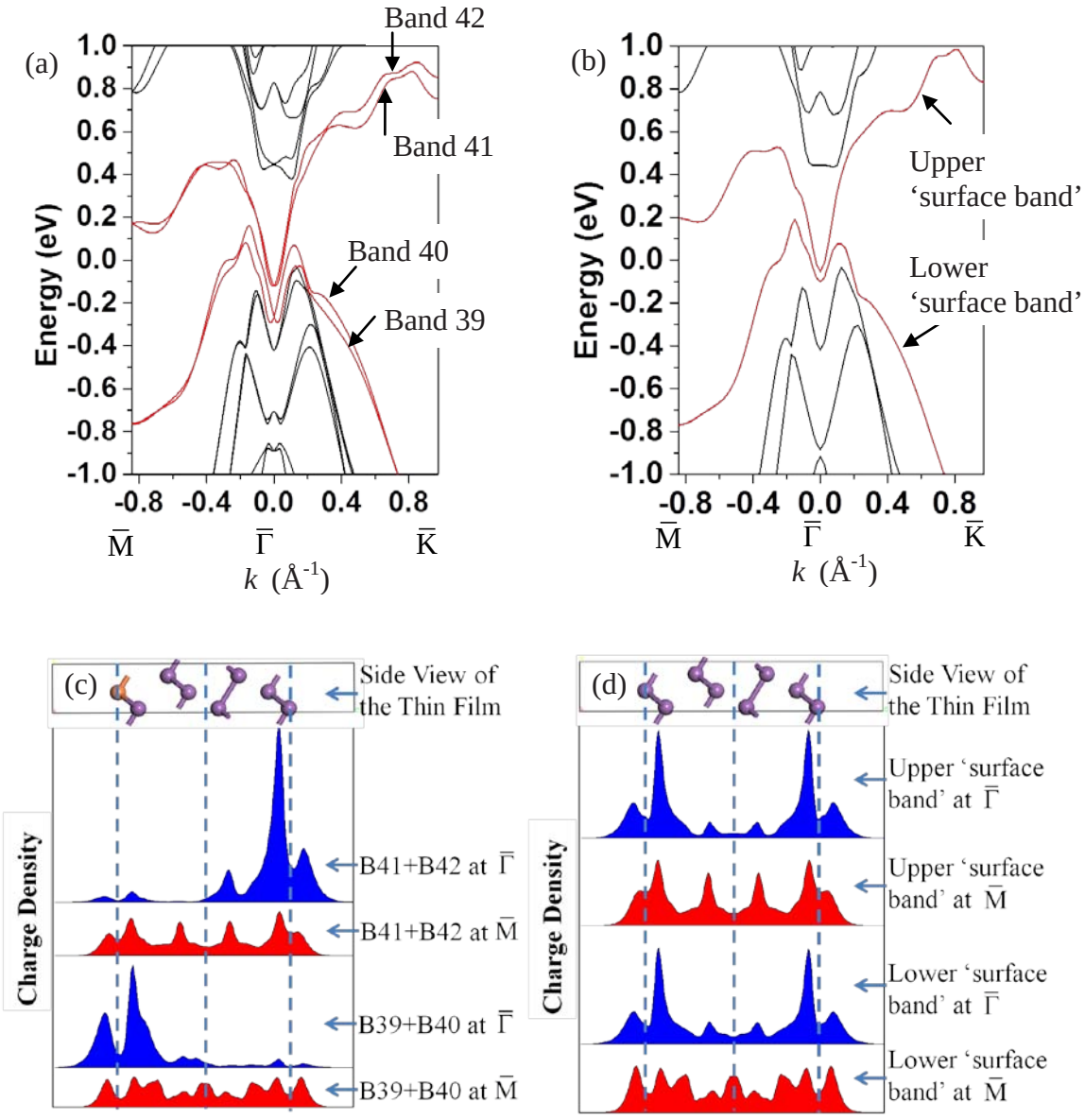

Fig. 4.5. (a) Band structure of Bi-Sb terminated 4 BL Sb(111) film along $\bar{M}$-$\bar{\Gamma}$-$\bar{K}$. The bottom-most Sb atom is replaced with one Bi atom to simulate the SIA effect. 'Surface bands' are indicated in red. (b) Band structure of the freestanding 4 BL Sb(111) film along $\bar{M}$-$\bar{\Gamma}$-$\bar{K}$. 'Surface bands' are indicated in red. There is a surface energy gap of 46 meV due to inter-surface coupling. (c) Charge distribution along the surface normal direction of the Bi-Sb terminated 4 BL Sb(111) film. The purple circles indicate Sb atoms. The purple lines indicate covalent bonds. The brown circle indicates Bi atom. (d) Charge distribution along the surface normal direction of the freestanding 4 BL Sb(111) film.

To look at the detail of the surface band dispersion in Fig. 4.5(a), band structure near the SBZ centre featuring only surface states along $\bar{M}$-$\bar{\Gamma}$-$\bar{M}$ is shown Fig. 4.6(a). If we define $\bar{\Gamma}$-$\bar{M}$ direction as k_x direction, k ranges from -0.1 $\bar{\Gamma}$-$\bar{M}$ (-0.084 Å^{-1}, 0) to 0.1 $\bar{\Gamma}$-$\bar{M}$ (0.084 Å^{-1}, 0) in Fig. 4.6(a). The pair of band 39 and 40, or the pair of band 41 and 42 split for $k \neq 0$, forming Rashba-type splitting bands. The charge distributions near $\bar{\Gamma}$, at (-0.02 Å^{-1}, 0) (indicated as (1), (2), (3) and (4)) were calculated, as shown in Fig 4.6(b). The lower two bands (band 39 and 40) and the upper two bands (band 41 and 42) reside mainly on the bottom and top surfaces, respectively, the same as that at $\bar{\Gamma}$ (see Fig. 4.5(c)). However, charge distributions further away from $\bar{\Gamma}$ are different. The charge distributions of the four bands at (-0.084 Å^{-1}, 0) (indicated as (5), (6), (7) and (8)) are shown in Fig. 4.6(c). The states at (5)/(8) reside mainly on the same surface as that at (1)/(4). However, the state at (6)/(7) reside mainly on different surfaces as that at (2)/(3).

To quantitatively study the real-space charge distributions, the percentage of charge in the top half of the film for each band at each k point, $P_{\mathrm{Top}}(k)$, along $\bar{M}$-$\bar{\Gamma}$ are calculated (which will be shown in Fig. 4.7(a) and (b)). We re-plot Fig. 4.6(a) in Fig. 4.6(d) with spatial charge distribution and spin information. Red and blue indicate different spins. Solid and dash line indicate states mainly in the top half of the film ($P_{\mathrm{Top}}(k) \geq 60\%$) and bottom half of the film ($P_{\mathrm{Top}}(k) \leq 40\%$), respectively. For each band, $P_{\mathrm{Top}}(k)$ changes continuously as a function of k (see Fig. 4.7(a) and (b)). The transition regions ($40\% < P_{\mathrm{Top}}(k) < 60\%$) are indicated by red and blue circles. This charge distribution is a result of a combination of inter-surface coupling and SIA effect, as illustrated schematically in Fig. 4.6(e). The black lines indicate the degenerate states in k-space. Red and blue lines indicate spin non-degenerate states with different spins. Solid and dash lines indicate

states residing mainly on the top and bottom surfaces, respectively. The left-most diagram shows degenerate surface states for thick Sb(111) that are composed of two highly warped Dirac cones, with one spin-polarized Dirac cone residing on each surface of the film. Inter-surface coupling can open an energy gap at the Dirac point. In this case, states are degenerate in both real space and *k*-space. If only SIA is introduced, space inversion symmetry along the surface normal direction is broken, resulting in the relative shift in energy for the two Dirac cones on different surfaces, hence lift the degeneracy in *k*-space. In this case, the states are non-degenerate in both real space and *k*-space. If inter-surface coupling is introduced together with SIA, the intersection points (same ***k*** and E) in *k*-space, indicated by two arrows in Fig. 4.6(e), are most affected. Since inter-surface coupling is the quantum tunneling of electrons between different surfaces, which requires conservation of momentum and energy (same ***k*** and E). Quantum tunneling again opens an energy gap at the intersection points thereby making the states distribute on both top and bottom half of the thin film near the intersection points (the circles in Fig. 4.6(d)). These first-principles calculations results of charge distributions for topological surface bands are in agreement with the effective continuous model[19] calculation results.

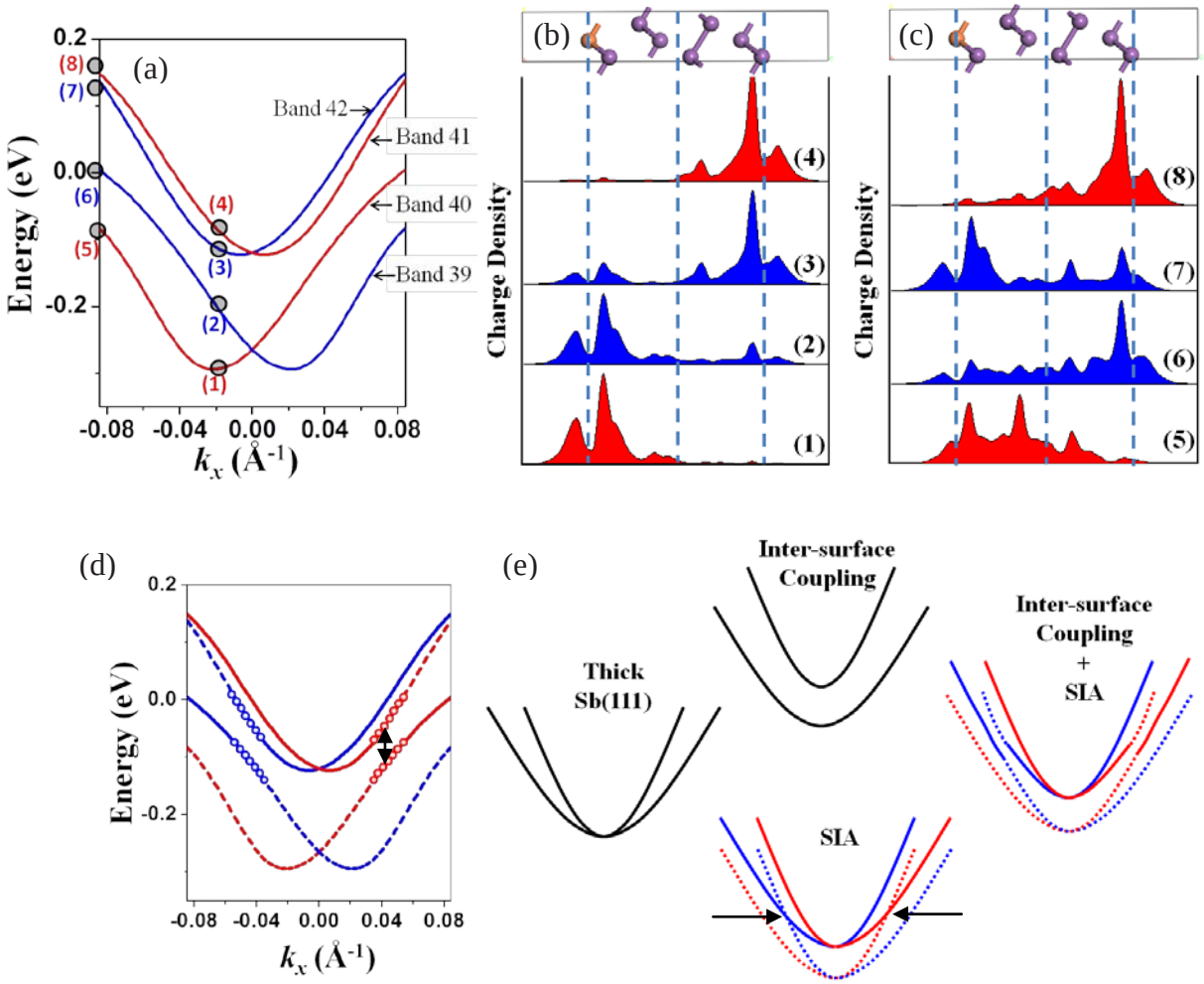

Fig. 4.6. Band structure and real-space charge distributions of the Bi-Sb terminated 4 BL Sb(111) surface states. (a) Calculated band structure along $\bar{M}$-$\bar{\Gamma}$-$\bar{M}$ direction featuring surface states near the SBZ centre, from -0.1 $\bar{\Gamma}$-$\bar{M}$ (-0.084 Å^{-1}, 0) to 0.1 $\bar{\Gamma}$-$\bar{M}$ (0.084 Å^{-1}, 0). Red and blue indicate different spins. (b) Charge distributions at (-0.02 Å^{-1}, 0) of the four bands, indicated by (1), (2), (3) and (4), respectively, in panel (a). (c) Charge distributions at (-0.084 Å^{-1}, 0) of the four bands, indicated by (5), (6), (7) and (8), respectively, in panel (a). (6) and (2) are from the same band but residing on different surfaces; the same is true with (7) and (3). (d) The same as panel (a), with extra spatial charge distribution information. Solid and dash lines represent states residing mainly on top ($P_{\mathrm{Top}}(k) \geq 60\%$) and bottom ($P_{\mathrm{Top}}(k) \leq 40\%$) half of the thin film, respectively. Circles indicate states in the transition region ($40\% < P_{\mathrm{Top}}(k) < 60\%$). The black arrow indicates an energy gap of 68 meV. (e) Cartoon schematic of the evolution of TSS with inter-surface coupling effect, SIA effect and a combination of both.

Fig. 4.7 (a) and (b) show $P_{Top}(k)$ of the four 'surface bands' as a function of k_x (k_y = 0). The four 'surface bands' are band 39, 40, 41 and 42, respectively. The pair of band 39 and 40 show approximately symmetrical distributions far away from $\bar{\Gamma}$, and distribute almost equally on two halves of the thin film, hence we can consider these states as spin degenerate in real space. Strictly speaking, these states should be called surface resonant states rather than surface states (Surface states are localized at the surface and, in terms of band energy, they are located in gaps of the bulk projected band structure. Surface resonant states are localized partially at the surface region and extend into the slab. In terms of the band energy, they overlap with the bulk projected band structure). As k approaches to $\bar{\Gamma}$, the states show tendency to accumulate on one surface. This is obvious from (-0.18 $Å^{-1}$, 0), where $P_{Top}(k)$ of the band 40 and 39 is about 60% and 35%. The high proportion of one band (band 40) over the other (band 39) residing on the top surface results in the spin polarization of these states.

The same evolutionary trend is shown for $P_{Top}(k)$ of bands 41 and 42, except that there are abrupt changes at k_x = -0.58, -0.42, -0.27 and -0.16 from $\bar{M}$ to $\bar{\Gamma}$, as indicated by arrows in Fig. 4.7(b). All four points here are intersection points between band 41 and 42, as shown by two solid arrows in Fig. 4.7(c). For convenience, we define the region from -0.27 < k_x < -0.16 as region I, and -0.16 < k_x < 0 as region II, as indicated in Fig. 4.7(b) and (c). Fig. 4.7(c) is the calculated band structure along $\bar{M}$-$\bar{\Gamma}$-$\bar{M}$ with spatial charge distribution and spin information. In both region I and II, the lower/higher bands are classified as band 41/42, but physically, the band 42/41 in region I and band 41/42 in region II should belong to the same band. This is the reason why $P_{Top}(k)$ changes abruptly in the intersection points. In Fig. 4.7(c), near $\bar{\Gamma}$, the meaning of blue and red colors, dash

and solid lines or circles are the same as in Fig. 4.6(d). Away from $\bar{\Gamma}$, the states are surface resonant states. The transition from surface states (near $\bar{\Gamma}$) to surface resonant sates is smooth, but we draw the states for $|k_x| \gtrsim 0.18$ ($P_{\mathrm{Top}}(k)$ are within 40% to 60%) in black for clarity. The surface resonant states can be considered to be spin-degenerate.

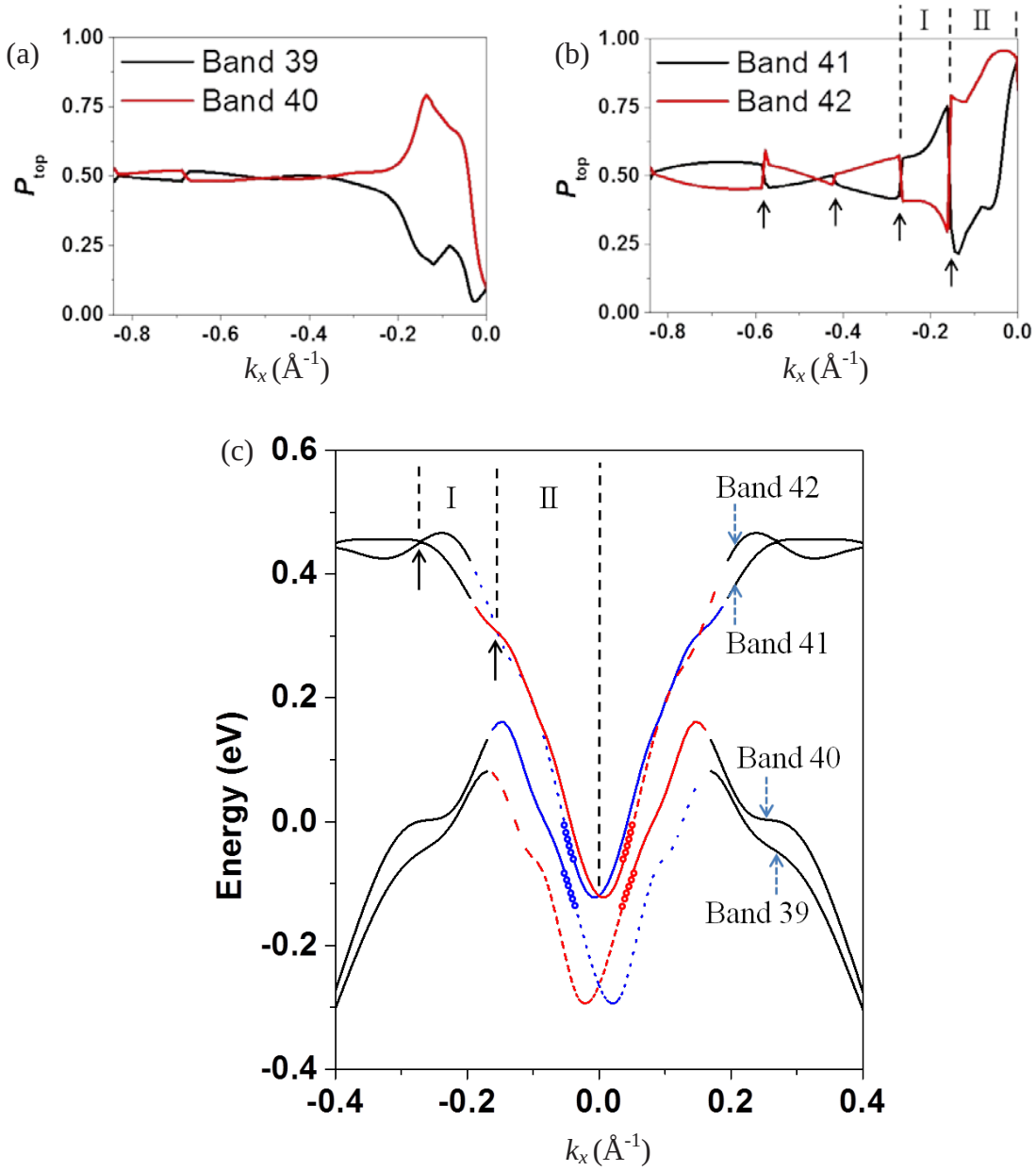

Fig. 4.7. (a) $P_{\mathrm{Top}}(k)$ of band 39 and 40. (b) $P_{\mathrm{Top}}(k)$ of band 41 and 42. (c) Band structure along $\bar{\mathrm{M}}$-$\bar{\Gamma}$-$\bar{\mathrm{M}}$ direction featuring surface bands of the Bi-Sb terminated 4 BL Sb(111) film.

Based on the 'surface bands' and spin textures, calculated CEC at Fermi energy are shown in Fig. 4.8(a). It is projected surface states from -10 mV to 10 mV. The width of the line depends on the slope of the surface states. The two electron pockets near $\bar{\Gamma}$ are spin-polarized, the spin directions are indicated by the gradient colors. The surrounding states far away from $\bar{\Gamma}$, shown in grey, are spin-degenerate surface resonant states. These degenerate states are more abundant in $\bar{\Gamma}$-$\bar{M}$ direction than in $\bar{\Gamma}$-$\bar{K}$ direction, because of asymmetric warping in $\bar{\Gamma}$-$\bar{M}$ and $\bar{\Gamma}$-$\bar{K}$ (see Fig. 4.5(a)). We can consider the six abundant surrounding states in $\bar{\Gamma}$-$\bar{M}$ direction as the hole pockets. The scattering events including the abundant states in $\bar{\Gamma}$-$\bar{M}$ direction (six hole pockets) must be dominant compared with that involving the states in $\bar{\Gamma}$-$\bar{K}$ direction.

Now we discuss the origins of the three main wavevectors $\mathbf{q_B}$, $\mathbf{q_E}$ and $\mathbf{q_F}$ in Fig. 4.4(e), which are re-plotted in Fig. 4.8 (b). Scattering between the two electron pockets and the hole pockets results in the short scattering wavevector $\mathbf{q_B}$ in $\bar{\Gamma}$-$\bar{M}$ direction**.** Scattering between the nearest electron pockets ($\mathbf{q'_B}$ in Fig. 4.8(a)) should also contribute to $\mathbf{q_B}$ in Fig. 4.8(b). The longest scattering wavevector $\mathbf{q_E}$ along $\bar{\Gamma}$-$\bar{M}$ direction corresponds to the scattering between the farthest two hole pockets. The second-longest scattering wavevector $\mathbf{q_F}$ along $\bar{\Gamma}$-$\bar{K}$ direction corresponds to the scattering between the second-nearest hole pockets. The angle between $\mathbf{q_E}$ and $\mathbf{q_F}$ is 30°. From Fig. 4.8(a), it is obvious that $|\mathbf{q_F}|/|\mathbf{q_E}|$ is $\sqrt{3}/2$, which explains that $\mathbf{q_E}$ and $\mathbf{q_F}$ form a hexagon in Fig. 4.8(b). The two concentric electron pockets have reverse spin textures, the state with a particular spin direction in one electron pocket can be scattered backward to the other electron pocket with the same spin direction. The most probable scattering without spin direction

change is indicated by $\mathbf{q_A}$. $\mathbf{q_A}$ is allowed in any direction, which should form a ring with a quite small radius in the FT-STS, and be partially responsible for the high intensity near the SBZ centre in Fig. 5.8(b). Fig. 5.8(c) is the simulated FT-STS based on the CEC in Fig. 5.8(a). This simulation revealed two strong intensity spots in $\bar{\Gamma}$-$\bar{M}$ direction and one strong intensity spot in $\bar{\Gamma}$-$\bar{K}$ direction, which are in good agreement with the experimental results.

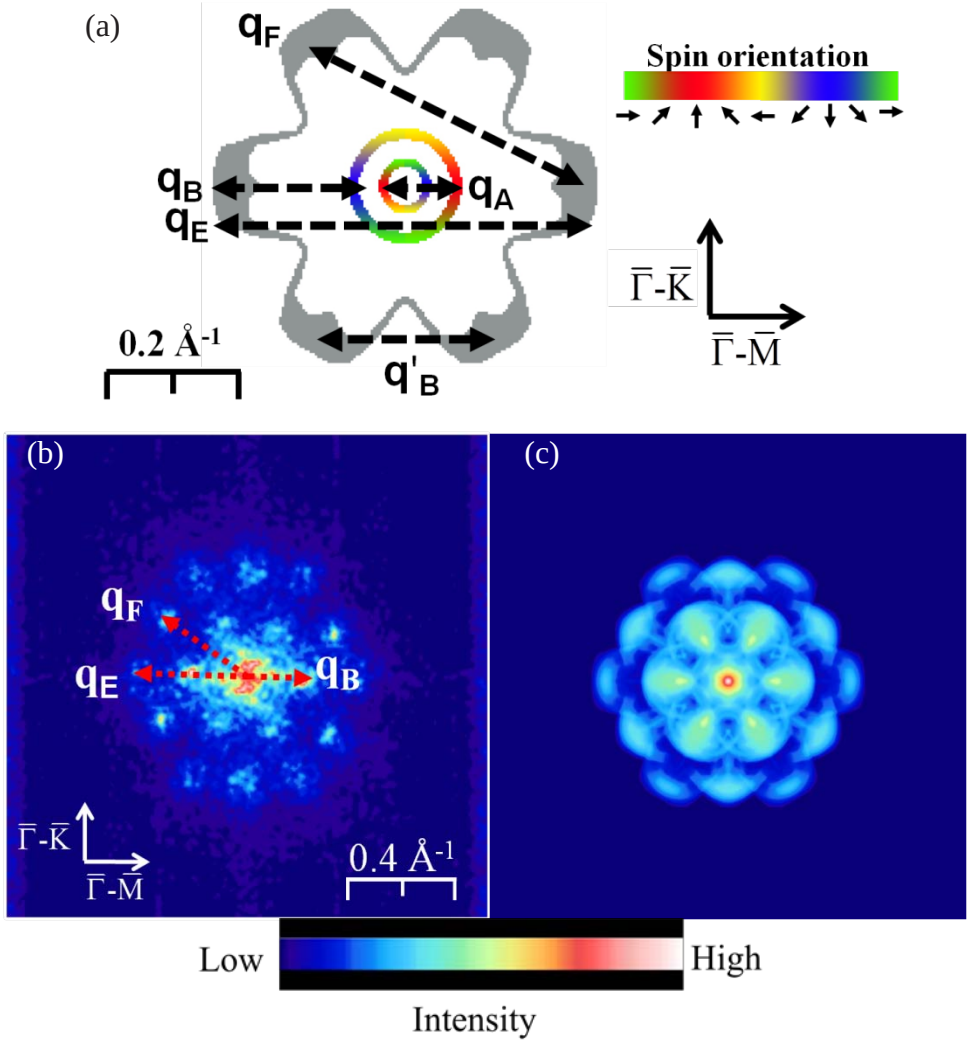

Fig. 4.8. (a) Calculated CEC of the Bi-Sb terminated 4 BL Sb(111) at Fermi level. The gradient colors indicate spin directions of the two electron pockets. The degenerate surface resonant states are shown in grey. Scattering wavevectors are indicated by $\mathbf{q_A}$, $\mathbf{q_B}$, $\mathbf{q'_B}$, $\mathbf{q_E}$, and $\mathbf{q_F}$, respectively. (b) The FT-STS at -80 mV. (c) Simulated FT-ST at Fermi level based on the CEC from panel (a).

4.3.3 Weakening of the SIA effect on thicker film

The influence of the substrate on the top surface states is by means of inter-surface coupling. Suppose there is no inter-surface coupling, *i.e.*, the film is thick enough, the influence of the substrate should decrease. Considering the limiting case in which the film is infinitely thick, it is impossible for the substrate condition to affect the top surface band structure. To validate this intuitive thought, calculations of states at thicker film are needed.

Fig. 4.9(a) shows the calculated surface band structure of the Bi-Sb terminated 5 BL Sb(111) near $\bar{\Gamma}$ from -0.1 $\bar{\Gamma}$-$\bar{M}$ (-0.084 Å^{-1}, 0) to 0.1 $\bar{\Gamma}$-$\bar{M}$ (0.084 Å^{-1}, 0), with the zoom-in dash rectangular area shown in Fig. 4.9(b). As in the case of Bi-Sb terminated 4 BL Sb(111), the four bands are classified as band 49, 50, 51 and 52. At first glance, the band structure seems quite complicated. To understand this dispersion, the percentage of charge in the top half of the film for each band at each k point, $P_{\mathrm{Top}}(k)$, along $\bar{M}$-$\bar{\Gamma}$ direction is calculated, as shown in Fig. 4.9(c) and (d). The k_x in the left panel of 4.9(c) and (d) ranges from -0.84 to 0 ($\bar{M}$ to $\bar{\Gamma}$), while k_x in the right panel ranges from -0.084 to 0 to zoom $P_{\mathrm{Top}}(k)$ near $\bar{\Gamma}$. Compared with $P_{\mathrm{Top}}(k)$ of 4 BL film (see Fig. 4.7), there are two differences for $P_{\mathrm{Top}}(k)$ of 5 BL film. First, $P_{\mathrm{Top}}(k)$ are nearly 100% or 0% near $\bar{\Gamma}$, indicating that the states are more localized in one side of the film. Second, the change of $P_{\mathrm{Top}}(k)$ between low and high values is abrupt near $\bar{\Gamma}$, almost without any transition area. We re-plot the surface band structure with the spatial charge distribution and spin information in Fig. 4.9(e). It is very clear that the bands consist of two sets of Rashba-type splitting bands, with one on the top surface and the other on the bottom surface.

There are two crossings in the $\bar{\Gamma}$-$\bar{M}$ direction from Fig. 4.9(e). The red dash line and red solid line cross each other at (0.0086 $Å^{-1}$, 0). The red dash line and blue solid line cross each other at (0.028 $Å^{-1}$, 0). It is interesting to note that the former crossing induced an energy gap of 4 meV, as shown in Fig. 4.9(b) by the red arrow, while the latter crossing has no energy gap at all, indicated by the green arrow in Fig. 4.9(b). The former crossing (red dash and red solid) opens an energy gap due to quantum tunneling, while at the latter crossing (red dash and green solid) point, quantum tunneling is insignificant because penetration depth is shorter.

SIA effect shifts the bottom surface band in energy with respect to the top surface band, hence protects the surface bands from opening a gap at $\bar{\Gamma}$. But at other degenerate points, like the red dash and red solid crossing point in Fig. 4.9(e), quantum tunneling is allowed and an energy gap can still open. Compared with the 68 meV energy gap for the Bi-Sb terminated 4 BL Sb(111) in Fig. 4.6(d), the gap of the 5 BL case in Fig. 4.9 (b) is just about 4 meV. The shrink of the energy gap at the intersection points, the high (nearly 100%) or low value (nearly 0%) of $P_{\mathrm{Top}}(k)$ near $\bar{\Gamma}$ as well as the abrupt change from high/low to low/high value for $P_{\mathrm{Top}}(k)$ near $\bar{\Gamma}$ indicate that the inter-surface coupling effect is significantly reduced in the thicker film. For sufficiently thick film grown on substrate, though the SIA is still present, the top surface states cannot ‘feel’ it.

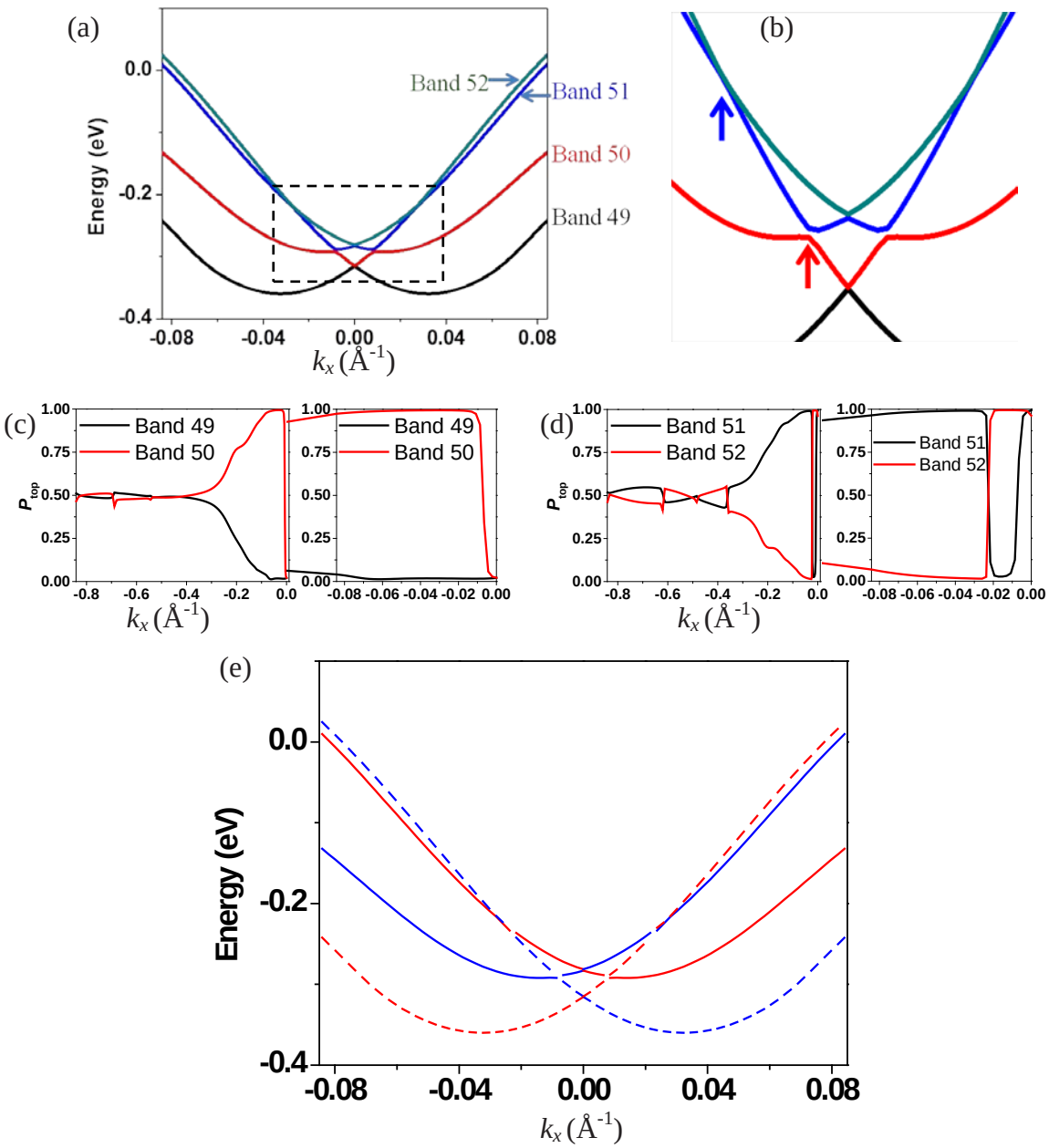

Fig. 4.9. Calculated surface band structure and real-space charge distributions of the Bi-Sb terminated 5 BL Sb(111). (a) Band structure along $\bar{M}$-$\bar{\Gamma}$-$\bar{M}$ direction featuring surface states near the SBZ centre, from -0.1 $\bar{\Gamma}$-$\bar{M}$ (-0.084 Å-1, 0) to 0.1 $\bar{\Gamma}$-$\bar{M}$ (0.084 Å-1, 0). (b) The zoom-in dash square in panel (a). (c) P_{Top}(k) of band 49 and 50. (d) P_{Top}(k) of band 51 and 52. (e) The same as panel (a), with extra spatial charge distribution information. Red and blue indicate different spins. Solid and dash lines represent states residing on top and bottom surfaces, respectively.

4.4 Conclusions

In this chapter, *in-situ* STM/STS studies together with DFT calculations on 30 BL, 9 BL, 4 BL Sb(111) films are demonstrated. The surface states on 30 BL Sb(111) are TSS affected little by inter-surface coupling. Scatterings are significantly reduced due to the spin-polarized TSS. On the 9 BL film, the surface states near $\bar{M}$ are affected most by inter-surface coupling due to longer penetration depth, and become surface resonant states. While the states near $\bar{\Gamma}$ remain spin-polarized TSS. On 4 BL Sb(111), the supposed surface gap is not observed experimentally by ARPES[18] because of the SIA effect. By replacing one Sb atom at the bottom surface layer by one Bi atom in each unit cell of 4 BL Sb(111), the SIA effect is simulated from first-principles calculations. The SIA lifts the degeneracy of the bands in *k*-space. Since quantum tunneling requires conservation of energy and momentum, the removed degeneracy near the SBZ centre protects the surface states from opening an energy gap. The calculated real-space distributions of the states are in agreement with the effective continuous model[19] calculation results. The simulated FT-STS is in good agreement with the experimental results. Calculations of the Bi-Sb terminated 5 BL Sb(111) show that the effect of the SIA on thicker film is weakened.

References

[1] D. Hsieh *et al.*, Observation of Unconventional Quantum Spin Textures in Topological Insulators. *Science* **323**, 919 (2009).

[2] D. Hsieh *et al.*, Direct observation of spin-polarized surface states in the parent compound of a topological insulator using spin- and angle-resolved photoemission spectroscopy in a Mott-polarimetry mode. *New Journal of Physics* **12**, 125001 (2010).

[3] K. K. Gomes *et al.*, Quantum Imaging of Topologically Unpaired Spin-Polarized Dirac Fermions. *arXiv:0909.0921v2* (2009).

[4] K. Sugawara *et al.*, Fermi Surface and Anisotropic Spin-Orbit Coupling of Sb(111) Studied by Angle-Resolved Photoemission Spectroscopy. *Physical Review Letters* **96**, 046411 (2006).

[5] T. Kadono *et al.*, Direct evidence of spin-polarized band structure of Sb(111) surface. *Applied Physics Letters* **93**, 252107 (2008).

[6] J. Seo *et al.*, Transmission of topological surface states through surface barriers. *Nature* **466**, 343 (2010).

[7] Y. Liu, R. E. Allen, Electronic structure of the semimetals Bi and Sb. *Physical Review B* **52**, 1566 (1995).

[8] P. Zhang, Z. Liu, W. Duan, F. Liu, J. Wu, Topological and electronic transitions in a Sb(111) nanofilm: The interplay between quantum confinement and surface effect. *Physical Review B* **85**, 201410 (2012).

[9] Y. Zhang *et al.*, Crossover of the three-dimensional topological insulator Bi2Se3 to the two-dimensional limit. *Nature Physics* **6**, 584 (2010).

[10] Y.-Y. Li *et al.*, Intrinsic Topological Insulator Bi2Te3 Thin Films on Si and Their Thickness Limit. *Advanced Materials* **22**, 4002 (2010).

[11] G. Yao *et al.*, Evolution of Topological Surface States in Antimony Ultra-Thin Films. *Scientific Reports* **3**, 2010 (2013).

[12] M. Neupane *et al.*, Tunneling Tuned Spin Modulations in Ultrathin Topological Insulator Films. *arXiv:1307.5485*, (2013).

[13] M. Konig *et al.*, Quantum Spin Hall Insulator State in HgTe Quantum Wells. *Science* **318**, 766 (2007).

[14] I. Knez, R.-R. Du, G. Sullivan, Evidence for Helical Edge Modes in Inverted InAs/GaSb Quantum Wells. *Physical Review Letters* **107**, 136603 (2011).

[15] F. Yang *et al.*, Spatial and Energy Distribution of Topological Edge States in Single Bi(111) Bilayer. *Physical Review Letters* **109**, 016801 (2012).

[16] Z. F. Wang *et al.*, Creation of helical Dirac fermions by interfacing two gapped systems of ordinary fermions. *Nature Communication* **4**, 1384 (2013).

[17] C. Sabater *et al.*, Topologically Protected Quantum Transport in Locally Exfoliated Bismuth at Room Temperature. *Physical Review Letters* **110**, 176802 (2013).

[18] G. Bian, X. Wang, Y. Liu, T. Miller, T. C. Chiang, Interfacial Protection of Topological Surface States in Ultrathin Sb Films. *Physical Review Letters* **108**, 176401 (2012).

[19] W.-Y. Shan, H.-Z. Lu, S.-Q. Shen, Effective continuous model for surface states and thin films of three-dimensional topological insulators. *New Journal of Physics* **12**, 043048 (2010).

[20] P. E. Blöchl, Projector augmented-wave method. *Physical Review B* **50**, 17953 (1994).

[21] G. Kresse, D. Joubert, From ultrasoft pseudopotentials to the projector augmented-wave method. *Physical Review B* **59**, 1758 (1999).

[22] J. P. Perdew, K. Burke, M. Ernzerhof, Generalized Gradient Approximation Made Simple. *Physical Review Letters* **77**, 3865 (1996).

[23] J. P. Perdew, K. Burke, M. Ernzerhof, Generalized Gradient Approximation Made Simple [Phys. Rev. Lett. 77, 3865 (1996)]. *Physical Review Letters* **78**, 1396 (1997).

[24] H. J. Monkhorst, J. D. Pack, Special points for Brillouin-zone integrations. *Physical Review B* **13**, 5188 (1976).

[25] P. Roushan *et al.*, Topological surface states protected from backscattering by chiral spin texture. *Nature* **460**, 1106 (2009).

[26] G. Bian, T. Miller, T. C. Chiang, Passage from Spin-Polarized Surface States to Unpolarized Quantum Well States in Topologically Nontrivial Sb Films. *Physical Review Letters* **107**, 036802 (2011).

[27] M. Wada, S. Murakami, F. Freimuth, G. Bihlmayer, Localized edge states in two-dimensional topological insulators: Ultrathin Bi films. *Physical Review B* **83**, 121310 (2011).

Chapter 5

Atomic and Electronic Structures of Sb(110) Thin Films

5.1 Introduction

Though the exploration of Sb(111) is abundant, few experimental studies have been performed on Sb(110), since (110) surface is not the natural cleavage plane of Sb. So far, there are only two papers regarding the surface states on the bulk Sb(110) to our knowledge, written by M. Bianchi *et al.*[1] and A. Strozecka *et al.*[2] The latter paper[2] revealed the absence of direct backscattering of the surface states, which requires spin flip and is forbidden for spin-polarized TSS in TRS system. The former[1] studied electronic structures by using ARPES and first-principles calculations. The paper contributes to our understanding of the surface states of Sb(110) in two ways. First, the dispersion of states can be interpreted in terms of strong spin-orbit coupling. Second, since the band structure of Sb crystal is topologically nontrivial with a Z_2 invariant $\nu_0 = 1$, the existence of the metallic surface states is constrained, *i.e.*, the surface states cross the Fermi level between two time reversal invariant momenta (TRIMs) an even number of times if the two relevant TRIMs have the same parity and odd times otherwise. However, this constraint is invalid if the projected bulk Fermi surface is present and the surface bands are allowed to mix with the bulk states. Specifically, there are four TRIMs in the SBZ of Sb(110), *i.e.*, $\bar{\Gamma}$, $\bar{X}_1$, $\bar{M}$ and $\bar{X}_2$, with surface fermion parities of -1, -1, -1 and 1, respectively, as shown in Fig. 5.1(a). The surface states should cross Fermi level between any two of $\bar{\Gamma}$, $\bar{X}_1$ and $\bar{M}$ even times, since the surface fermion parities of the three

TRIMs are the same. This is confirmed by both ARPES and first-principles calculations. The calculated band structure are shown in Fig. 5.1(b). The surface states should cross Fermi level between $\bar{X}_2$ and any other TRIM odd times. However, both experiment and calculations show even-number crossings, instead of odd. This is because Sb is a semimetal, the surface states near $\bar{X}_2$ lie within the bulk projected states and mix with the bulk states. The mixing of the surface states with bulk state is also responsible for the lifting of the degeneracy at $\bar{X}_2$.

As Sb(110) surface is difficult to be obtained from bulk crystal, the preparation and characterization of the properties of Sb(110) surface are interesting. For thin film growth, HOPG is an inert substrate, which is good for minimizing the substrate effect. By controlling the deposition flux and substrate temperature, Sb_4 deposited on HOPG could form finger-like nanoparticles,[3] Sb(111) 2D structure above thickness of 3 nm and compressed Sb(110) nanorods above thickness of 15 nm.[4-6] Thanks to the Sb source that crack Sb_4 into single atoms, as discussed in Chapter 3, we can grow Sb(110) films as thin as 2 ML on HOPG.

In this chapter, the growth of ultrathin Sb(110) films or nanobelts on HOPG is demonstrated. The atomic structures of ultrathin Sb(110) are proposed. Calculated DOS based on the proposed atomic structures is in reasonable agreement with the measured STS. Unlike in the case of Sb(111) thin films, we did not find repeatable energy dependent QPI patterns on Sb(110) thin films, and the reasons for the lack of QPI patterns on ultrathin Sb(110) are discussed. A 4× reconstruction on the edge of Sb(110) thin film along $\left[0\bar{1}1\right]$ direction was observed.

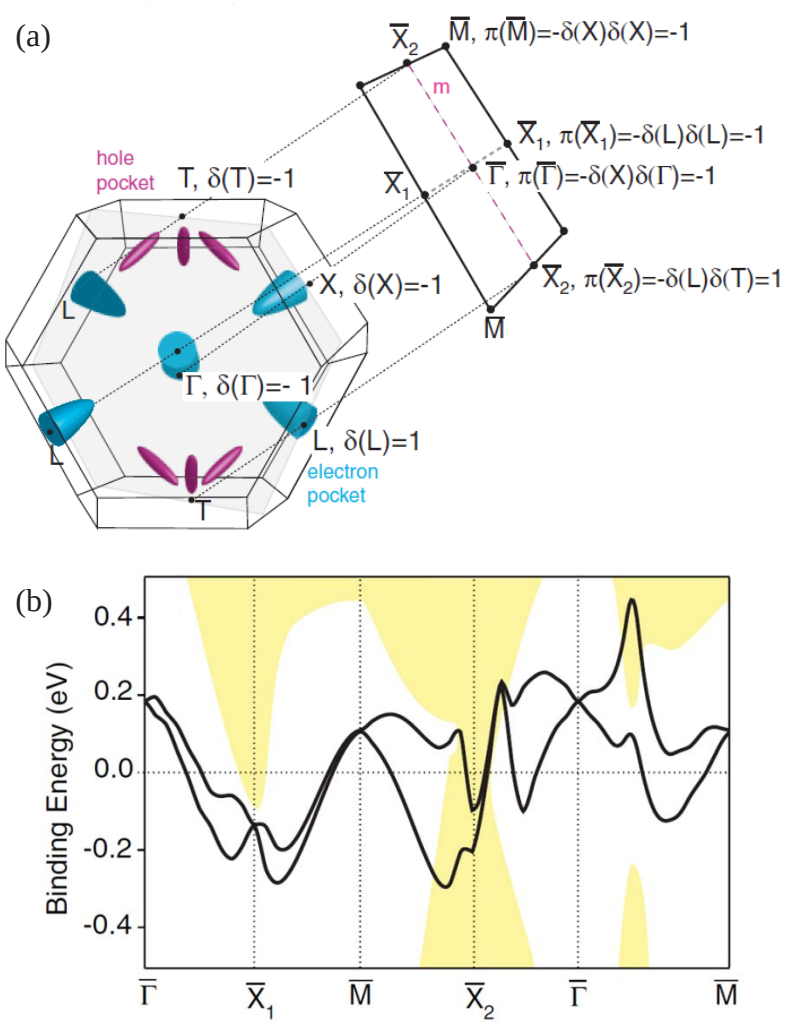

Fig. 5.1. (a) Bulk BZ of Sb, together with a projection onto the Sb(110) SBZ. (b) Calculated surface state dispersion. The yellow continuum is the projected bulk band structure. (Reprinted from Ref. [1] by permission from American Physical Society)

5.2 Experimental and computational methods

The experiments are carried out in a Unisoku UHV LT-STM system. All the STM measurements are performed at LN_2 temperature. The base pressure is 9×10^{-11} Torr. The freshly cleaved HOPG is loaded to the STM chamber, annealed at 520 °C overnight and serves as the substrate. The surface condition of HOPG is checked with STM. High purity (99.999%) Sb is deposited on HOPG at RT. Before deposition, the Sb source is degassed at appropriate temperature for 30 min in order to remove contamination. The flux of Sb is 0.36 ML/min (1 ML is defined as 1 monolayer of Sb(110), *i.e.*, 10.3×10^{14} cm^{-2}), which is calibrated by growing flat Sb(111) thin film on Si(111) and measuring the film thickness. However, the effective flux deposited on HOPG may possibly be lower than 0.36 ML/min, taking into account of the fact that HOPG is inert, thus reducing the adsorption rate compared with that on Si(111). The STS data are acquired using a lock-in amplifier with the bias voltage modulated at a frequency of 700 Hz and peak-to-peak amplitude of 10 mV.

The computational methods are the same as described in Chapter 3.

5.3 Results and discussion

5.3.1 Growth mode

Fig. 5.2 shows the STM images of Sb nanostructures with different coverage on HOPG. At 2.2-ML deposition amount, islands formed along the HOPG step edges. The islands along the same step edge are close, but not connected to each other, because they grown

from different nucleation centers. The thinnest islands are 8 Å in height, on which residing 6.2 Å height islands, as shown in Fig. 5.2 (a) and (b). Upon more Sb deposition (5.0 ML), the main part of the islands is (6.2 + 6.2 + 8) Å in height, as shown in Fig. 5.2(c) and (d). A small part of the island is (6.2 + 8) Å in height, indicated by the red arrow, and another small part is (6.2 + 6.2 + 6.2 + 8) Å in height, indicated by the black arrows. The atomic-resolution STM image shows a rectangular unit cell of 4.55 Å × 4.35 Å, which is approximately the unit cell of bulk (110) surface (4.51 Å × 4.31 Å). The thickness of 2 ML Sb(110) is 6.2 Å. The 8 Å height structure is not well defined. Since large area of 8 Å height island does not exist independently, and 8 Å is not an integral number of thickness of low-index Sb atomic layer, such as Sb(110) or Sb(111), we regard this layer as a wetting layer, which separate the Sb(110) islands from the substrate. We regard this as wetting layer for another reason: The 8 Å thickness layer does not contribute to the DOS (see below). We indicate the 2 ML islands on the wetting layer as '2 + W', and similarly for islands of other thicknesses in Fig. 5.2 and Fig. 5.3, while in the text, for simplicity, we refer them as 2 ML Sb(110) only, and so forth for islands of other thicknesses.

The odd-ML films from 1 to 5 are not observed. This even-ML-film growth on wetting layer reminds us the growth of Bi on HOPG[7] and Si.[7, 8] Bi grown on HOPG forms 2 ML, 4 ML and 6 ML nanostructures on a 1-ML height wetting layer, and the 1-ML wetting layer does not contribute to the DOS.[7] The Bi grown on Si (111) also forms a wetting layer of < 2 ML on which 2 and 4 ML Bi(110) grow.[8] More Bi on Si(111) forms Bi(111), because Bi(110) has lower energy than Bi(111) for thinner films but reversed for thicker films.[8] By the way, the thinnest Sb(111) film on Si(111) is also 4 BL, this is

because below 4 BL deposition, only amorphous wetting layer can form without crystallization (see Chapter 3). Neither Bi wetting layer on Si(111) nor 1-ML height Bi wetting layer on HOPG makes a significant contribution to the electronic structures of the Bi(111) nanostructures.[7, 9] The similar growth mode between Bi and Sb on HOPG and Si is not surprising since both bulk Sb and Bi crystallize in the rhombohedral A7 structure in ambient conditions and share the same outer electronic structure[10] as group V semimetals. In this chapter, besides the Sb(110) thin film itself, we also address the extensively studied case of Bi(110) for reference.

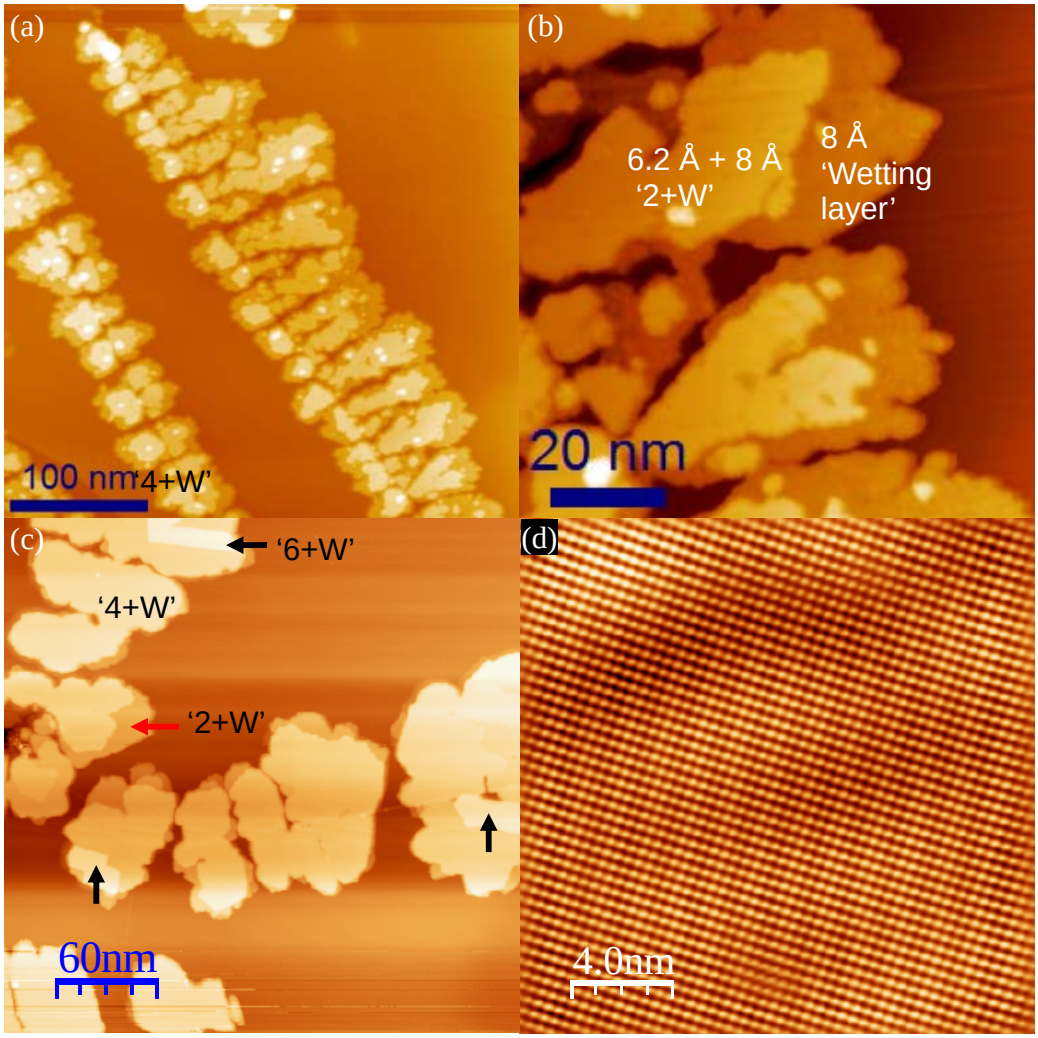

Fig. 5.2. STM images of 2.2-ML and 5.0-ML Sb deposited on HOPG at RT. (a) and (b) 2.2-ML Sb, forming mainly '2+W' ML films. (c) 5.0-ML Sb, forming mainly '4+W' ML films. '6+W' ML islands are indicated by black arrows. (d) An aomic-resolution STM image of '4+W' ML thin film, with sample bias voltage V_s = -0.01 V and tunneling current = 0.11 nA. The rectangular unit cell size is 4.55 × 4.35 Å.

As 8.6-ML Sb is deposited on HOPG, the main films are 6 ML Sb(110), as shown in Fig. 5.3(a). Meanwhile, we can observe odd-ML Sb(110) on 6 ML Sb(110), indicated by the blue arrows. Zoom-in STM image at the top-right area of Fig. 5.3(a) indicated by the blue arrow is shown in Fig. 5.3(b), where 6 to 9 ML Sb(110) islands are observed. By depositing more Sb on the sample of Fig. 5.3(a), both even- and odd-ML Sb(110) films of thickness from 6 to 14 ML can be observed, as shown in Fig. 5.3(c).

From the experimental results, it is obvious that Sb(110) follow even-ML growth mode below 6 ML, while above 6 ML both even- and odd-ML films are stable. To understand this growth behavior, the extra energy E_e(n) of relaxed Sb(110) was calculated. E_e(n) is defined in Section 3.1.2, which provides a measure for the relative stability of the n-ML Sb(110) film. Fig. 5.3(d) shows that E_e decreases monotonously with increasing n. E_e(n) should approach zero as n approaches infinity according to our definition. E_e(1) is 708 meV, while E_e(2) reduces dramatically to 187 meV. This dramatic energy reduction from 1 ML to 2 ML thin film indicates that 1 ML is extremely unstable. Note that since E_e(1) is especially large, for better view of other E_e(n), there is a break of vertical axis from 300 meV to 700 meV. Generally speaking, n-layer thin film is not even meta-stable if $E_e(n) > [E_e(n-1) + E_e(n+1)]/2$, since the n-layer thin film can decompose to (n-1)-layer and (n+1)-layer films to reduce energy. To examine the relative stability of thin films of different thicknesses, the energy difference $E_d(n) = E_e(n) - [E_e(n-1) + E_e(n+1)]/2$ is calculated, as shown in Fig. 5.3(e). The physical meaning of E_d(n) can be considered as how much energy is released per atom if an n-layer film of area x is decomposed to (n-1)-layer and (n+1)-layer films of area $x/2$. A negative E_d(n) means an increase in energy after decomposition, and hence indicates n-layer film is stable against

such decomposition. E_d(n) fluctuates around zero. The fluctuation is large for thinner layers below 6, indicating that the energy gain or loss is dramatic if one layer transform to adjacent layers. E_d(2) has a large negative value of -245 meV since E_e(1) is quite large, while for n from 3 to 11, the deviation of E_d(n) from zero is within 20 meV. For better view again, there is a break of vertical axis from -200 meV to -50 meV. The large negative value for E_d(2), E_d(4) and positive value for E_d(3) indicate that 2- and 4-ML films are more stable than the 3-ML film. This is the reason why 3-ML film is not observed in our experiment. For the same reason, 5-ML film is unstable against decomposition to adjacent 4- and 6-ML films. From 7 ML and above, the fluctuations around zero are within 5.2 meV, which means energy difference is quite small between adjacent layers compared with room temperature thermal energy (26 meV), so films of these thicknesses all can exist.

We can compare the growth of Sb on HOPG with that on Si(111) (See Chapter 3). On Si(111), Sb atoms distribute more uniformly because the substrate is chemically active, on which diffusion of the Sb atoms is suppressed and the thin film is quite extended laterally. HOPG is a quite inert substrate so that Sb atoms have a longer diffusion length. The initial nucleation centers are located along the HOPG atomic steps, as shown in Fig. 5.2(a). Sb atoms coalesce into discrete films or islands instead of uniform thin films. Sb(110) films form on HOPG at low coverage. On Si(111), there are also Sb(110) forming at low coverage (See Fig. 3.3(d), Fig. 3.3(f) and Fig. 3.4(b)). However, the post-growth annealing makes the Sb films on Si(111) single crystalline Sb(111) structure.

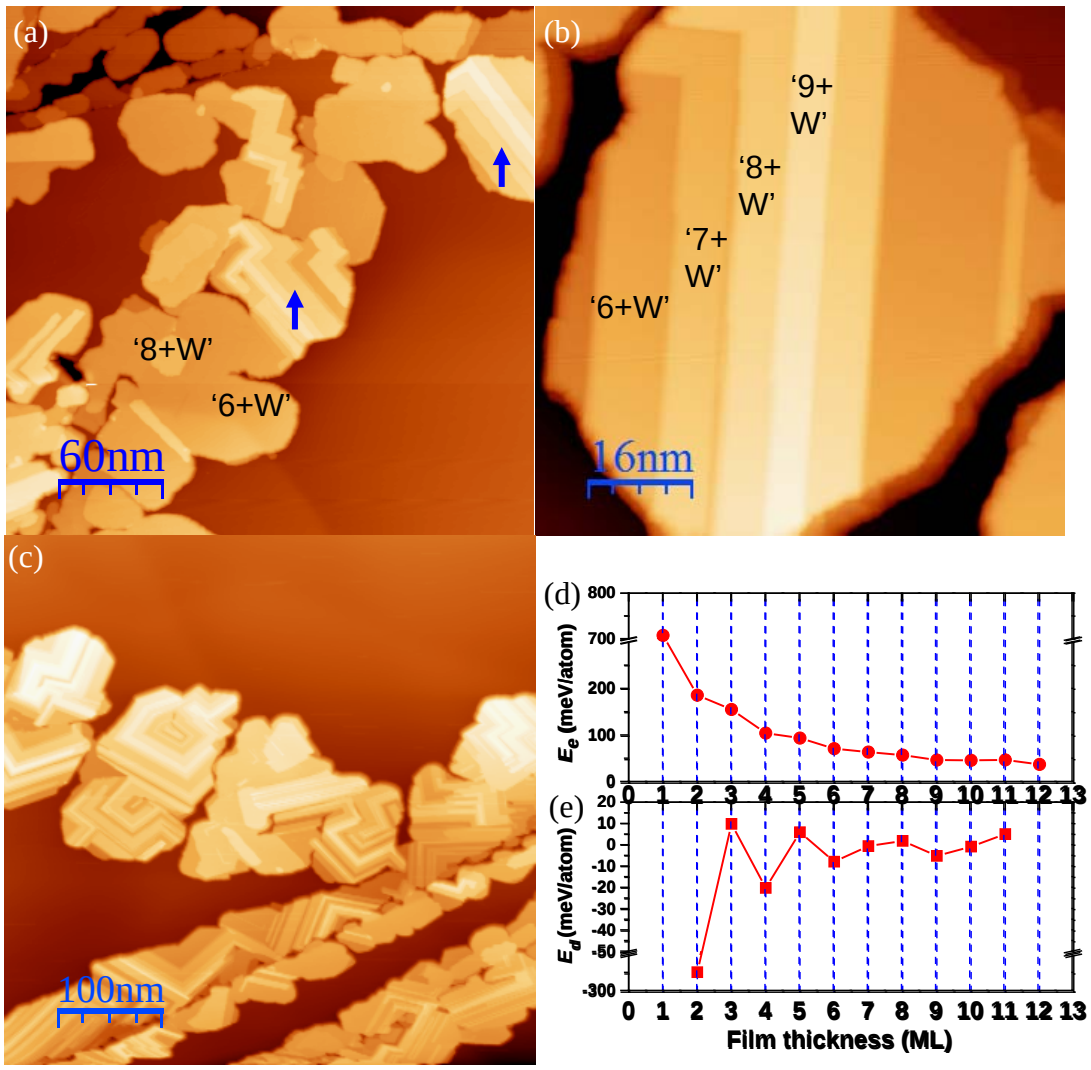

Fig. 5.3. (a) An STM image of 8.6-ML Sb deposited on HOPG at RT, forming mainly '6+W' ML films. The thinnest odd-ML '7+M' island was found, indicated by blue arrows. (b) Zoom-in scans at top-right corner of panel (a) by STM, showing the islands of 6 to 9 ML. (c) An STM image of 12.2-ML Sb deposited on HOPG at RT, single-atomic-step islands over 8 ML is common. (d) The red solid circles are extra energies $E_e(n)$ for n-ML Sb(110) film, with n varying from 1 to 12. (e) The red solid squares are energy differences $E_d(n) = E_e(n) - [E_e(n-1) + E_e(n+1)]/2$ for n-ML Sb(110), with n varying from 2 to 11. The red lines are guides to the eye in (d) and (e).

5.3.2 Atomic structures

Fig. 5.4(a) is the side view of the ideal bulk-terminated 4 ML Sb(110) from $[01\bar{1}]$ direction for reference (see Fig. 2.11 for more details). The solid circles indicate Sb atoms. The purple solid lines indicate covalent bonds, the length of which is 2.90 Å. Within each ML, the out-of-plane corrugation is 0.2 Å. Half of the atoms at the top and bottom surfaces have dangling bonds, as indicated by the blue dash lines. The upper image of Fig. 5.4(b) is the side view of the relaxed the 2 ML Sb(110), while the lower image is the perspective view. Fig. 5.4(b) shows that the two layers pair up, form one paired-layer and saturate all the dangling bonds on the top and bottom surfaces. Within each ML, the out-of-plane corrugation is 0.32 Å, larger than the bulk value. The intralayer bonds within each ML are 2.91 Å in length, which is almost the same as the bulk value. The interlayer bonds decrease to 2.82 Å in length. This paired-layer structure is analogous to the black phosphorus (BP) structure.[11] We call this BP-like structure[8] hereafter. The relaxed 4 ML Sb(110) is shown in Fig. 5.4(c). The 1st and 2nd ML form a BP-like paired-layer. The 3rd and 4th ML form another paired-layer.

On Si(111), Bi(110) follows even-ML growth mode below 4 ML. More deposition of Bi causes the Bi(110) to transform into Bi(111).[8] Nagao *et al.*[8] proposed the BP-like structure for both 2 ML and 4 ML Bi(110). 2 ML Bi(110) BP-like structure are the same as our 2 ML Sb(110) model in Fig. 5.4(b). However, the 4 ML Bi(110) BP-like structure is different from our 4 ML Sb(110). Following the previously proposed 4 ML Bi(110) structure, the relaxed BP-like structure for 4 ML Sb(110) is shown in Fig. 5.4(d), which also consists of two paired-layers. Within each paired-layer, atoms are connected by

strong covalent bonds. The two paired-layers are connected by weak van der Waals force. There are similarities and differences between the BP-like structure in Fig. 5.4(c) and Fig. 5.4(d). The similarity is that two ML of atoms are connected by strong covalent bonds to saturate the dangling bonds from the top and bottom ML, forming paired-layers. The differences are: (i) The stacking sequence for the two paired-layers are different; the stacking sequence of our model (Fig. 5.4(c)) is the same as that of the real BP structure. (ii) The distance between the two paired-layers are shorter for our model, indicating that the interaction between the paired-layers is stronger in our model.

We now discuss the possibility of the two structures shown in Fig. 5.4(c) and (d). There are two evidences supporting our model. First, the extra energies E_e are 106.6 meV and 120.8 meV for the structure of Fig. 5.4(c) and 5.4(d), respectively, so the former is lower in energy. Second, since the subtle change in the atomic structure may affect the electronic structure, we compare the calculated DOS from different structures with the measured STS, as shown in Fig. 5.4(e)-(g). The black solid lines are the experimental STS on 4 ML Sb(110) film; the red solid lines are calculated DOS of (e) the ideal bulk-terminated 4 ML Sb(110), (f) for the structure shown in Fig. 5.4(c) and (g) for that shown in Fig. 5.4(d). The calculated DOS in Fig. 5.4(e) is in poor agreement with the STS result, while the fitting is better in Fig. 5.4(g) and is best in Fig. 5.4(f). Detailed STS for ultrathin Sb(110) will be presented in the next section.

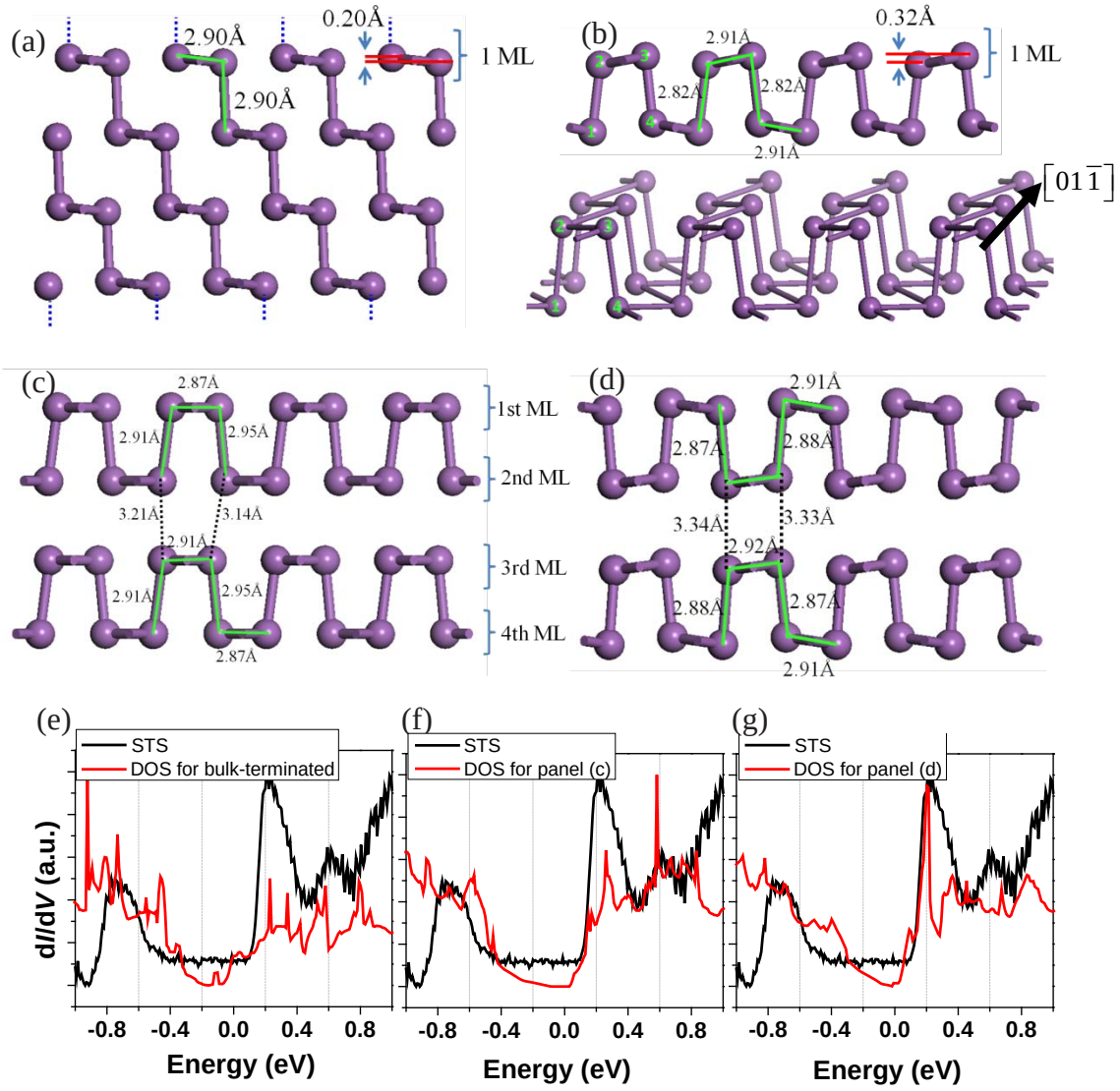

Fig. 5.4. (a)-(d) Schematic view of the Sb(110) atomic structure. The brown solid balls and lines indicate Sb atoms and covalent bonds, respectively. (a) Schematic side view of the ideal bulk-terminated 4 ML Sb(110) atomic structure. (b) Side view (top panel) and perspective view (bottom panel) of the relaxed 2 ML Sb(110) atomic structure, showing the BP-like structure. (c) Side view of the relaxed 4 ML Sb(110) atomic structure. (d) Side view of the relaxed BP-like 4 ML Sb(110) based on the 4 ML Bi(110) model in Ref. [8]. (e)-(g) The STS (black solid lines) and calculated DOS (red solid lines) from (e) the ideal bulk-terminate 4 ML Sb(110), (f) the structure shown in panel (c) and (g) the structure shown in panel (d). Note that all the lines are normalized for clarity. The calculated DOS are shifted to lower energy by 0.08 eV, 0.08 eV and 0.00 eV in panel (e), (f) and (g), respectively, to align the calculated DOS peak with STS high peak at 0.23 eV.

In fact, although the BP-like structure (Fig. 5.4(d)) is also commonly considered as a possibility for the ultrathin Bi(110), the real structure is still uncertain.[12] There is evidence showing that strong binding, instead of weak Van der Waals force, exists between each layers of ultrathin Bi(110) on HOPG.[13] In a recent paper,[7] the DOS of many structures are calculated to fit the STS data from ultrathin Bi(110) on HOPG. The only DOS that is in reasonable agreement with the STS is the one from the freestanding slabs with relaxed surfaces only. The model for 4 ML and 6 ML Bi(110) are composed of bulk-like interior and the BP-like paired-layers at the surfaces.

The relaxed 6 ML Sb(110) (Fig. 5.5(a)) is analogous to the relaxed 4 ML Sb(110). According to the bonding strength, this structure can be considered as a stack of three paired-layers and relative weak bonding between the paired-layers. According to the bond length, the intralayer bonding within the top and bottom paired-layers are stronger than that of the middle. Fig. 5.5(b) schematically shows the relaxed 7 ML Sb (110) structure. The top two layers as well as the bottom two layers form paired-layer, while the interior structure is more like the bulk structure.

We have performed the calculations for Sb(110) films from 1 ML to 12 ML. For other even-ML Sb(110) (8, 10, 12 ML), the structure can be regarded as analogous to the 6 ML Sb(110), and the atomic structures of odd-ML Sb(110) (9, 11 ML) are similar to the 7 ML Sb(110), except for some minor differences in the bond lengths. The trend is that as the film gets thicker, the interior atoms are more bulk alike, but the top and bottom two layers always tend to form paired-layer to saturate dangling bonds. We will now examine the electronic structures of Sb(110) ultrathin films.

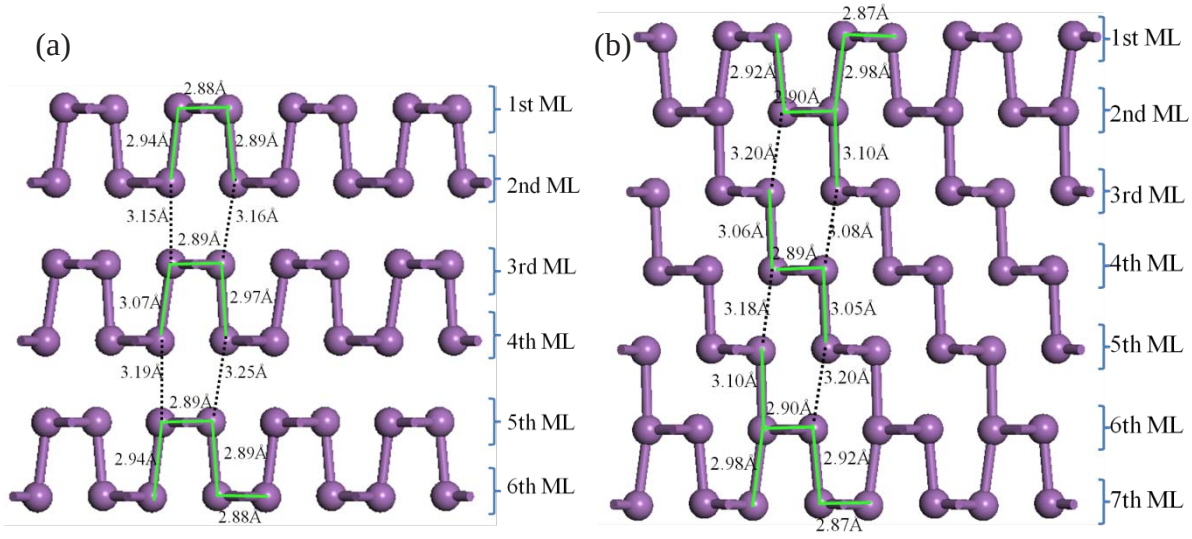

Fig. 5.5. Schematic side view of the relaxed (a) 6 ML Sb(110) atomic structure and (b) 7 ML Sb(110) atomic structure.

5.3.3 Electronic properties

Fig. 5.6(a) shows the measured STS from Sb(110) films on HOPG from 2 to 10 ML and the calculated DOS from relaxed freestanding films. To fit the STS, the Fermi levels of the calculated DOS are shifted by -0.16 eV (2 ML), -0.08 eV (4 ML), -0.08 eV (6 ML), -0.04 eV (7 ML), -0.12 eV (8 ML), +0.06 eV (9 ML) and 0.00 eV (10 ML). The downward shift of the Fermi levels for the calculated DOS from 2 ML to 8 ML compared with STS may indicate charge transfer from HOPG to Sb(110) islands (n-type doping). STS studies of 2 ML, 4 ML and 6 ML Bi(110) on HOPG also support n-type doping.[7] However, since the Fermi level of 9 ML DOS is shifted upward and the 10 ML DOS does not show any shift, the small Fermi level shifts may simply come from uncertainties in the calculated band energies.

Let us focus on the STS of the 2 ML Sb(110) film (black solid line in Fig. 5.6(a)). There are two large peaks at -0.67 eV (indicated as *a*) and 0.44 eV (indicated as *b*), respectively, which are well reproduced in the calculated DOS (black dot line), except that the peak below Fermi level is at -0.73 eV. The 0.06 eV shift compared with STS is acceptable considering the fact that the STS is quite sensitive to the spatial distribution of the electronic states. For STS, between these two large peaks (*a* and *b*) around the Fermi level, there is a 0.75 eV wide flat region, which may indicate an energy gap or very weak surface state within this energy range. The calculated DOS and band structure of the 2 ML Sb(110) are drawn together for clarity in Fig. 5.6(b). Comparing the DOS and band structure gives us some hint on where the peaks originate. We can see that the two large peaks *a* and *b* originate from the superposition of quite a few valence bands and conduction bands, respectively. In region I, there is only one band (the highest valence band) between $\bar{\Gamma}$-$\bar{X}_2$ contributing to the DOS. If there exist strong surface states, the surface bands are the highest valence band and lowest conduction band, which usually give rise to peaks in the STS.[14, 15] STS at region I is almost flat, indicating that there is no strong surface states at 2 ML Sb(110). The real-space charge distributions for the highest valence band and lowest conduction band at TRIMs are shown in Fig. 5.8(a).

The STS for 4 ML and 6 ML Sb(110) films are qualitatively similar to that of 2 ML Sb(110). The flat regions around Fermi level indicate very weak surface states. The two high peaks *a* and *b* are getting closer both in STS and the calculated DOS, since the quantum confinement energy is reduced in thicker film, valence band is shifted upward and conduction band downwards in energy, which are confirmed in the band structure calculations in Fig. 5.7. From 7 ML above, there is no flat region around the Fermi level,

indicating relatively abundant states around the Fermi level. This is also consistent with the calculated band structures in Fig. 5.7. There is one thing worth pointing out that agreement between STS and calculated DOS is better for thinner films. This is because the STS detects the states localized at the surface only, while the calculated DOS is an integration of all the states, including the states localized at the surface and in the bulk.

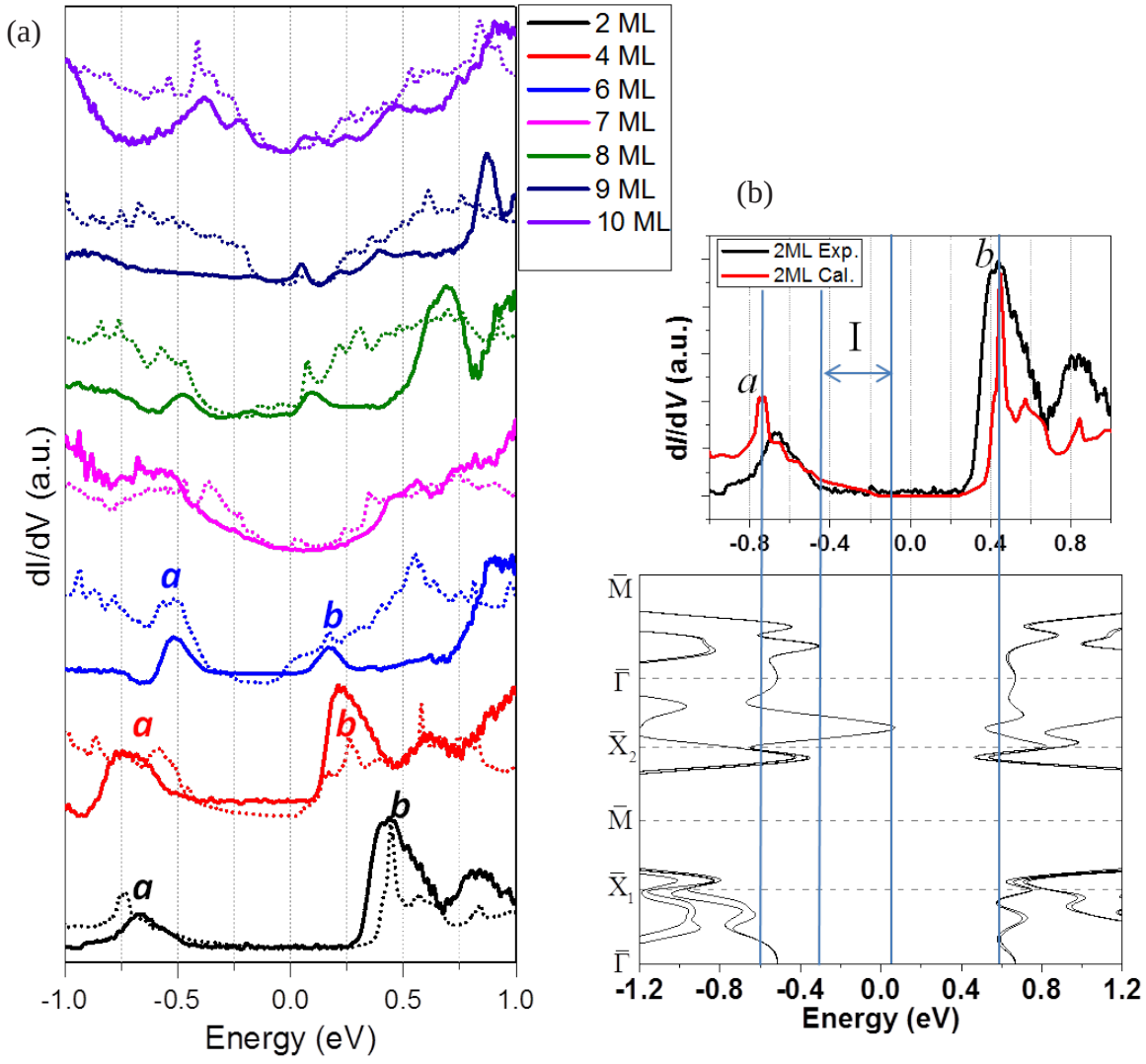

Fig. 5.6. (a) The STS (solid lines) and calculated DOS (dash lines) of 2 ML to 10 ML Sb(110). Note that all the STS and DOS are normalized for clarity. (b) Top panel: re-plot of STS (black solid line) and calculated DOS (red solid line) of the 2 ML Sb(110). Bottom panel: band structure of the 2 ML Sb(110) film. The blue solid lines are guides to the eye for the comparison of the STS, DOS and band structure.

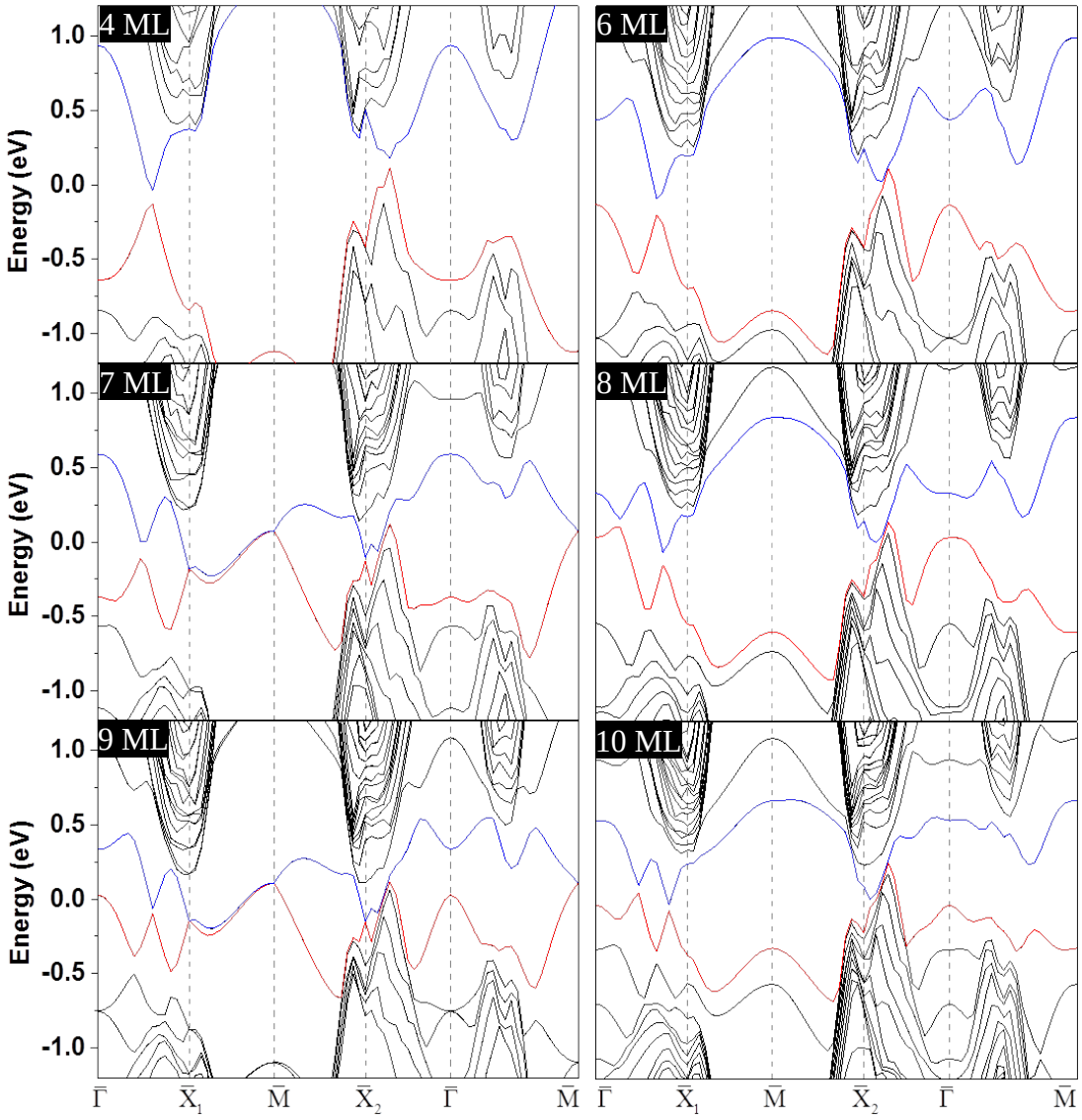

Fig. 5.7. Band structures of The Sb(110) films from 4 ML to 10 ML. red and blue solid lines indicate the highest valence bands and lowest conduction bands, respectively.

The band structures show differences between even- and odd-ML films in Fig. 5.7. The differences lie in the highest valence bands (red solid lines) and lowest conduction bands (blue solid lines). For example, along $\bar{X}_1$-$\bar{M}$-$\bar{X}_2$ direction, the highest valence bands and lowest conduction bands are far apart for the even-ML films, but get closer for the odd-ML films. The differences may be due to the different atomic structures of the

even- and odd-ML Sb(110) (see Fig. 5.5). The dispersions of the highest valence bands and lowest conduction bands for 7 and 9 ML films are quite similar to the surface bands of the thick film shown in Fig. 5.1(b),[2] probably because the interior atomic bonding is bulk-like for odd-ML Sb(110). For other bands as shown in black, there is no obvious even- or odd-ML dependence. This distinctive even- and odd-ML dependence character for the highest valence bands and lowest conduction bands indicate that they are very likely to be derived from the surface bands in a thick film.

To investigate if they are surface states or not, the real-space charge distributions along the surface normal direction for the highest valence bands and the lowest conduction bands of 2 ML, 6 ML and 7 ML at four TRIMs ($\bar{\Gamma}$, $\bar{X}_1$, $\bar{M}$, $\bar{X}_2$) are calculated, and plotted in Fig. 5.8(a), (b) and (c), respectively. The corresponding positions of the films are indicated by the side view on top. Unlike the real-space charge distributions of surface bands at $\bar{\Gamma}$ on thin Sb(111) film (see Fig. 4.5), there are no clear surface band characters here. They are more like surface resonant states on Sb(110). However, the existence of TSS should not depend on the surface index,[16] *i.e.*, since the TSS exist on Sb(111) surface, so do on Sb(110) surface. The thickness of 4 BL Sb(111) and 7 ML Sb(110) is 15.0 Å and 21.8 Å, respectively. If the penetration depth of surface states on Sb(111) and Sb(110) are comparable, there should be some surface band character for the highest valence bands and lowest conduction bands at certain points. The lack of surface band character on thin Sb(110) may be because the penetration depth of surface states on Sb(110) is longer than that on Sb(111) or because the Sb(110) films are relaxed. For comparison, we calculated the real-space charge distributions for the highest valence bands and the lowest conduction bands of bulk-terminated 7 ML Sb(110) as plotted in

Fig. 5.8(d). Compared with the surface states of 4 BL Sb(111) at $\bar{\Gamma}$ (see Fig. 4.5), the surface character for bulk-terminated 7 ML Sb(110) is still not obvious. The charge distributions are more similar to the surface resonant states of 4 BL Sb(111) at $\bar{M}$ (see Fig. 4.5), indicating that the surface bands in a thick Sb(110) film have longer penetration depth and thus strong inter-surface coupling in 7 ML Sb(110) film than in 4 BL Sb(111). Comparing Fig. 5.8(d) and Fig 5.8(c), we find that these states accumulate a little bit more on the bulk-terminated surfaces than on the relaxed film surfaces. For example, at $\bar{M}$ point this is obvious. We have performed STS conductance maps on Sb(110) from 2 ML to 10 ML, but cannot get repeated QPI patterns as on Sb(111) surfaces, mainly because the longer penetration depth of the surface sates in Sb(110) films. The relaxation of the ultrathin Sb(110) films further weakened the surface states.

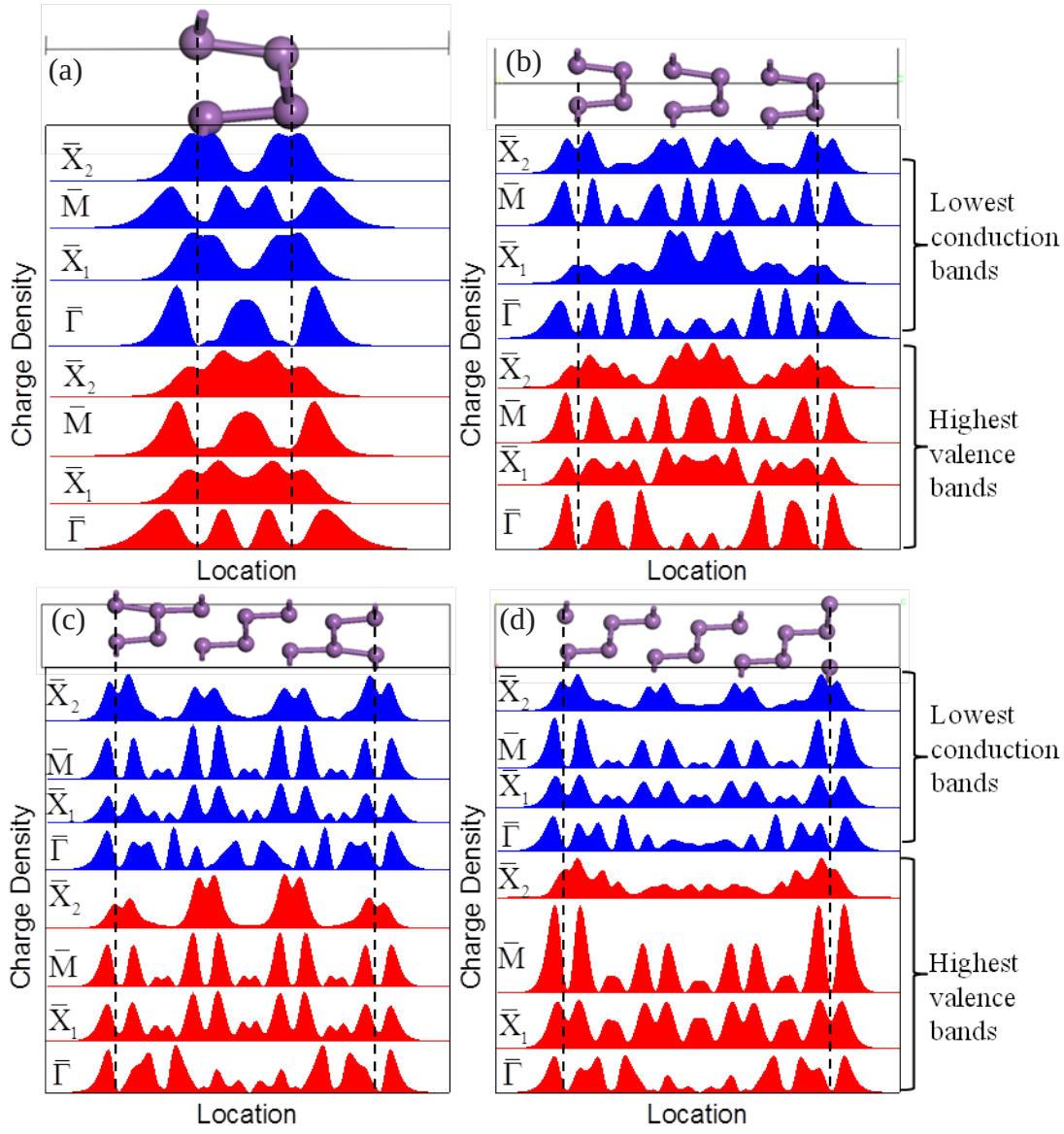

Fig. 5.8. Real-space charge distributions along the surface normal direction for the highest valence bands (red) and the lowest conduction bands (blue) at four TRIMs ($\bar{\Gamma}$, $\bar{X}_1, \bar{M}, \bar{X}_2$) of the (a) 2 ML Sb(110), (b) 6 ML Sb(110), (c) 7 ML Sb(110) and (d) bulk-terminated 7 ML Sb(110). The corresponding positions of the film are indicated by the side view on top. Black dash lines are guides to the eye.

5.3.4 Edge reconstruction

We have not found any surface reconstruction on either Sb(111) or Sb(110) surface. Also, there are no surface reconstructions found on Bi(111), Bi(110) and Bi(100) surfaces, probably due to the strong spin-orbit coupling.[17] We have found a 4× edge reconstruction on Sb(110), which has never been reported before to our knowledge. There are also 4× and 2× edge reconstructions on 4 ML Bi(110) on graphene,[18] which is the only paper reporting the edge reconstruction on Bi surfaces so far.

Fig. 5.9(a) is a 300 nm × 300 nm STM image of Sb(110) films on HOPG. Fig. 5.9(b) is a zoom-in STM image of the square area in Fig. 5.9(a). The right part of Fig. 5.9(b) is 6 ML Sb(110) while the left is 4 ML. Fig. 5.9(c) is the derivative image of Fig. 5.9(b) that can enhance the atomic feature on both 6 ML and 4 ML areas. In Fig. 5.9(d), the blue line is the profile along the blue straight line in Fig. 5.9(b); the red line is the profile along the red straight line in Fig. 5.9(b). The profiles clearly indicate the 4× edge reconstruction. In our experiment, not all edges show this reconstruction. Two necessary conditions must be fulfilled: (i) The sharp edge is along $\left[01\bar{1}\right]$; (ii) it is the edge of 2-ML Sb(110) grown on another Sb(110) film. The second condition means that there is no reconstruction if the thickness of the edge is > 2 ML. There may be no reconstruction even the two conditions are fulfilled. In Fig. 5.9(e), the lower three lines are the STS at points a, b and c in Fig. 5.9(b); the upmost line is the STS on 6 ML Sb(110) film far away from the edge. STS from point a shows extra peaks compared with the STS far away from the edge, which indicates extra electronic states. However, these states are quite localized, since STS from point b and c are already quite similar with the STS far away

from the edge. We have tried several models for this 4× edge reconstruction; But so far, none of the calculation results from these models is in satisfactory agreement with the experiments. More effort is needed to figure out this edge reconstruction structure.

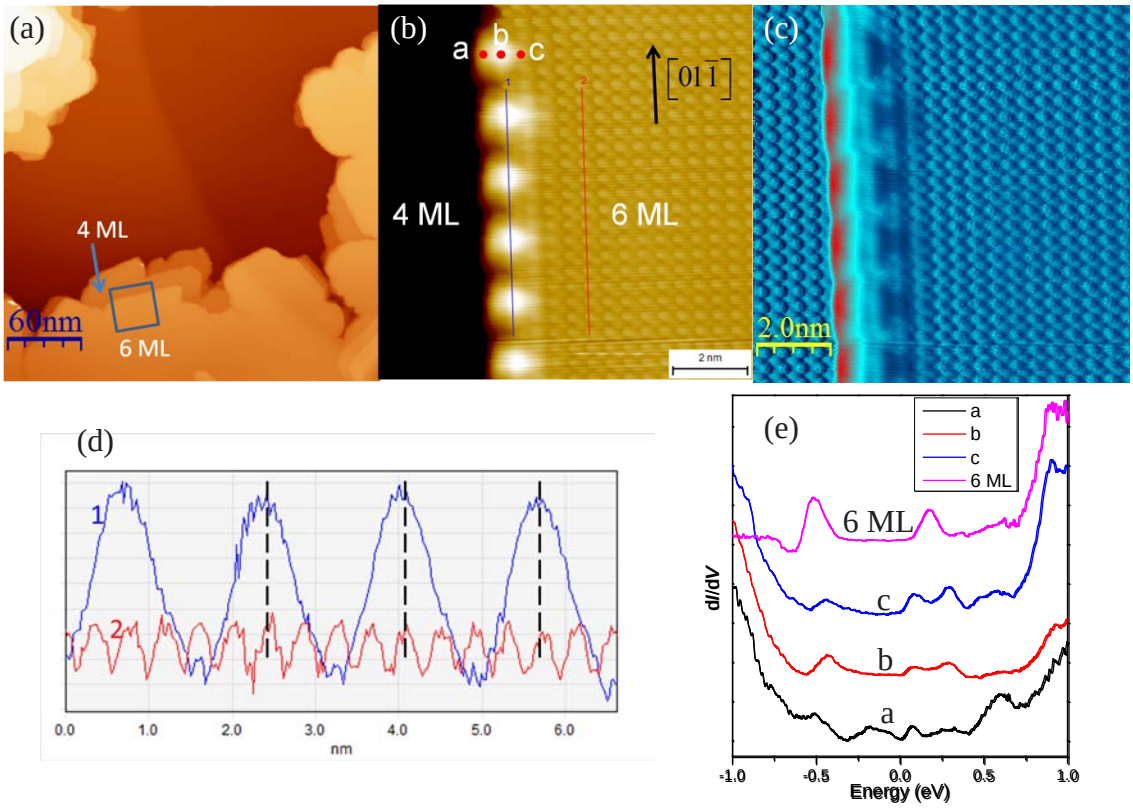

Fig. 5.9. (a) STM image of 10.5-ML Sb deposited on HOPG at RT. (b) A zooming-in STM image from the square area in panel (a). (c) The derivative image of panel (b) that can emphasize the atomic resolution on both 4 ML and 6 ML Sb(110) area. (d) The blue line is the profile along the blue strait line in panel (b); the red line is the profile along the red strait line in panel (b). Black dash lines are guides to the eye. (e) the lower three lines are the STS at points a, b and c, as indicated in panel (b); the topmost line is the STS on 6 ML Sb(110) film far away from the edge.

5.4 Conclusions

In-situ STM/STS studies together with first-principles calculations on ultrathin Sb(110) films grown on HOPG are demonstrated. The Sb(110) follows even-ML growth mode below 6 ML. Above 6 ML, both even- and odd-ML Sb(110) can be observed. First-principles calculations support this growth mode and show that the ultrathin Sb(110) films are relaxed, unlike the ultrathin Sb(111) films, which are bulk-like. The DOS calculated from the relaxed structures is in reasonable agreement with the STS data. Real-space charge distributions along the surface normal direction for the highest valence bands and the lowest conduction bands do not show clear sign of surface band character, mainly because of long penetration depth and partly because of the relaxed structure. The weak surface states explain the lack of QPI patterns on ultrathin Sb(110) films. The 4× reconstruction along the edge of the ultrathin Sb(110) is found to form under certain conditions.

References

[1] M. Bianchi *et al.*, Surface states on a topologically nontrivial semimetal: The case of Sb(110). *Physical Review B* **85**, 155431 (2012).

[2] A. Strozecka *et al.*, Unconventional spin texture of a topologically nontrivial semimetal Sb(110). *New Journal of Physics.* **14**, 103026 (2012).

[3] B. Stegemann, C. Ritter, B. Kaiser, K. Rademann, Crystallization of Antimony Nanoparticles: Pattern Formation and Fractal Growth. *Journal of Physical Chemistry B* **108**, 14292 (2004).

[4] S. S. Kushvaha *et al.*, Self-assembled Ge, Sb and Al nanostructures on graphite: Comparative STM studies. *Nanotechnology* **18**, 145501 (2007).

[5] X.-S. Wang, S. S. Kushvaha, Z. Yan, W. Xiao, Self-assembly of antimony nanowires on graphite. *Applied Physics Letters* **88**, 233105 (2006).

[6] A. V. Narlikar, Y. Y. Fu, *Oxford Handbook of Nanoscience and Technology: Volume 2: Materials: Structures, Properties and Characterization Techniques*. Oxford: Oxford University Press, 2010.

[7] P. J. Kowalczyk *et al.*, Electronic Size Effects in Three-Dimensional Nanostructures. *Nano Letters* **13**, 43 (2013).

[8] T. Nagao *et al.*, Nanofilm Allotrope and Phase Transformation of Ultrathin Bi Film on Si(111)-7x7. *Physical Review Letters* **93**, 105501 (2004).

[9] T. Hirahara *et al.*, Role of Spin-Orbit Coupling and Hybridization Effects in the Electronic Structure of Ultrathin Bi Films. *Physical Review Letters* **97**, 146803 (2006).

[10] Y. Liu, R. E. Allen, Electronic structure of the semimetals Bi and Sb. *Physical Review B* **52**, 1566 (1995).

[11] H. Iwasaki, T. Kikegawa, Structural Systematics of the High-Pressure Phases of Phosphorus, Arsenic, Antimony and Bismuth. *Acta Crystallographica Section B* **53**, 353 (1997).

[12] P. J. Kowalczyk *et al.*, Anisotropic oxidation of bismuth nanostructures: Evidence for a thin film allotrope of bismuth. *Applied Physics Letters* **100**, 151904 (2012).

[13] P. J. Kowalczyk *et al.*, STM and XPS investigations of bismuth islands on HOPG. *Surface Science* **605**, 659 (2011).

[14] K. K. Gomes *et al.*, Quantum Imaging of Topologically Unpaired Spin-Polarized Dirac Fermions. *arXiv:0909.0921v2* (2009).

[15] A. Stróżecka, A. Eiguren, J. I. Pascual, Quasiparticle Interference around a Magnetic Impurity on a Surface with Strong Spin-Orbit Coupling. *Physical Review Letters* **107**, 186805 (2011).

[16] J. C. Y. Teo, L. Fu, C. L. Kane, Surface states and topological invariants in three-dimensional topological insulators: Application to $Bi_{1-x}Sb_x$. *Physical Review B* **78**, 045426 (2008).

[17] P. Hofmann, The surfaces of bismuth: Structural and electronic properties. *Progress in Surface Science* **81**, 191 (2006).

[18] J.-T. Sun *et al.*, Energy-Gap Opening in a Bi(110) Nanoribbon Induced by Edge Reconstruction. *Physical Review Letters* **109**, 246804 (2012).

Chapter 6

Conclusions and Future Work

Motivated by the unique electronic properties of Sb and its potential applications in spin related transportation or processing, this thesis address the growth, atomic structure and electronic properties of ultrathin Sb films on Si-based substrate (Si(111) and Si(111)-$\sqrt{3}\times\sqrt{3}$:Bi) and HOPG.

The quality of the thin film is important for real applications. Thanks to the cracked Sb source with single atoms evaporated instead of Sb_4 molecules, we can grow self-assembled atomically flat Sb(111) thin films on Si(111) and Si(111)-$\sqrt{3}\times\sqrt{3}$:Bi. At or above RT, Sb form thin films on Si(111) with both Sb(111) and Sb(110) coexisting. By annealing the sample grown at RT, Sb atoms gain sufficient kinetic energy and rearrange themselves into single crystalline Sb(111) films. First-principles calculations support this transformation, since Sb(111) is lower in energy than Sb(110) at the same coverage from 1 to 10 BL (or 1 to 12 ML). The single crystalline Sb(111) thin film $\geq$ 4 BL of best quality can be grown by deposition at low temperature followed with post-growth annealing to about 280 °C for 10 min. The critical thickness of Sb(111) is 4 BL below which Sb(111) films cannot form. The Si(111) substrate is quite active, with 19 dangling bonds in each 7×7 unit cell (see Section 2.3.1), hence kinetics play an important role in the self-assembly process. The kinetics can be manipulated by controlling the substrate temperature. This is the reason why the morphology of Sb nanostructures is significantly affected by the Si substrate temperature. In comparison, Sb growth on HOPG is less affected by the substrate temperature, since HOPG substrate is inert.

TSS on Sb(111) is spin-polarized for a thick film (~30 BL). At 9 BL Sb(111), inter-surface coupling is significant near $\bar{M}$, while near $\bar{\Gamma}$, surface states are still spin polarized. This is because the penetration depth of surface states is longer near $\bar{M}$, where the surface states merge into the bulk bands; away from $\bar{M}$, penetration depth is short. From first-principles calculations of freestanding 4 BL Sb(111), an energy gap should open at the Dirac point, since this film thickness is comparable with the penetration depth of surface states at $\bar{\Gamma}$, but ARPES measurement did not show such a gap, because of the SIA induced by the substrate. By replacing one Sb atom at the bottom surface layer by one Bi atom in each unit cell of 4 BL Sb(111), the SIA effect is simulated with first-principles calculations. The calculations show that the degeneracy of the surface states in *k*-space is lifted by the SIA, hindering the quantum tunneling of electrons between two surfaces. This protects the surface states from opening an energy gap. The real-space distributions of the surface states near $\bar{\Gamma}$ are in agreement with the effective continuous models calculation results. The calculated FT-STS is in good agreement with the experimental results. First-principles calculations on the Bi-Sb terminated 5 BL Sb(111) show that the thicker film is less affected by the SIA.

Since Sb(110) surface is hard to get from bulk crystal, this surface is rarely studied. We present the preparation, atomic structure and electronic properties of ultrathin Sb(110) films from 2 to 10 ML that are prepared on HOPG. The Sb(110) films follow even-ML growth mode below 6 ML; above 6 ML, both even- and odd-ML Sb(110) can be observed. First-principles calculations show that the ultrathin Sb(110) films are relaxed, unlike the ultrathin Sb(111) films which are bulk-like. The energy of the relaxed Sb(110) films supports the even-ML growth mode below 6 ML. The calculated DOS is in

reasonable agreement with the STS. We do not find any repeatable QPI patterns, indicating weak surface states on ultrathin Sb(110). Calculated real-space charge distributions of the highest valence bands and lowest conduction bands indicate that the bands are surface resonant states, instead of surface states, mainly because of longer penetration depth of these sates. A 4× reconstruction forms at the edge along $[0\bar{1}1]$ under certain conditions.

The inter-surface coupling in Sb ultrathin films can be investigated further using other probes such as ARPES. ARPES measurements have been performed extensively on the second generation TI, for example, Bi_2Se_3. However, the unit layer of these TI materials is a quintuple-layer (QL), of thickness about 10 Å. APPES measurements cannot detect the bottom surface states of Bi_2Se_3 over 1 QL, because of short photoelectrons escape depths (merely 5~10 Å for photon energy of 20~50 eV). 4 ML Sb(111) (15 Å) is on the verge of the depth resolution of ARPES, hence, it is possible to observe states from different surfaces. It is even possible to study the top surface doping effect on the bottom surface states. If these experiments are able to be performed, the ultrathin Sb(111) films would be an ideal candidate to study the inter-surface coupling and the substrate effect.

Very recently, it is predicted that 1 BL Sb(111) is in nontrivial topological insulating phase induced by tensile strain.[1] The thinnest Sb(111) film can be grown is 4 BL so far. Realization of ultrathin Sb(111) below 4 BL can be tried on other substrates. Sb_2Te_3 may be one of the candidates, considering the case that on Bi_2Te_3, 1 BL Bi(111)

has been realized.[2] The possibility that ultrathin Sb(110) may become 2D TI at certain thickness can also be studied by experiments and calculations.

References

[1] F. C. Chuang *et al.*, Tunable topological electronic structures in Sb(111) bilayers: A first-principles study. *Applied Physics Letters* **102**, 022424 (2013).

[2] F. Yang *et al.*, Spatial and Energy Distribution of Topological Edge States in Single Bi(111) Bilayer. *Physical Review Letters* **109**, 016801 (2012).